CFD MODELING AND EXPERIMENTS IN A BUBBLING FLUIDIZED BED REACTOR FOR BIOMASS GASIFICATION

MS. PINCHOOKORN CHOBTHIANGTHAM
ID: 49920011

A THESIS SUBMITTED AS A PART OF THE REQUIREMENTS FOR THE DEGREE OF MASTER OF PHILOSOPHY IN ENERGY TECHNOLOGY

THE JOINT GRADUATE SCHOOL OF ENERGY AND ENVIRONMENT AT KING MONGKUT'S UNIVERSITY OF TECHNOLOGY THONBURI

2ND SEMESTER 2013

CFD Modeling and Experiments in a Bubbling Fluidized Bed Reactor
for Biomass Gasification

Ms. Pinchookorn Chobthiangtham
ID: 49920011

A Thesis Submitted as a Part of the Requirements
for the Degree of Master of Philosophy
in Energy Technology

The Joint Graduate School of Energy and Environment
at King Mongkut's University of Technology Thonburi

2nd Semester 2013

Thesis Committees

(Assoc. Prof. Dr. Suneerat Fukuda)	Advisor
(Assoc. Prof. Dr. Pornpote Piumsomboon)	Co-Advisor
(Asst. Prof. Dr. Suthum Patumsawad)	Member
(Dipl.-Ing. Werner Siemers)	Member
(Prof. Dr. Sankar Bhattacharya)	External Examiner

Thesis Title: CFD Modeling and Experiments in a Bubbling Fluidized Bed Reactor for Biomass Gasification

Student's name, organization and telephone/fax numbers/email

Miss Pinchookorn Chobthiangtham

Department of Energy Technology,

The Joint Graduate School of Energy and Environment (JGSEE)

King Mongkut's University of Technology Thonburi (KMUTT)

126 Pracha Uthid Rd., Bangmod, Tungkru, Bangkok 10140 Thailand

Telephone 08-7550-4805

E-Mail: chobpin@gmail.com

Supervisor's name, organization and telephone/fax numbers/email

Assoc. Prof. Dr. Suneerat Fukuda

Department of Energy Technology

The Joint Graduate School of Energy and Environment (JGSEE)

King Mongkut's University of Technology Thonburi (KMUTT)

126 Pracha Uthid Rd., Bangmod, Tungkru, Bangkok 10140 Thailand

Tel. 0-2872-9014 Fax. 0-2872-6978

E-mail: suneerat@jgsee.kmutt.ac.th

Co-Supervisor, organization and telephone/fax numbers/email

Assoc. Prof. Dr. Pornpote Piumsomboon

Department of Chemical Technology, Faculty of Science

Chulalongkorn University

Bangkok, Thailand 10330

Tel. 0-2218-7676 Fax. 0-2255-5831

E-mail: pornpote.p@chula.ac.th

Topic: CFD Modeling and Experiments in a Bubbling Fluidized Bed Reactor for Biomass Gasification

Name of student: Miss Pinchookorn Chobthiangtham

Student ID: 49920011

Name of Supervisor: Assoc. Prof. Dr. Suneerat Fukuda

ABSTRACT

This research consists of two main parts: the experimental investigation of rubber woodchip gasification and computational fluid dynamic (CFD) simulation of a bubbling fluidized bed gasifier (BFBG), the main device used for gasification experiments. The objective of the gasification experiment is to investigate the potential of utilizing high-moisture (27% moisture content) biomass fuel by mixing with plastic waste (High Density Polyethylene type). For the gasification model simulation, the CFD codes were developed using FLUENT on three-dimensional computational domains to investigate the hydrodynamic behaviors of the BFBG. The Euler-Euler approach with KTGF was applied. The input parameters and the optional model selections were studied and validated under cold flow (ambient temperature and non-reactive considered) conditions by comparing the simulation with the experimental results of a downscale BFB made of acrylic. The hydrodynamic behaviors especially inside bed zone of the BFBG were investigated comparing the non-simplified (actual configuration) and simplified air distributor under both cold flow condition and elevated temperature (hot sand with heat transfer and non-reactive considered) condition.

The results of the gasification experiments showed a significant improvement of gasification performance from mixing the high-moisture (27% M.C.) rubber woodchip with plastic waste (SPB). Even at 10% mixing ratio, the HHV of the product gas increased by about 50% and 25% compared to the case of high-moisture rubber woodchip (27% moisture) and pre-dried rubber woodchip (8% moisture), respectively. At 20% mixing ratio, the HHV of product gas increased from 3.85 to 6.06 MJ/Nm^3. The carbon conversion efficiency was significantly improved to reach the level of the pre-dried rubber woodchip when mixing with 20% SPB. Moreover, increasing ER could also effectively increase the carbon conversion efficiency for all feedstocks. These experimental results indicate that the

co-gasification with plastic waste can be considered as a promising solution for utilizing high-moisture biomass and effective way for plastic waste management is an additional benefit.

Comparing the non-simplified and simplified air distributor models, which were simulated under cold flow conditions, the results show that their hydrodynamic behaviors, i.e. bubble formation and motion inside bed zone, gas-solid flow pattern, bed expansion ratio, and profiles of absolute pressure along the height of bed zone, were different. More fluctuations were observed, and the loops of bubble formation and motion were also faster in a non-simplified air distributor model. The gas-solid flow patterns in the simplified air distributor model were different from those in the non-simplified air distributor model, as there were large-size vortexes in the lower part of the bed in the simplified air distributor model, while the gas-solid flow mainly occurred around the nozzles in the non-simplified air distributor model, resulting in large-size of vortexes in upper part of the bed. For the bed expansion ratio, it was 1.33 and 1.16 for non-simplified and simplified air distributor model, respectively. The difference of these comparison bed expansion ratios indicated that the expansion height of fluidized bed obtained from simplified air distributor model was underestimated as compared to the non-simplified air distributor model which was closer to the actual BFBG. The profiles of absolute pressure along the height of bed zone in simplified air distributor model was different from that in non-simplified air distributor model as the absolute pressure at each height in simplified air distributor model was nearly constant, while fluctuations were clearly observed in non-simplified air distributor model, especially in upper zone of the bed. In addition, in both non-simplified and simplified air distributor model, the pressure drop across the bed resulted from the simulation under elevated temperature condition was lower and the bubbles formed rose to the bed surface faster than that obtained from the simulation under cold flow condition. The main reasons are the decrease in air density and dynamic pressure with increasing temperature.

Keyword: CFD; Three-dimensional model; Simulation; Bubbling Fluidized Bed; Biomass Gasification

ACKNOWLEDGEMENTS

In the first place, I would like to express my gratitude to the following people who gave me support and encouragement for my Ph.D. study. Assoc. Prof. Dr. Suneerat Fukuda for a chance to work under her guidance, support, motivation, encouragement, and discussions from the beginning to the end of this research as well as giving me extraordinary experiences throughout the work. I have gained a lot of knowledge, many skills and her assistance in writing reports and papers. I would like to thank specially for Assoc. Prof. Dr. Pornpote Piumsomboon, my co-advisor, who gave me the valuable knowledge, great advice, and support. And many special thanks to Asst. Prof. Dr. Suthum Pathumsawad, my committee member, who always gave me very useful ideas and support. I also appreciate the kindness of Dipl.-Ing. Werner Siemers, another committee member who supported and gave me a great advice at early stage of this research. In addition, I would like to express my gratitude to Prof. Dr. Sankar Bhattacharya who served as external examiner for his valuable comments.

Furthermore, I would like to express my special thanks to Mr. Sapha Pansanga and Dr. Benjapol Kongsombut who have consulted me on the simulation part, and Dr. Setta Sasananan, my colleague, who helped me handle my work load during tough times, and all my friends and colleagues who gave me encouragement and support.

I especially want to dedicate my thesis to my family members. They provided me a chance to study Ph.D. and have continued to give me help and encouragement unconditionally. Their love and understanding have allowed me to be the person I am today, and for that I will be eternally grateful.

In conclusion, I recognize that this research would not have been possible without the financial assistance of the Joint Graduate School of Energy and Environment (JGSEE).

CONTENTS

CONTENTS (Cont')

CONTENTS (Cont')

LIST OF TABLES

LIST OF FIGURES

LIST OF FIGURES (Cont')

LIST OF FIGURES (Cont')

LIST OF FIGURES (Cont')

LIST OF FIGURES (Cont')

LIST OF FIGURES (Cont')

LIST OF SYMBOLS AND ABBREVIATIONS

A	=	Cross-sectional area of the bed
ASTM	=	American society for testing and materials
ATM	=	Standard atmosphere
BFBG	=	Bubbling fluidized bed gasifier
CFD	=	Computation fluid dynamics
C	=	Carbon-containing organic compound
CH_4	=	Methane
CO	=	Carbon monoxide
CO_2	=	Carbon dioxide
cm w.g.	=	centimetre water gauge
DEM	=	Discrete element method
DNS	=	Direct numerical simulation
E	=	Equation
ER	=	Equivalent ratio
g/m^2s	=	gram per square meter second
H_2	=	Hydrogen
H_2O	=	Water
HHV	=	Higher heating value
Hz	=	Hertz
ha	=	hectare
IGCC	=	Integrated Gasification Combined Cycle
KTGF	=	Kinetic theory of granular flow
kg	=	kilogram
kg/hr	=	kilogram per hour
kg/m^3	=	kilogram per cubic metre
kg/m-s	=	kilogram per metre-second
kW	=	kilowatt
kWth	=	kilowatt thermal
LHV	=	Lower heating value
LPG	=	Liquefied petroleum gas

LIST OF SYMBOLS AND ABBREVIATIONS (Cont')

M.C.	=	Moisture content
MJ/kg	=	megajoules per kilogram
MJ/Nm^3	=	Megajoules per normal cubic metre
MSW	=	Municipal solid wastes
MWe	=	Megawatt electricity
m	=	metre
min	=	minute
mm	=	millimeter
m/s	=	metre per second
m/s^2	=	metre per second squared
NO_X	=	Nitrogen x-oxide
OEA	=	Organic elemental analyzer
O_2	=	Oxygen
ΔP	=	Pressure drop through the bed
P9_1	=	Simplified air distributor model with feeding pipe
P9_2	=	Simplified air distributor model without feeding pipe
Pa	=	Pascal
R	=	Reaction
R^2	=	Coefficient of determination of a linear regression
SO_X	=	Sulfur x-oxide
SPB	=	Shredded plastic bag
SRW	=	Shredded rubber waste
s	=	second
TFM	=	Two-fluid model
TGA	=	Thermal gravimetric analyzer
VOF	=	Volume of fluid
W	=	Bed weight

LIST OF SYMBOLS AND ABBREVIATIONS (Cont')

A	=	Cross sectional area
^{0}C	=	Degree Celsius
C_d	=	Drag coefficient
D	=	Gas diffusion
d_p	=	Particle size/Surface-volume mean diameter of particles
F	=	Mass fraction of particles less than 45 µm
F_D	=	Fluid drag (drag force)
f	=	Drag function
g	=	Acceleration due to gravity
g_0	=	Radial distribution function expressing the statistics of the spatial arrangement of particles
H	=	Enthalpy (subscripts *g* and *s* denote the gas phase and solid phase)
H_i/H_0	=	Quasi-steady state bed height divided by initial bed height
h	=	Heat transfer coefficient between phases ($h_{sg} = h_{gs}$)
β_{gs}	=	Interphase (Fluid-solid) exchange coefficients
k	=	Reaction kinetic rate
L	=	Bed height
M_c	=	Molecular weight
Nu_s	=	Nusselt number
P_g	=	Gas pressure
$\Delta P/L$	=	Pressure drop per unit height
Re_s	=	Reynolds number
R_c	=	Reaction rate
S	=	Mass source term (subscripts *g* and *s* denote the gas phase and solid phase)
T_g	=	Gas temperature
U	=	Superficial gas velocity
U_{mf}	=	Minimum fluidization velocity

LIST OF SYMBOLS AND ABBREVIATIONS (Cont')

U_s	=	Mean velocity of solid
wt%	=	Weight percent/ Percentage by weight
X_j	=	Molar fraction of species *j*
Y_i	=	Mass fraction of species *i* entering the fine structures
μm	=	Micro meter
ε	=	Void fraction in the bed
ε_{mf}	=	Characteristic voidage/Voidage fraction
ϕ	=	Sphericity of bed solids
μ	=	Dynamic viscosity/Viscosity of gas in kg/m sec
μ_s, dil	=	Dilute viscosity
ρ	=	Density in kg/m^3 (subscripts *g* and *s* denote the gas phase and solid phase)
ρ_p	=	Density of particle
$\vec{v}$	=	Instantaneous velocity (subscripts *g* and *s* denote the gas phase and solid phase)
$\overrightarrow{v_s'}$	=	Solid fluctuating velocity
λ_g	=	Gas thermal conductivity
λ_j	=	Thermal conductivity of species *j*
λ_s	=	Bulk viscosity
α	=	Volume fraction (subscripts *g* and *s* denote the gas phase and solid phase)
γ	=	Rate of dissipation of the fluctuating energy due to inelastic collision
γ_c	=	Stoichiometric coefficient
τ	=	Stress tensor (subscripts *g* and *s* denote the gas phase and solid phase)
Θ_s	=	Granular temperature
β	=	Interface momentum transfer coefficient
τ_p	=	Particulate relaxation time
e_w	=	Restitution coefficient between silica sand and wall

CHAPTER 1
INTRODUCTION

1.1 Rationale/Problem Statement

With respect to global issues of sustainable energy, attention to biomass utilization has been increasing as a potential source of renewable energy. Replacing fossil fuels with biomass fuel is one option that countries may wish to consider in controlling CO_2 emissions [1]. Compared to coal, biomass fuels generally have very low sulfur content [2], and therefore the use of biomass can also lower SO_x emissions. However, increasing utilization of biomass has some drawbacks due to its poor physical and chemical properties. The high moisture content is one of the problematic properties, which an alternative technology that can be applied to the utilization of high-moisture biomass fuels is co-processing with other fuels of low moisture content. Considering the vast amount of plastic waste generated and its high heat content with low moisture content, plastic bag (High Density Polyethylene type) after being separated from MSW can be considered as a high quality fuel.

Although direct combustion is the most widely used technology for biomass energy conversion, gasification has become one of the most promising new technologies. This is due to the flexible utilization of the products, which is fuel gas, from gasification and the potential reduction of gaseous pollutants, such as NO_x. The quality of fuel gas product from gasification is dependent on the type of biomass, the operating conditions and the system configuration. All of these are considered to have effects on the chemical reactions as well as the physical movement inside the system, which in turn influence the amount and quality of the products. Therefore, to successfully design and operate a gasification system, understanding of the system characteristics upon biomass gasification is essential. So far, both experimental studies of factors affecting biomass gasification in various reactor configurations and model simulations to predict what happen inside the reactor in both macro- and micro level have been carried out. Computational fluid dynamics (CFD) codes were developed to explain the thermodynamics and hydrodynamics behavior; however, in most studies, the model simulations under cold flow (ambient temperature and non-reactive considered) condition were investigated, with a limited number of the studies

under elevated temperature (hot sand with heat transfer and non-reactive considered) condition.

Among various types of gasification technologies available, the fluidized-bed type has been found to have several advantages, especially its fuel flexibility in term of properties and sizes, and the high heat and mass transfer. A bubbling fluidized bed gasifier (BFBG), previously developed in this laboratory, is chosen for this study to investigate the high-moisture biomass gasification both experimentally and by model simulation. The findings from this study will gain information of developing a promising solution for utilizing high-moisture biomass fuels and also decreasing the amount of plastic waste in the waste stream through energy recovery. Furthermore, the hydrodynamic behaviors inside bed zone of non-simplified and simplified air distributor model of the BFBG (both under cold flow condition and elevated temperature condition) will be obtained from this study for further improvement of gasification system design and operation.

1.2 Literature review

A number of studies focusing on biomass gasification in fluidized bed reactors have been carried out. Various fuels have been used, including agricultural wastes, wood or municipal solid wastes (MSW). Factors studied normally include the air-to-fuel ratio or equivalent ratio (ER), gasifier bed temperature and types of biomass. These have been the subject of several experimental studies in bubbling fluidized bed gasification [3-8].

The effects of ER have been intensively studied by Gómez-Barea et al. [7] and Kaewluan and Pipatmanomai [8]. Although different biomass fuels were used in the two studies, i.e. untreated olive stone and rubber wood chips, respectively, the significant effects of ER on a series of parameters, such as reactor temperature, gas composition, lower heating value (LHV), gas yield, gasification efficiency and overall carbon conversion, were similarly observed. So far, most of gasification studies were carried out using agricultural wastes and woods, which normally have high moisture content (as receive). There was found that the biomass with high moisture content will take more time to achieve a complete degradation and decrease the CO evolution which results to the lower heat content of producer gas [9]. Furthermore, the proportion of tar in the product gas would increase due to incomplete cracking [10]. To reduce the moisture content, biomass is typically dried under the sunlight for small-scale applications. However, the

requirements of land and constant sunlight make it impractical for the necessary large-scale applications and installations of mechanical dryers, leading to additional investments and operating costs. Other advanced gasification technologies to directly process high moisture biomass such as plasma gasification [11, 12], hydrothermal gasification [13] have also been studied. However, these technologies have so far only been developed on a small scale and are projected to have very high capital cost when compared to conventional gasification technologies [12]. Anyway, there is an alternative technology which can be applied to the utilization of high-moisture biomass fuels. It is co-processing with other fuels of low moisture content. Coal, which generally has lower moisture content and higher heating values, has often been co-processed with biomass and municipal solid waste to help increase the reaction temperature by reducing the average moisture of the fuel mixture [14]. Co-gasification of high moisture biomass with waste materials has also been carried out. For example, Kaewluan and Pipatmanomai [15] studied the co-gasification of rubber woodchip with around 30% moisture content with shredded rubber waste (SRW) in a bubbling fluidized bed. The results showed that the gasification performance and the quality of product gas from co-gasification were significantly improved when compared to the gasification of pure woodchip. At only 20 wt% SWR addition, the performance was even better than the gasification of pre-dried woodchip of similar final average moisture content. Therefore, co-gasification can be considered an effective solution for not only to utilize high moisture fuels, but also to dispose wastes with energy recovery.

Although the effects of operating conditions have been widely studied experimentally in several types of biomass gasification and co-gasification, the fundamental phenomena and the mechanisms inside the bubbling fluidized bed reactor are still somewhat obscure. Furthermore, the impact of flow behavior on the bubbling fluidized bed gasification is also interesting as these data cannot be obtained through the experiments. Therefore, the uses of computer power through a computational fluid dynamics (CFD) have become a boon to figure out and understand the hydrodynamic behavior of the reactor to successfully design and operate the BFBG system. Simulations are becoming faster and models more accurate, allowing detailed predictive simulation to compare to the experimental data. In recent years, the models for fluidized beds are divided into two main categories, i.e., discrete element method (DEM) and two-fluid model (TFM) [16, 17]. The DEM, which is based on molecular dynamics, is a simple numerical model by which interactions from multi-body collisions can be calculated. It is also called the

Euler-Lagrange approach. In this model, the fluid phase is treated as a continuum, while the particles are traced individually. This model has been used for investigating inter-particle force effect on fluidization characteristics [18, 19], mixing and segregation characteristics [20, 21], particle residence time [22], and minimum fluidization velocity [23] in the bubbling fluidized bed. For the TFM, which is also called Euler-Euler approach, all phases are considered to be continuous and fully interpenetrating. As a bubbling fluidized bed behaves like a chaos motion of a large numbers of particles in the bed, the fundamental procedure to closer complex particle stresses is resulted from multi-body collisions which are based on the DEM. However, many computational practices present that the DEM will normally take more computational time than the TFM if one requires modeling complex systems like BFBG with the millions of particles (e.g. Gera et al. [24], Chiesa et al. [25]). Furthermore, the TFM is more convenient when making quantifiable decisions for an engineering design, as TFM is able to obtain the mean particulate flow fields. Computational simulations which were done by several groups have been shown feasible to compute the observed bubbles and the flow regime by using TFM. Dig and Gidaspow [26] found that the model based on TFM predicts well the time-averaged and instantaneous porosity in two-dimensional bubbling fluidized beds. Gamwo et al. [27] also found that TFM predicts well the solids flow pattern and the axial solids velocity profiles in a bubbling fluidized bed.

To improve the descriptions of particle collisions, the kinetic theory of granular flow (KTGF) has been introduced into the TFM. The kinetic theory formulation includes an interaction term between gas turbulence and particle fluctuations in the granular temperature equation [28]. Enwald and Almstedt [29] found that the KTGF approach for granular flow allows the determination of the pressure and viscosity of the solid in place of empirical relations. Yu at el. [17] developed a new numerical model based on the TFM including the KTGF and complicated reactions to simulate the comprehensive model of BFBG and found that the flow behaviors of gas and solid phases in the bed and freeboard could be predicted and the calculated results of exit gas composition were in agreement with the experimental data. The KTGF approach has also been extended to binary mixtures studies as a mixing/segregation phenomena is an important one in the bubbling fluidized beds consisting of particles of different sizes and/or densities. Based on KTGF, the multi-fluid model with a gas phase and two particle phases has been used to simulate flow behavior in many research groups. Huilin et al. [30] derived a model using kinetic theory

of dense gases to simulated flow behavior of binary mixture differing in particle sizes with the same density in the gas bubbling fluidized bed and found that the fluidization behavior is strongly influenced by the variations of average particle diameter and mass fraction in the bed. Cooper and Coronella [31] modeled flow behavior of binary particles in a gas fluidized bed, to predicted the realistic bubbles, and observed segregating jump in a selected point in the bed. Sun and Battaglia [32] performed simulations with and without particle rotation to study segregation phenomena in a bi-dispersed gas bubbling fluidized bed and claimed that with particle rotation in the kinetic theory model and slightly friction considered better captures the bubble dynamics and time-averaged bed behavior. Huilin et al. [33] simulated the flow behavior of particles mixing or segregating in bubbling fluidized beds by using the Euler-Euler approach with KTGF, and found that better mixing or segregation reduction of particles may be obtained by increasing fluidizing velocity in a bubbling fluidized bed.

Computational fluid dynamic (CFD) simulations of fluidized beds have presented a lot of challenges, such as computational, modeling, and numerical challenges. Developing CFD skills need to provide the fundamental of the fluid dynamics behind complex engineering flows and the fundamental of the numerical solution algorithms on which the CFD codes are based. FLUENT is one of the main commercially available CFD codes, which base on the finite volume method. It has been focused to use and provide a comprehensive model in several researches. Benyahia et al. [34] used a CFD package by FLUENT to simulate gas-particle flow behavior in the riser section of a circulating fluidized bed. This approach treated each phase separately, and the link between the gas and particle phases was through drag, turbulence, or energy dissipation due to particle fluctuation. Gas and particle flow profiles were obtained for velocity, volume fraction, pressure, and turbulence parameters for each phase. The computational values agreed well with the experimental results and also showed that the inlet and outlet designed have significant effects on the overall gas and solid flow patterns and cluster formations in the riser. Cooper and Coronella [31] used FLUENT to performed a series of unsteady, three-fluid CFD simulations, and found that the simulated bed is well mixed axially. The simulated results also showed that gas velocity, maximum packing fraction, and solids composition do not affect the extent of mixing. From the simulations, it was possible to identify the solids wake trailing rising gas bubbles by looking at the vertical solid flux.

Comparisons of the simulation with the experimental results validate the utility of these techniques, and give insights into the mixing and segregation phenomena in fluidized beds.

According to those studies, the majority of bubbling fluidized bed behavior studies was investigated through computer power support, i.e. the commercial FLUENT package, in the case of two-dimensional simulations, and focused on the simulation under cold flow condition with a limited number of elevated temperature conditions. Therefore, the hydrodynamic behavior of bubbling fluidized beds will be studied in case of three-dimensional simulations, both under cold flow condition and elevated temperature condition, in this research in order to understand a reality of flow behaviors and to gain an information to successfully design and operate a bubbling fluidized bed gasifier.

1.3 Research Objectives

1.3.1 To examine the technical feasibility of the gasification of high-moisture rubber woodchips with plastic waste in a bubbling fluidized bed gasifier with the purpose of developing a promising solution for utilizing high-moisture biomass and the purpose of developing an environmentally acceptable process to decrease the amount of plastic waste in the waste stream through energy recovery.

1.3.2 To investigate the hydrodynamic behaviors inside bed zones of non-simplified and simplified air distributors in a bubbling fluidized bed gasifier model under cold flow (ambient temperature and non-reactive considered) conditions by using FLUENT.

1.3.3 To investigate the hydrodynamic behaviors inside bed zones of non-simplified and simplified air distributors in a bubbling fluidized bed gasifier model under elevated temperature (hot sand with heat transfer and non-reactive considered) conditions by using FLUENT.

CHAPTER 2
THEORIES

2.1 Gasification Technology

Gasification is a process that converts carbonaceous materials, such as coal or biomass, into carbon monoxide and hydrogen by reacting the raw material at high temperatures with a controlled amount of oxygen. The resulting gas mixture is called synthesis gas or syngas. The syngas may be burned directly in internal combustion engines to produce methanol and hydrogen, or converted via the Fischer-Tropsch process into synthetic fuel [1]. These give gasification the potential for high efficiency.

The gasification of fossil fuels is currently widely used on industrial scales to generate electricity. However, almost any types of organic materials can be used as the raw material for gasification as gasification is a very efficient method for extracting energy from many different types of organic materials, such as wood, biomass, or even plastic waste. So, gasification may be an important technology for renewable energy. Especially, biomass gasification is carbon neutral. It also has applications as a clean waste disposal technique.

Biomass has been extensively used to fully or partially substitute fossil fuels for heat and power production in combustion boilers. More recently, biomass gasification has increased its popularity mainly due to its wide range of operated capacity, the flexible utilization of fuel gas product, and the potential reduction of gaseous pollutants such as NO_x [35]. Maximizing biomass utilization potential has become the main focus especially in response to the commitment in CO_2 reduction in many countries.

Several gasification processes for thermal treatment of biomass and waste are also under development as an alternative to incineration. Their gasification has several principal advantages over incineration:

- The necessary extensive flue gas cleaning may be performed on the syngas instead of the much larger volume of flue gas after combustion.
- Electrical power may be generated in engines and gas turbines, which are much cheaper and more efficient than the steam cycle used in incineration. Even fuel cells may potentially be used, but these have rather severe requirements regarding the purity of the gas.

- Chemical processing of the syngas may produce other synthetic fuels instead of electricity.
- Some gasification processes treat ash containing heavy metals at very high temperatures so that it is released in a glassy and chemically stable form.

2.1.1 Chemical processes

Gasification relies on chemical processes at elevated temperatures >700°C, which discriminate it from biological processes, such as anaerobic digestion, that produce biogas. In a gasifier, the carbonaceous material undergoes several different physicochemical processes [36, 37]:

- *The pyrolysis (or devolatilization) process* occurs as the carbonaceous particles heat up. Volatiles are released and char is produced. The process is dependent on the properties of the carbonaceous material and determines the structure and composition of the char, which will then undergo gasification reactions. This process can be represented by the general Reaction 2.1:

Carbonaceous material + Heat → Char + Light Gases + Vapors or Liquid (Tar) (R 2.1)

- *The combustion (or oxidation) process* occurs as the volatile products and some of the char reacts with oxygen to form CO_2 and H_2O, which provides heat for the subsequent gasification reactions (endothermic reactions). Letting C represent a carbon-containing organic compound, the basic reactions are presented in Reactions 2.2 and 2.3:

$C + O_2 \rightarrow CO_2 + Heat$ (R 2.2)

$H_2 + 0.5O_2 \rightarrow H_2O + Heat$ (R 2.3)

Reaction 2.2 is a complete combustion. While the steam production, known as hydrogen oxidation, is presented in Reaction 2.3. It is a homogeneous volatile oxidation.

- *The gasification process* occurs as the char reacts with carbon dioxide and steam to produce carbon monoxide and hydrogen, via the Reactions 2.4 to 2.6:

$C + H_2O \rightarrow H_2 + CO - Heat$ (R 2.4)

$C + CO_2 \rightarrow 2CO - Heat$ (R 2.5)

$CO + H_2O \rightarrow CO_2 + H_2 + Heat$ (R 2.6)

Reaction 2.4 is a water-gas reaction. It is a partial oxidation of carbon by steam. Reaction 2.5 is known as the Boudouard Reaction. Both of these reactions are endothermic reaction. While the reduction of steam by carbon monoxide to produce hydrogen is shown in Reaction 2.6, known as water-gas shift reaction, is exothermic reaction. Methane could also be formed in the gasifier through Reaction 2.7:

$C + 2H_2 \rightarrow CH_4 + Heat$ (R 2.7)

Methane formation is preferred when the gasification products are used as a feedstock for other chemical process, and also preferred in IGCC applications as the high heating value of methane.

In essence, a limited amount of oxygen or air is introduced into the reactor to allow some of the organic material to be burned to produce carbon monoxide and energy, which drives a second reaction that converts further organic material to hydrogen and additional carbon monoxide.

2.1.2 Types of gasifiers

Gasifiers can be divided into four types depending on how the fuel and gas contact each other [37]:

- *Fixed or moving bed*: The gasification medium flows through, and thus, comes into contact with a fixed bed of solid fuel particles. This type of gasifier has been in use for the longest time and therefore uses the oldest technology. Its advantage is that it is quite simple and robust. Since the bed is fixed, the design in normally very simple. A disadvantage is that the plant size is limited. The up-scaling is limited due to the fixed bed technology since it is hard to reach a large fuel bed with uniform temperature distribution (the larger the bed, the larger the temperature differences).

- *Spouted bed*: The gasification medium penetrates through a thick bed of relatively coarse particles at high velocity. The solids are carried to the bed surface and rain down like a fountain to be re-entrained again.

- *Entrained bed*: Entrained bed gasifiers are available in much larger capacities (>100 MWe) than other types, but they are more commonly used for fossil fuels. Their use

for biomass gasification is limited as they require the fuel particles to be very fine (80-100 μm).

- *Fluidized bed (Bubbling or Circulating)*: The fluidized bed or bed material enhances the heat exchange between the fuel particles, and increases mixing and kinetics, thus increasing overall gasifier efficiency and fuel throughput. The risk for bed agglomeration, which is also one of the major disadvantages for biomass fuels, makes it necessary to exchange the bed material with proper intervals. The fluidization agent, air or steam, is normally added in several steps. The primary air is added in the bottom of the bed as fluidizing medium (gasification medium). The velocity of the primary air must at least reaches the minimum fluidization velocity (U_{mf}) if not the air will only trickle the sand with no bubbles formed. As the air velocity is increased higher than U_{mf}, the bed begins to float. The bubbles are getting bigger and will finally erupt quite heavily in the surface of the bed. This behavior occurs in bubbling fluidized bed (BFB). In circulating fluidized bed (CFB), the air is operated at much higher velocity that the particles inside the bed are entrained in the gas stream. A large cyclone installed at the top of the furnace will capture the bed material as well as other particles and returns them to the bottom of the bed region. Due to the intense gas-solid mixing in a fluidized bed, the different zones of drying, pyrolysis, oxidation and reduction cannot be distinguished, but the temperature is uniform throughout the bed. In fluidized-bed, the temperature is relatively low, approximately 750° to 900°C when compared with fixed-bed reactor of which the temperature in the hearth zone may be as high as 1,200°C.

The advantages of BFBGs are that they allow higher rates of throughput than do fixed bed gasifiers, and also allow in good mixing, optimized kinetics, particle/gas contact and heat transfer as well as longer residence times. These factors contribute to high carbon conversion rates and, consequently, high yields. The BFBG is tolerant to particle size and fluctuations in feed quantity and moisture. No real technical scale-up limit, but size may be limited by availability of biomass.

The environmental and operating characteristics of a gasifier are the direct results of its hydrodynamics and thermodynamics. For this reason, the performance of a fluidized bed gasifier drops significantly when the operation of its reactor deviates from the designed fluidization regime. Therefore, understanding of the hydrodynamics and thermodynamics behavior in the reactor of a fluidized bed unit is very important.

2.2 Fluidization Hydrodynamics

When a fluid (gas), i.e. air, is passed upwards through a bed of solid particles at low flow rates, the fluid spreads through the void spaces between stationary particles without disturbing the bed. This condition represents *a fixed bed* or *packed bed*.

The pressure drop per unit height of a fixed bed ($\Delta P/L$) of uniformly sized particles (d_p) is correlated, as shown in Equation 2.1 (Ergun Equation):

$$\frac{\Delta P}{L} = 150\frac{(1-\varepsilon)^2}{\varepsilon^3}\frac{\mu U}{(\phi d_p)^2} + 1.75\frac{(1-\varepsilon)}{\varepsilon^3}\frac{\rho_g U^2}{\phi d_p} \qquad \text{(E 2.1)}$$

where ε is the void fraction in the bed, ϕ is the sphericity of bed solids, μ is the dynamic viscosity, ρ_g is the density of gas, and d_p is the surface-volume mean diameter of particles. The superficial gas velocity (U) is defined as the gas flow rate per unit cross section of the bed [38].

If the gas flow rate through the fixed bed is increased, the pressure drop due to the fluid drag continues to rise until the superficial gas velocity reaches a critical value known as the minimum fluidization velocity (U_{mf}). At U_{mf}, the fixed bed transforms into *an incipiently fluidized bed*. In this state, the body of solid particles behaves like a liquid. Since the pressure drop across the bed equals the weight of the bed, the fluid drag (drag force) is written as:

$$F_D = \Delta PA = AL(1-\varepsilon)(\rho_p - \rho_g)g \qquad \text{(E.2.2)}$$

where ρ_p is the density of the particle, g is the acceleration due to gravity, A is the cross-sectional area, and L is the bed height [37].

From Equation 2.2, the minimum fluidization condition is written as:

$$\frac{\Delta P}{L_{mf}} = (1-\varepsilon_{mf})(\rho_s - \rho_g)g \qquad \text{(E 2.3)}$$

At minimum fluidization, the bed behaves as a pseudoliquid. For Group B and D particles, a further increase in gas flow causes the excess gas to flow in the form of bubbles. The gas-solid suspension around the bubbles and elsewhere in the bed is called the emulsion phase. The superficial gas velocity through this phase is of the order of U_{mf} and it has a characteristic voidage ε_{mf}. The U_{mf} is found by combining Equations 2.1 and 2.3. In general, for isotropic-shaped solids this gives a quadratic in U_{mf} [38]:

$$\frac{1.75}{\varepsilon_{mf}^3 \phi_s}\left(\frac{d_p U_{mf} \rho_g}{\mu}\right)^2 + \frac{150(1-\varepsilon_{mf})}{\varepsilon_{mf}^3 \phi_s^2}\left(\frac{d_p U_{mf} \rho_g}{\mu}\right) = \frac{d_p^3 \rho_g (\rho_s - \rho_g)}{\mu^2} \qquad \text{(E 2.4)}$$

In the special case of very small particles, $Re_p < 20$, the U_{mf} is obtained from:

$$U_{mf} = \frac{(\phi d_p)^2}{150}\frac{(\rho_s - \rho_g)}{\mu} g\left(\frac{\varepsilon_{mf}^3}{1-\varepsilon_{mf}}\right) = \frac{d_p^2(\rho_s - \rho_g)g}{1650\,\mu} \qquad \text{(E 2.5)}$$

For very large particles, $Re_p > 1000$, the U_{mf} is obtained from:

$$U_{mf}^{\ 2} = \frac{\phi d_p}{1.75}\frac{(\rho_s - \rho_g)}{\rho_g} g\varepsilon_{mf}^3 = \frac{d_p(\rho_s - \rho_g)g}{24.5\rho_g} \qquad \text{(E 2.6)}$$

where Re_p is the Reynolds Number for particles, $Re_p = \frac{d_p U_{mf} \rho_g}{\mu}$.

A fluidized bed of Group A particles does not start bubbling as soon as the U exceeds U_{mf}, but instead the bed starts expanding. The bubbles start appearing when U exceeds another characteristic value called minimum bubbling velocity (U_{mb}). The U_{mb} is given as:

$$U_{mb} = 2.07\exp(0.716F) d_p\left[\frac{\rho_g^{0.06}}{\mu^{0.347}}\right] \qquad \text{(E 2.7)}$$

where F is the mass fraction of particles less than 45 μm, d_p is the surface-volume mean diameter of particles in m, ρ_g is the density of gas in kg/m^3, and μ is the viscosity of gas in kg/m-sec [39].

If the gas flow rate through the bubbling fluidized bed is increased, the bed starts expanding. A continued increase in the velocity may eventually show a change in the pattern of bed expansion, indicating a transition into a new regime called a *turbulent bed*.

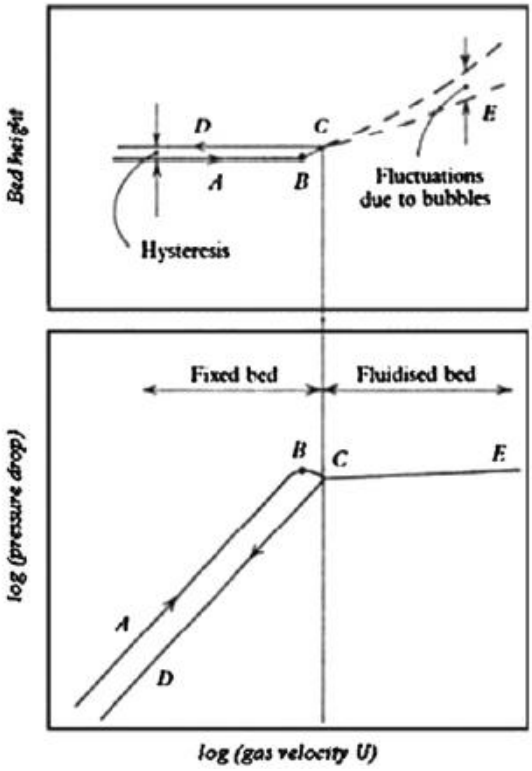

Figure 2.1 Typical curves for gas fluidized bed of particles [40].

Typical results of a gas fluidized bed of particles are shown in Figure 2.1 where the pressure drops across the bed and its height are plotted as a function of the superficial gas velocity [41]: starting from line *A* for slowly increasing flow, the overall pressure drop is slightly more than enough to support the weight of the particles. Above point *B*, a slight increase in flow velocity frees the particles, the pressure drop becomes just enough to support their weight and, consequently, point *C* is commonly defined as a point of incipient fluidization, characterized by the minimum fluidization velocity (U_{mf}) and the voidage fraction (ε_{mf}). If the flow rate is decreased from point *C*, the particles are more loosely packed so the bed height is greater and the pressure drop smaller as shown on line *D*. For a gas fluidized bed in which the gas velocity is higher than U_{mf}, some of the gas may pass through the bed as bubbles which agitate the bed and consequently its height fluctuates as indicated in region *E*. The formation of bubbles characterizes the bubbling fluidized bed;

with still greater flows the bubbles grow and appear more frequently, until the bed becomes slugging. A further increase in flow rate carries particles out of the reactor according to the phenomena of pneumatic transport. After the gas reaches the minimum fluidization velocity, bubbles form and during their rise to the surface of the bed, they are not only increased in size and coalesce, they are also divided.

In general, fluidized bed models consider three things. First is the division between the bubble phase and the particulate phase (emulsion or dense phase). Second is the degree of mixing in the particulate phase. And third is the transfer of gas between the two phases. The reason for developing a conceptual model for the bubbling bed is to estimate its main features, such as velocities of gas and solid, volume fractions and contacting regimes.

2.3 Computational Fluid Dynamics (CFD) Modeling

Versteeg and Malalasekera [42] gave a meaning of computational fluid dynamics (CFD), which is "CFD is the analysis of systems involving fluid flow, heat transfer and associated phenomena such as chemical reactions by means of computer-based simulation." Figure 2.2 shows the framework for CFD modeling of fluidized bed gasifier. The use of CFD to predict internal and external flows has risen dramatically in the past decade. The solution of fluid flow problems by means of CFD was the domain of the academic and research in 1980s. Developing CFD skills need to provide the fundamental of the fluid dynamics behind complex engineering flows and the fundamental of the numerical solution algorithms on which the CFD codes are based.

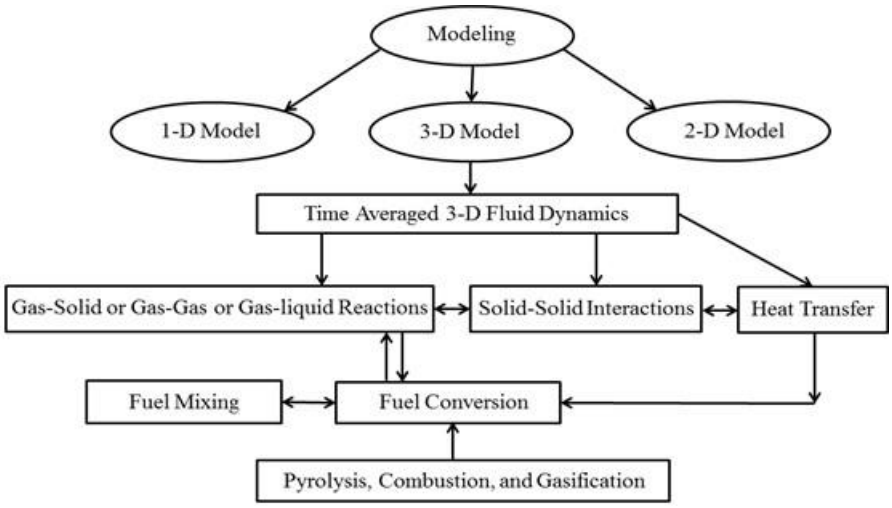

Figure 2.2 Framework for CFD modeling [43].

Prior to setting up and running a CFD simulation, there is a stage of identification and formulation of the flow problem in terms of the physical and chemical phenomena that need to be considered in the CFD code. Simplified problem is also needed for assumption making to reduce the complexity to a manageable level. All assumptions that have been made will govern the quality of the information generated by CFD.

Compared to the physical experiment operation, CFD modeling is more economical, timely, safe and easy to scale-up. CFD codes turn computers into a virtual laboratory and perform the equivalent "numerical experiments" conveniently providing insight, foresight and return on investment. Various numerical techniques known as direct numerical simulation (DNS), vortex dynamics and discretization methods have been employed in the solution of the CFD model equations [44]. The most widely used numerical techniques are discretization methods mainly including finite difference (usually based on Taylor's series, polynomial expansions), finite elements (based on calculus of variations, and the method-of-weighted-residuals) and finite volumes method (based on control-volume formulation). Finite difference techniques are rarely used in engineering flows due to the difficulties in the handling of complex geometry [45]. Finite elements are used in the commercial packages of FIDAP and POLYFLOW. Finite volumes are now the most commonly used approach in CFD code development for its ease in the understanding, programming and versatility.

FLUENT is one of the main commercially available CFD codes, which is based on the finite volume method. The finite volume method was originally developed as a special finite difference formulation. The numerical algorithm consists of the following step:

- Formal integration of the governing equations of fluid flow over all the (finite) control volumes of the solution domain.
- Discretisation involves the substitution of a variety of finite-difference-type approximations for the terms in the integrated equation representing flow processes such as convection, diffusion, and sources. This converts the integral equations into a system of algebraic equations.
- Solution of the algebraic equations by an iterative method.

The FLUENT provides comprehensive modeling capabilities for a wide range of incompressible and compressible, laminar and turbulent fluid flow problems. Steady-state or transient analyses can be performed. In FLUENT, a broad range of mathematical models for transport phenomena (such as heat transfer and chemical reactions) is combined with

the ability to model complex geometries. Examples of FLUENT applications include laminar non-Newtonian flows in process equipment; conjugate heat transfer in turbo machinery and automotive engine components; pulverized coal combustion in utility boilers; external aerodynamics; flow through compressors, pumps, and fans; and multiphase flows in bubble columns and fluidized beds.

A very useful group of models in FLUENT is the set of free surface and multiphase flow models. A large number of flows encountered in nature and technology are a mixture of these phases. The physical phases of matter are gas, liquid, and solid, but the concept of phase in a multiphase flow system is applied in a broader sense. In multiphase flow, a phase can be defined as an identifiable class of material that has a particular inertial response to and interaction with the flow and the potential field in which it is immersed. For example, different-sized solid particles of the same material can be treated as different phase because each collection of particles with the same size will have a similar dynamical response to the flow field.

Multiphase flow can be classified into four categories: gas-liquid or liquid-liquid flows, gas-solid flows, liquid-solid flows, and gas-solid-liquid flows. Fluidized beds are grouped as a gas-solid flow category. They consist of a vertical cylinder containing solid particles where gas (air) is introduced through a distributor. The gas rising through the bed suspends the solid particles. Depending on the gas flow rate, bubbles appear and rise through the bed, intensifying the mixing within the bed.

Currently there are two approaches for the numerical calculation of multiphase flows: the Euler-Lagrange approach and the Euler-Euler approach.

- *The Euler-Lagrange Approach*: The Lagrangian discrete phase model follows the Euler-Lagrange approach. It is a simple numerical model by which interactions from multi-body collisions can be calculated. The fluid phase is treated as a continuum by solving the time-averaged Navier-Stokes equations, while the dispersed phase is solved by tracking a large number of solid particles, bubbles, or droplets through the calculated flow field. The dispersed phase can exchange momentum, mass, and energy with the fluid phase. A fundamental assumption made in this model is that the dispersed second phase occupies a low volume fraction, even though high mass loading is acceptable. The particle or droplet trajectories are computed individually at specified intervals during the fluid phase calculation. This makes the model appropriate for the modeling of spray dryers, coal and liquid fuel combustion, and some particle-laden flows, but inappropriate for the

modeling of liquid-liquid mixtures, fluidized beds, or any application where the volume fraction of the second phase is not negligible.

- *The Euler-Euler Approach*: In the Euler-Euler approach, the different phases are treated mathematically as interpenetrating continua. Since the volume of a phase cannot be occupied by the other phases, the concept of a phase's volume fraction is introduced. These volume fractions are assumed to be continuous functions of space and time and their sum is equal to one. Conservation equations for each phase are derived to obtain a set of equations, which have similar structure for all phases. These equations are closed by providing constitutive relations that are obtained from empirical information, or, in the case of granular flows, by application of kinetic theory. There are three different available Euler-Euler multiphase models: the volume of fluid (VOF) model, the mixture model, and the Eulerian model.

The VOF Model: This is a surface-tracking technique applied to a fixed Eulerian mesh. It is designed for two or more immiscible fluids where the position of the interface between the fluids is to be studied. In the VOF model, a single set of momentum equations is shared by the fluids, and the volume fraction of each of the fluids in each computational cell is tracked throughout the domain. Applications of the VOF model include stratified flows, free-surface flows, filling, sloshing, the motion of large bubbles in a liquid, the motion of liquid after a dam break, the prediction of jet breakup (surface tension), and the steady or transient tracking of any liquid-gas interface.

The Mixture Model: This is designed for two or more phases (fluid or particulate). As in the Eulerian model, the phases are treated as interpenetrating continua. The mixture model solves for the mixture momentum equation and prescribes relative velocities to describe the dispersed phases. Applications of the mixture model include particle-laden flows with low loading, bubbly flows, sedimentation, and cyclone separators. The mixture model can also be used without relative velocities for the dispersed phases to model homogeneous multiphase flow.

The Eulerian Model: This is the most complex of the multiphase models that solves a set of *n* momentum and continuity equations for each phase. Coupling is achieved through the pressure and interphase exchange coefficients. The manner in which this coupling is handled depends upon the type of phases involved; granular (fluid-solid) flows are handled differently than non-granular (fluid-fluid) flows. For granular flows, the properties are obtained from application of kinetic theory. Momentum exchange between

the phases is also dependent upon the type of mixture being modeled. Applications of the Eulerian multiphase model include bubble columns, risers, particle suspension, and fluidized beds.

In addition, robust and accurate turbulence models are a vital component of the FLUENT suite of models. The turbulence models provided have a broad range of applicability, and include the effects of other physical phenomena, such as buoyancy and compressibility. Particular care has been devoted to addressing issues of near-wall accuracy via the use of extended wall functions and zonal models. Various modes of heat transfer can be modeled, including natural, forced, and mixed convection with or without conjugate heat transfer, porous media, etc. The set of radiation models and related sub-models for modeling participating media are general and can take into account the complications of combustion. A particular strength of FLUENT is its ability to model combustion phenomena using a variety of models, including eddy dissipation and probability density function models. A host of other models that are very useful for reacting flow applications are also available, including coal and droplet combustion, surface reaction, and pollutant formation models.

2.4 Mathematical Model

This model is based on the fundamental concept of interpenetrating continua for multiphase mixers in which different phases can be present at the same time in the same computational volume. The fundamental equations of mass and momentum conservation are solved for each considered phase. Appropriate constitutive equations have to be specified in order to describe the physical properties of each phase and to close the conservation equations. In the model, solids viscosity and pressure are derived by considering the random fluctuation of particle velocity and its variations due to particle-particle collisions and the actual flow field. The solids viscosity and pressure can be computed as a function of granular temperature at any time and position. Particles are considered smooth, spherical, inelastic, and undergoing binary collisions.

For flows involving heat transfer or compressibility, an additional equation for energy conservation is solved. While for flows involving species mixing or reactions, a species conservation equation is solved, or if the non-premixed combustion model is used, conservation equations for the mixture fraction and its variance are solved.

2.4.1 Basic governing equations

Following are the basic fundamental equations for mass, momentum, energy and species, respectively for the gas phase. These are basic equations of flow for gas phase when combustion and gasification is taking place in fluidized bed. For multiphase flow these equations are modified and presented in Section 2.4.2. The detail of these basic equations, as follows, could be referred from Warnatz et al. [46] and Bakul et al. [47].

- *Mass conservation equation*

$$\frac{\partial}{\partial t}\left(\rho_g\right) + \nabla \cdot \left(\rho_g \vec{v}_g\right) = S_g \qquad \text{(E 2.8)}$$

- *Momentum equation*

$$\frac{\partial}{\partial t}\left(\rho_g \vec{v}_g\right) + \nabla \cdot \left(\rho_g \vec{v}_g \vec{v}_g\right) = -\nabla P_g + \nabla \cdot \left(\mu \nabla \vec{v}_g\right) + S_g \qquad \text{(E 2.9)}$$

- *Energy equation*

$$\frac{\partial}{\partial t}\left(\rho_g H_g\right) + \nabla \cdot \left(\rho_g \vec{v}_g H_g\right) = \nabla\left(\lambda_g \nabla T_g\right) + S_H \qquad \text{(E 2.10)}$$

- *Species transport equation*

$$\frac{\partial}{\partial t}\left(\rho_g Y_i\right) + \nabla \cdot \left(\rho_g \vec{v}_g Y_i\right) = \nabla\left(D \nabla(\rho \mathrm{Y_i})\right) + S_Y + R_f \qquad \text{(E 2.11)}$$

where $\rho_g, \vec{v}_g, \mu, \lambda_g, P_g, H_g, T_g, Y_i, D,$ and S are gas density, gas instantaneous velocity, viscosity, gas thermal conductivity, gas pressure, gas enthalpy, gas temperature, mass fraction of species *i* entering the fine structures, gas diffusion, and source term, respectively.

2.4.2 Eulerian-Eulerian two fluid CFD model with kinetic theory of granular flow (KTGF)

The Eulerian-Eulerian method which is one of the affordable CFD modeling approaches for performing simulations of gas-solid flow system inside fluidized bed with

combustion and gasification are presented as the general equations below. Details of these could be referred from Armstrong et al. [48] and Yu et al. [17].

- *Mass conservation equations*

The accumulation of mass in each phase is balanced by the convective mass flows

$$\frac{\partial}{\partial t}\left(\alpha_g \rho_g\right) + \nabla \cdot \left(\alpha_g \rho_g \vec{v}_g\right) = S_{gs} \quad \text{(E 2.12)}$$

$$\frac{\partial}{\partial t}\left(\alpha_s \rho_s\right) + \nabla \cdot \left(\alpha_s \rho_s \vec{v}_s\right) = S_{sg} \quad \text{(E 2.13)}$$

where $\alpha, \rho,$ and $\vec{v}$ represent the volume fraction, density, and instantaneous velocity and subscripts *g, s* denote the gas phase and solid phase, respectively. S is the mass source term due to heterogeneous reactions, which is expressed as given by Yu et al. [17]:

$$S_{sg} = -S_{gs} = M_c \sum \gamma_c R_c \quad \text{(E 2.14)}$$

where M_c, γ_c and R_c are molecular weight, stoichiometric coefficient, and reaction rate, respectively. Anyway, the source term will be neglected for the model simulation under cold flow conditions.

Moreover, source terms are also added into all relevant momentum and energy equations based on the assumption that the momentum and energy are carried along with the transferred mass.

The gas density is a function of the composition of the chemical species and the gas temperature. The gas fluid is considered to be a weakly compressible flow. Thus, it is given by

$$\rho_g = \frac{P}{RT \sum_{i=1}^{n} \frac{Y_i}{M_i}} \quad \text{(E 2.15)}$$

The solid mixture density is defined as a composition-dependent value:

$$\rho_s = \frac{1}{\sum_{i=1}^{m} Y_i / \rho_i} \quad \text{(E 2.16)}$$

- *Momentum conservation equations*

$$\frac{\partial}{\partial t}\left(\alpha_g \rho_g \vec{v}_g\right) + \nabla \cdot \left(\alpha_g \rho_g \vec{v}_g \vec{v}_g\right) = -\alpha_g \nabla P_g + \nabla \alpha_g \cdot \tau_g + \alpha_g \rho_g g - \beta_{gs}\left(\vec{v}_g - \vec{v}_s\right) + S_{gs} U_s \quad \text{(E 2.17)}$$

$$\frac{\partial}{\partial t}\left(\alpha_s \rho_s \vec{v}_s\right) + \nabla \cdot \left(\alpha_s \rho_s \vec{v}_s \vec{v}_s\right) = -\alpha_s \nabla P_s + \nabla \alpha_s \cdot \tau_s + \alpha_s \rho_s g + \beta_{gs}\left(\vec{v}_g - \vec{v}_s\right) + S_{sg} U_s \quad \text{(E 2.18)}$$

where P, τ, g, β_{gs},U_s represent the pressure, stress tensor, gravity force, interphase exchange coefficient, and mean velocity of a solid, respectively.

In the above equations, the stress tensor τ_g and τ_s are given by

$$\tau_g = \mu_g \left[\nabla \vec{\mathrm{v}}_{\mathrm{g}} + \left(\nabla \vec{\mathrm{v}}_{\mathrm{g}}\right)^{\mathrm{T}}\right] - \frac{2}{3}\alpha_g \mu_g \left(\nabla \vec{\mathrm{v}}_{\mathrm{g}}\right) \quad \text{(E 2.19)}$$

$$\tau_s = \mu_s [\nabla \vec{\mathrm{v}}_{\mathrm{s}} + (\nabla \vec{\mathrm{v}}_{\mathrm{s}})^{\mathrm{T}}] - \frac{2}{3}\mu_s (\nabla \vec{\mathrm{v}}_{\mathrm{s}}) + \lambda_s \cdot \nabla \vec{\mathrm{v}}_{\mathrm{s}} \quad \text{(E 2.20)}$$

here λ_s is bulk viscosity, which based on expression given by Lun et al. [49] and can be defined as

$$\lambda_s = \frac{4}{5}\alpha_s \rho_s d_s g_0 (1-e)\left(\frac{\Theta_s}{\pi}\right)^{1/2} \quad \text{(E 2.21)}$$

For the collision and kinetic effects, the coefficient of restitution is introduced by Jenkins and Savage [50], and the equation of solid shear viscosity is defined as

$$\mu_s = \frac{\mu_{s,\mathrm{dil}}}{(1+e)g_0}\left[1 + \frac{4}{5}(1+e)g_0 \alpha_s\right]^2 + \frac{4}{5}\alpha_s^2 \rho_s d_s (1+e) g_0 \left(\frac{\Theta}{\pi}\right)^{1/2} \quad \text{(E 2.22)}$$

$$\mu_s, \mathrm{dil} = \frac{5\sqrt{\pi}}{96}\rho_s d_s \Theta^{1/2} \quad \text{(E 2.23)}$$

where μ_s, dil is the dilute viscosity and g_0 is the radial distribution function expressing the statistics of the spatial arrangement of particles.

$$g_0 = \left[1 - \left(\frac{\alpha_s}{\alpha_{s,max}}\right)^{1/3}\right]^{-1} \quad \text{(E 2.24)}$$

Equivalent to the thermodynamic temperature for gases, the granular temperature can be introduced as a measure for the fluctuating kinetic energy of the particles. The granular temperature Θ_s is defined as

$$\Theta_s = \frac{1}{3}\overrightarrow{v_s}^2 \quad \text{(E 2.25)}$$

where $\overrightarrow{v_s}$ is the solids fluctuating velocity.

The equation of conservation of a solid's fluctuating energy is given as

$$\frac{3}{2}\left[\frac{\partial}{\partial t}(\alpha_s \rho_s \Theta) + \nabla \cdot (\alpha_s \rho_s \overrightarrow{v_s} \cdot \Theta)\right] = -(P_s I + \alpha_s \tau_s) : \nabla \overrightarrow{v_s} + \nabla \cdot \kappa_s \nabla \Theta - \gamma \quad \text{(E 2.26)}$$

where $(P_s I + \alpha_s \tau_s) : \nabla \overrightarrow{v_s}$ is the generation of the fluctuating energy due to work done by shear stress in the particle phase; $\nabla \cdot \kappa_s \nabla \Theta$ is the conduction of the fluctuating energy; γ is the rate of dissipation of the fluctuating energy due to inelastic collisions.

The granular conductivity κ_s and the collisional rate of energy dissipation per unit volume γ are adopted as:

$$\kappa_s = \frac{2\kappa_{\text{dil}}}{(1+e)g_0}\left[1 + \frac{6}{5}(1+e)g_0\alpha_s\right]^2 + 2\alpha_s^2 \rho_s d_s \left(\frac{\Theta}{\pi}\right)^{1/2} \quad \text{(E 2.27)}$$

$$\kappa_{\text{dil}} = \frac{75\sqrt{\pi}}{384}\rho_s d_s \Theta^{1/2} \quad \text{(E 2.28)}$$

$$\gamma = 3(1-e^2)\alpha_s^2 \rho_s g_0 \Theta \left[\frac{4}{d_s}\left(\frac{\Theta}{\pi}\right)^{1/2} - \nabla \cdot \overrightarrow{v_s}\right] \quad \text{(E 2.29)}$$

The particle pressure represents the particle normal forces due to particle–particle interaction. Its description based on the kinetic theory of granular flow was developed. In this approach, both the kinetic and the collisional influence are taken into account. The kinetic portion describes the influence of particle translations, whereas the collisional term accounts for the momentum transfer by direct collisions [28]. The particle pressure is calculated as follows:

$$p_s = \alpha_s \rho_s \Theta [1 + 2 g_0 \alpha_s (1 + e)] \qquad \text{(E 2.30)}$$

In order to couple the two momentum balances in Equations 2.24 and 2.25, a model for the interphase force is required. For $\alpha_g \leq 0.8$, the pressure drop due to friction between gas and particles can be described by the Ergun Equation. Thus, the interface momentum transfer coefficient (interphase exchange coefficient), β_{gs}, in this porosity range [30, 51] becomes:

$$\beta_{gs} = 150 \frac{\alpha_s^2 \mu_g}{\alpha_g d_s^2} + 1.75 \frac{\rho_g \alpha_s |\overrightarrow{v_g} - \overrightarrow{v_s}|}{d_s} \qquad \text{(E 2.31)}$$

for $\alpha_g > 0.8$, such a relation for the pressure drop leads to the following expression for the interface momentum transfer coefficient:

$$\beta_{gs} = \frac{3}{4} C_\mathrm{d} \frac{\alpha_s \alpha_g \rho_g |\overrightarrow{v_g} - \overrightarrow{v_s}|}{d_s} \alpha_g^{-2.65} \qquad \text{(E 2.32)}$$

where the drag coefficient C_d is given by

$$C_\mathrm{d} = 0.44; \qquad \text{for} \quad Re_s > 1000 \qquad \text{(E 2.33)}$$

$$C_\mathrm{d} = \frac{24}{Re_s}(1 + 0.15 Re_s^{0.687}) \qquad \text{for} \quad Re_s \leq 1000 \qquad \text{(E 2.34)}$$

where Re_s is the Reynolds number,

$$Re_s = \frac{\alpha_g \rho_g d_s |\overrightarrow{v_g} - \overrightarrow{v_s}|}{\mu_g} \qquad \text{(E 2.35)}$$

- *Energy conservation equation*

To describe the conservation of energy in a Eulerian multiphase, a separate enthalpy equation is written for each phase. Heat transfers in each phase and the heat exchange between two phases are taken into account but the viscous heating is neglected:

$$\frac{\partial}{\partial t}\left(\alpha_g \rho_g H_g\right) + \nabla\left(\alpha_g \rho_g \vec{v}_g H_g\right) = \nabla\left(\lambda_g \nabla T_g\right) + h_{gs}\left(T_g - T_s\right) + S_{gs} H_s \quad \text{(E 2.36)}$$

$$\frac{\partial}{\partial t}\left(\alpha_s \rho_s H_s\right) + \nabla \cdot \left(\alpha_s \rho_s \vec{v}_s H_s\right) = \nabla\left(\lambda_s \nabla T_s\right) + h_{sg}\left(T_s - T_g\right) + S_{sg} H_s \quad \text{(E 2.37)}$$

In which H is the specific enthalpy, λ is the mixture thermal conductivity, and $h\left(h_{sg} = h_{gs}\right)$ is the heat transfer coefficient between phases. SH is the source term that includes sources of enthalpy.

All variables are defined as follows:

$$H = \sum_j Y_j H_j \quad \text{(E 2.38)}$$

$$\lambda_g = \sum_j \frac{X_j \lambda_j}{\sum_j X_j \phi_{ij}} \quad \text{(E 2.39)}$$

where λ_j is the thermal conductivity for each chemical species in the mixture and is defined using kinetic theory as $\lambda_j = \mu_j \left(C_{\mathrm{p}j} + \left((5/4)\left(R/M_j\right)\right)\right)$; X_j is the molar fraction of species j, and

$$\phi_{ij} = \frac{\left[1+\left(\mu_i/\mu_j\right)^{1/2}\left(M_j/M_i\right)^{1/4}\right]^2}{\left[8\left(1+\left(M_i/M_j\right)\right)\right]^{1/2}} \quad \text{(E 2.40)}$$

The heat transfer coefficient, which is related to the solid phase Nusselt number (Nu_s), is given by

$$h_{sg} = \frac{6\lambda_g \alpha_s \alpha_g Nu_s}{d_s^2} \quad \text{(E 2.41)}$$

where Nu_s is proposed by Gunn [51]:

$$Nu_s = \left(7 - 10\alpha_g + 5\alpha_g^2\right)\left(1 + 0.7Re_s^{0.2}Pr^{1/3}\right) + \left(1.33 - 2.4\varepsilon_g + 1.2\alpha_g^2\right)Re_s^{0.7}Pr^{1/3} \quad \text{(E 2.42)}$$

2.4.3 Chemical reaction sub-models

As soon as the solid fuel enters inside the fluidized bed, process drying, devolatilization, combustion or gasification occur. The following sub-models will be incorporated in to basic equations of computational fluid dynamics to simulate the actual combustion and gasification processes in fluidized bed.

- *Devolatilization sub-model*

The devolatilization process begins when the solid fuel reaches a particular level. Many devolatilization [52] models have been developed in past. One-step global mechanisms and semi-global multi-step mechanisms can be basically distinguished. The simplified approaches define devolatization rates with single or two step Arrhenius Reaction schemes. The details of the one-step devolatilization mechanism is shown below

Carbonaceous material + Heat → Char + Light Gases + Vapors or Liquid (Tar) (R 2.8)

The reaction kinetic rate (k) can be expressed as a single-step Arrhenius fashion as $k = A\exp(-E_a/RT)$ and the devolatilization rate [53] is

$$\frac{-dm_p}{dt} = k\left[m_p - \left(1 - f_{v,0}\right)m_{p,0}\right] \quad \text{(E 2.43)}$$

Here A and E are numerical constants of reacting substances. For two-step Arrhenius reaction schemes, the kinetic devolatilization rate expressions of the form proposed by Kobayashi et al. [54] are as follows:

$$k_1 = A_1\exp\left(-E_1/RT\right) \quad \text{(E 2.44)}$$

$$k_2 = A_2\exp\left(-E_2/RT\right) \quad \text{(E 2.45)}$$

where k_1 and k_2 are competing rates that may control the devolatilization over different temperature ranges. The two kinetic rates weighted to yield an expression for the devolatilization [53] is

$$\frac{m_v(t)}{(1-f_{v,0})m_{p,0}-m_a} = \int_0^t (r_1 k_1 + r_2 k_2) exp\left(-\int_0^t (k_1 + k_2) dt\right) dt \quad \text{(E 2.46)}$$

- *Homogeneous reaction sub-models*

The solid fuel devolatilization and cracking gas species will react with the supplied oxidizer and with each other, such as in the water gas shift reaction. The heat generated by exothermic reactions is important for the release of volatiles and ignition of char. The general homogenous reactions taking place are as follows.

Carbon monoxide oxidation:	$CO + 0.5O_2 \rightarrow CO_2 + Heat$	(R 2.9)
Hydrogen oxidation:	$H_2 + 0.5O_2 \rightarrow H_2O + Heat$	(R 2.10)
Methane oxidation:	$CH_4 + 2O_2 \rightarrow CO_2 + 2H_2O + Heat$	(R 2.11)
Water gas shift reaction:	$H_2O + CO \rightarrow CO_2 + H_2 + Heat$	(R 2.12)

Other models such as the Laminar finite rate model, Eddy dissipation model, Eddy dissipation concept model, which could be used with homogenous reactions only (for gaseous fuel), are not included as the aim of the fluidized bed is to burn/gasify solid fuels, rather than gaseous fuels.

- *Heterogeneous reaction sub-models*

Char is the solid devolatilization residue. A heterogeneous reaction of char with the gas species is a complex process that involves the balancing rate of mass diffusion of the oxidizing chemical species to the surface of fuel particles with the surface reaction of these species with the char. The overall rate of a char particle is determined by the oxygen diffusion to the particle surface and the rate of surface reaction, which depend on the temperature and composition of the gaseous environment and the size, porosity and temperature of the particle. The commonly simplified reaction models consider the following overall reactions:

Partial combustion:	$C + 0.5O_2 \rightarrow CO + Heat$	(R 2.13)
Complete combustion:	$C + O_2 \rightarrow CO_2 + Heat$	(R 2.14)
Boudouard reaction:	$C + CO_2 \rightarrow 2CO - Heat$	(R 2.15)
Water gas reaction/ Steam gasification:	$C + H_2O \rightarrow H_2 + CO - Heat$	(R 2.16)
Hydrogen gasification/ Methanation reaction:	$C + 2H_2 \rightarrow CH_4 + Heat$	(R 2.17)

CHAPTER 3
METHODOLOGY

This study can be divided into two main parts. The first part is the experiments that consist of gasification experiments in the 100 kWth lab-scale bubbling fluidized bed reactor and hydrodynamic behavior experiments inside bed zone of an acrylic reactor. The second part is the model simulations. The details of their methodology are presented as follows:

3.1 Gasification Experiments in the 100 kWth Lab-Scale Bubbling Fluidized Bed Reactor

3.1.1 Fuel materials

Figure 3.1 The selected fuels: rubber woodchips and plastic waste.

Rubber which is produced from rubber trees is one of the most important agricultural products in Thailand. Its plantation area is about 2.72 million ha in 2000. Every year aged rubber trees are cut down equivalent to about 14.7-19.6 million tons of rubber wood to become a raw material for sawmills and wood product factories. By-products from rubber wood processing, e.g. sawdust, wood shaving, rubber wood chip, etc., are an alternative fuel for biomass conversion processes [55].

Plastic waste is also one of the materials present in significant quantities in municipal solid waste (MSW). The majority of it consists of discarded plastic bags, which are composed of polyethylene or polypropylene. The generation of plastic waste worldwide has been and is expected to increase every year. In 2010, local media have quoted Bangkok Metropolitan Administration (BMA) deputy governor Porntep Techapaibul as saying that the city's daily 10,000 tons of trash, about 1,800 tons is plastic bags. This amount was projected to increase by about 20 percent each year. Considering the vast amount of plastic waste generated and its high heat content with low moisture content, plastic bag after being separated from MSW can be considered as a high quality fuel. However, gasification of pure plastic waste has been shown to have some operational problems such as difficulties in feeding and technical limitations due to melting [56] and therefore plastic wastes are often co-processed with other fuels [56-59]. Therefore, this study used rubber woodchip and shredded plastic bag of the High Density Polyethylene type, as seen in Figure 3.1, as fuels for gasification experiments.

As received, rubber woodchips have a very high moisture content, i.e. 30-50%, and are on average 10 mm in width and less than 5 mm in thickness. During storage, the woodchip lost some of its moisture by natural drying. To eliminate the possible effect of fuel particle size as well as to provide consistency of biomass feed rate, the length of chip was reduced to the maximum of 30 mm. The moisture content of low-moisture woodchip (pre-dried) and high-moisture woodchip was controlled at 8.5% and 27%, respectively.

The plastic waste bags (High Density Polyethylene type), which was separated from MSW, was dried and shredded. The length was approximately the same as the rubber woodchips. The shredded plastic bag was then added into high-moisture rubber woodchip (i.e. 27% moisture content) at 0, 10, and 20% by weight, which is denoted as 0, 10 and 20% SPB, respectively. The fuels were mixed thoroughly before the gasification experiment.

The properties of fuels and fuel mixtures were analyzed. The proximate analysis was conducted using the Thermal Gravimetric Analyzer (TGA). The moisture content of the rubber woodchip and the shredded plastic bag were determined following ASTM D4442-07 and ASTM D6980-12, respectively. The higher heating value (HHV) was analyzed by a Bomb Calorimeter. The major elemental contents were analyzed by the Organic Elemental Analyzer (OEA: Flash EA 1112, Thermofinnigan).

3.1.2 Experimental facilities and procedure

Due to several advantages, especially fuel flexibility in terms of properties and sizes and the high heat and mass transfer [60], the bubbling fluidized bed gasifier is considered suitable for co-gasification and was chosen for the study. Experiments were carried out in the 100 kWth bubbling fluidized bed gasifier using air as a gasifying agent. The gasifier was previously developed in this laboratory and has been used for gasification studies of various fuels. A schematic view of the BFBG is shown in Figure 3.2. It has an internal diameter of 300 mm and a height of 2,500 mm with a wall of thermal insulation 150 mm thick inside the gasifier. Its lower part situates the nozzle-type air distributor, which consists of 9 closed-end nozzles. Each of them has 42 air distributing holes with 3 mm of diameter and 60 degree downward inclination as seen in Figure 3.3. This air distributor configuration was designed for purposes of a highly promote re-circulation of gas and solid in the bed zone and a bed aggregation prevention.

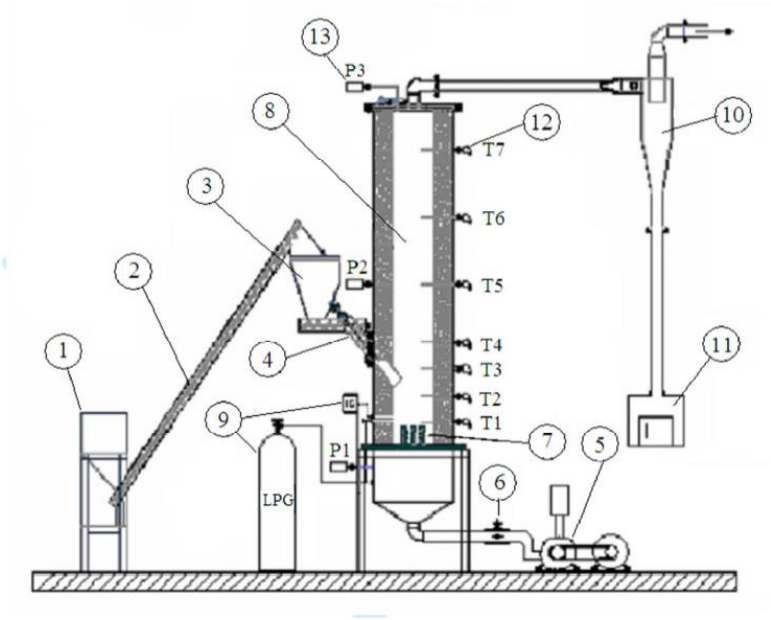

Figure 3.2 A bubbling fluidized bed gasification system: (1) ground hopper, (2) screw conveyor, (3) upper hopper, (4) injection screw, (5) force draft fan, (6) air flow meter, (7) air distributor system, (8) fluidized bed reactor, (9) preheat system, (10) fly-ash cyclone, (11) fly-ash container, (12) temperature measurement, (13) pressure measurement.

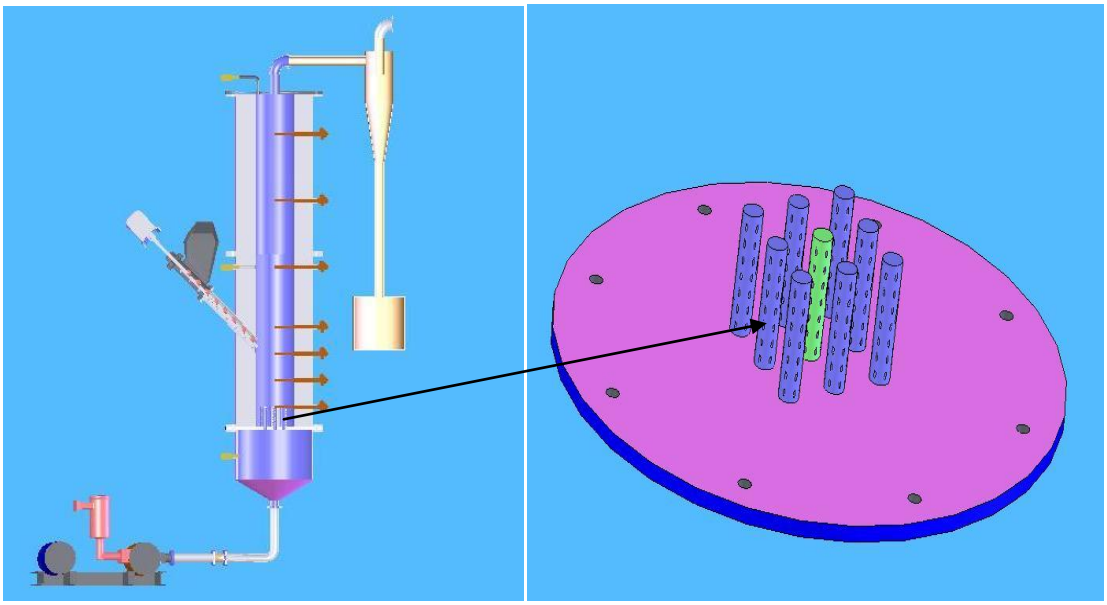

Figure 3.3 The schematic diagram of bubbling fluidized bed gasifier (left) and 3-D view of air distributor part (right).

Prior to the start of the experiment, about 30 kg of silica sand having the average particle diameter of 0.352 mm was added into the gasifier to serve as bed material with an initial height of 300 mm. The particle density and bulk density were 2647 kg/m^3 and 1560 kg/m^3, respectively. Which these size and density make silica sand is fallen into the Group B of Geldart classification. An air was fed into the system at ambient conditions with a density of 1.225 kg/m^3 and a viscosity of 1.7894 x 10^5 kg/m-s. The air flow rate is 74.3 kg/hr, which corresponds to the superficial velocity at 0.24 m/s. It was above the predetermined minimum fluidization velocity, i.e. 0.206 m/s, at ambient temperature. The gasifier system was heated up to approximately 800°C by liquefied petroleum gas (LPG) combustion. After the LPG was stopped, the fuel started to be fed into the gasifier. The flow rate of air was fixed while the fuel feed rate was varied in the range of 27-40 kg/hr, which corresponded to the equivalence ratio (ER) ranging from 0.26 to 0.48. The bulk density of feedstocks has influence on the screw feeding rate and therefore the screw feeder was calibrated before the gasification experiments. The feeder calibration and calibration curve are presented in Appendix A.

The temperatures along the height of the gasifier were measured at positions as specified in Figure 3.2 and recorded by the data logger for further analyses. To prevent the gas leakage during the experiment, the pressure in the gasifier was controlled so that it was slightly lower than the ambient pressure. The product gas was continuously sampled and

its compositions were measured by a series of gas analyzers, including Continuous Emission Monitoring (Servomex 4200 series) and Micro Gas Chromatography (Varian CP-4900). The dry gas heating value in term of higher heating value (HHV) and lower heating value (LHV) were also estimated from the obtained gas composition by Equations 3.1 and 3.2, respectively.

$$HHV = \frac{(12.77[H_2]+12.62[CO]+39.78[CH_4]+58.06[C_2H_2]+63[C_2H_4]+69.69[C_2H_6]+\dots}{100} \quad \text{(E 3.1)}$$

$$LHV = \frac{(10.79[H_2]+12.62[CO]+35.81[CH_4]+56.08[C_2H_2]+59.04[C_2H_4]+63.75[C_2H_6]+\dots}{100} \quad \text{(E 3.2)}$$

where the species contents are given in volume %, and their heat of combustion in MJ/Nm^3 [61].

The main objective of this part is to examine the technical feasibility of the operation of plastic waste gasification, with the purpose of developing an environmentally acceptable process to decrease the amount in the waste stream through energy recovery. The proportion of plastic waste to biomass was studied to solve the moisture problem for biomass gasification. The experiments will be performed in 100 kWth lab-scale of a bubbling fluidized bed gasifier as seen above. The effect of air to fuel ratio (presented in term of equivalence ratio - ER) and plastic waste addition ratio on gasification performance and quality of gas product were investigated and compared with those obtained from the pre-dried woodchip.

3.2 Hydrodynamic Behavior Experiments inside Bed Zone of an Acrylic Reactor

Due to the insulation inside the gasifier as presented above, it is impossible to observe the behavior inside. Therefore, to validate the CFD simulation results, an acrylic reactor was constructed and performed. It was designed to have the same ratio of diameter to height as that of the BFBG used in this study, i.e. about 1:8, as shown in Figure 3.4.

A series of manometers were installed to monitor the absolute pressure along the height of the model, with more frequent positions around the bed zone (every 50 mm from the air distributor level). The silica sand with the same properties as mentioned above was patched for 150 mm of height inside the acrylic reactor. An air distributor was designed to

be a plate with 9 holes, which was supported by wire mesh, as it is simple fabrication and represents the simplified version of 9 closed-end nozzles air distributor at lower part of the real BFBG. An air flow from the ring blower was controlled by bypass valve and was measured by an air flow meter as presented in Figure 3.5.

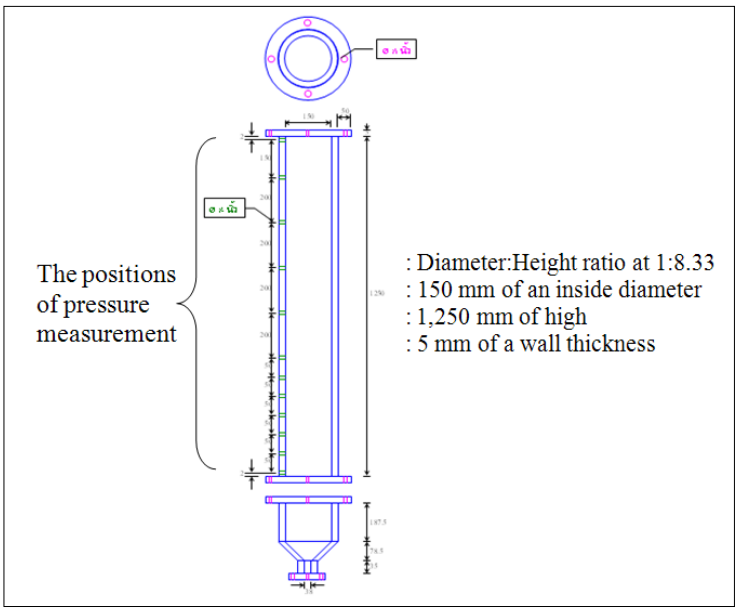

Figure 3.4 An acrylic reactor.

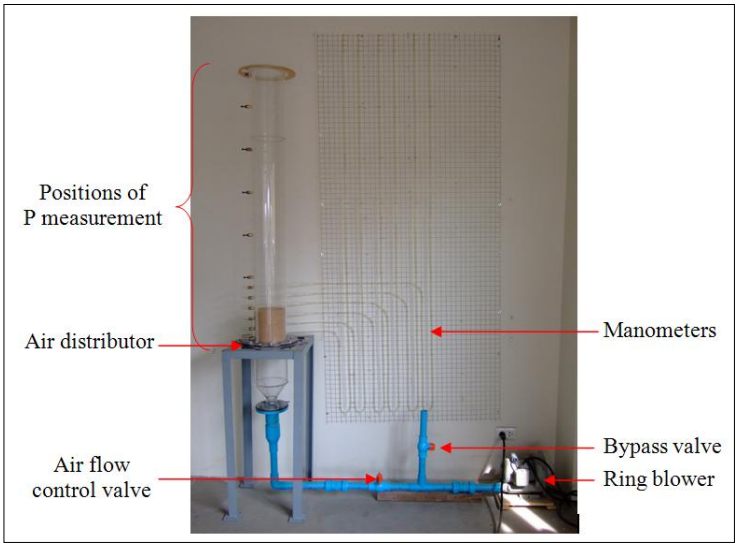

Figure 3.5 A complete set of an acrylic reactor.

The pressure drop across the bed at minimum fluidization velocity, the bubble appearance inside the bed zone, and the bed expansion ratio were investigated by using this acrylic reactor. The pressure drop across the bed at minimum fluidization velocity was

obtained from the graph plot between air velocities versus pressure drop across the bed. The bubble appearance inside bed zone was obtained from the video recording. The bed expansion ratio was calculated by dividing the quasi-steady state bed height by initial bed height (H_i/H_0) [62].

3.3 Model Simulations

The enormous growth in computing power, coupled with the advent of meaningful mathematical models, has been very useful in fluidization study. Simulations are becoming faster and models more accurate, allowing for detailed predictive simulations. Therefore, the hydrodynamic behavior of bubbling fluidized bed gasifier was studied in case of three-dimensional simulation, both under cold flow condition and elevated temperature condition, in this research by using a commercially available CFD code called FLUENT.

Computational fluid dynamics simulations of fluidized beds present substantial challenges including computational, modeling, and numerical challenges. In a Lagrangian approach, tracking individual particles through independent but simultaneous force balances has been done [16, 63], but the computational demands for large fluidized beds with several million particles is substantial, and in many cases, prohibitive. Therefore, an Eulerian approach which describes a fluidized bed as consisting of two interpenetrating fluids is used in this study. The kinetic theory of granular flow (KTGF) is also introduced into the Eulerian approach to improve the description of particle collision.

For the model simulation study, assumptions were set as follows:

- the multiphase flows in fluidized bed gasifier were two phases of gas and solid
- the nozzles of air distributor were designated as “Velocity Inlets”
- no solids were introduced through the “Velocity Inlets” boundary
- the top of the bed was set as a constant pressure outlet
- the walls were all set as no-slip walls

This part of the research has been separated into two sections as follows.

3.3.1 CFD model validations: Under cold flow (ambient temperature and non-reactive consideration) conditions

For the CFD model validation, all the input parameters and optional model selections were studied and set in the simulation model, named the "acrylic model", then the results obtained from this acrylic model simulation were validated by comparison with

the experimental results obtained from the acrylic reactor performance. The acrylic model was set up following the dimension of acrylic reactor as presented above in Figure 3.4. The grids as seen in Figure 3.6 were created and meshed in a CAD program called GAMBIT which now more comfortable use in a function called ANSYS Workbench, including of DesignModeler and Meshing. The yellow color represent to the meshed line while the green color on the bottom phase represent to the holes on a plate. Then the meshed model was exported into FLUENT for simulation.

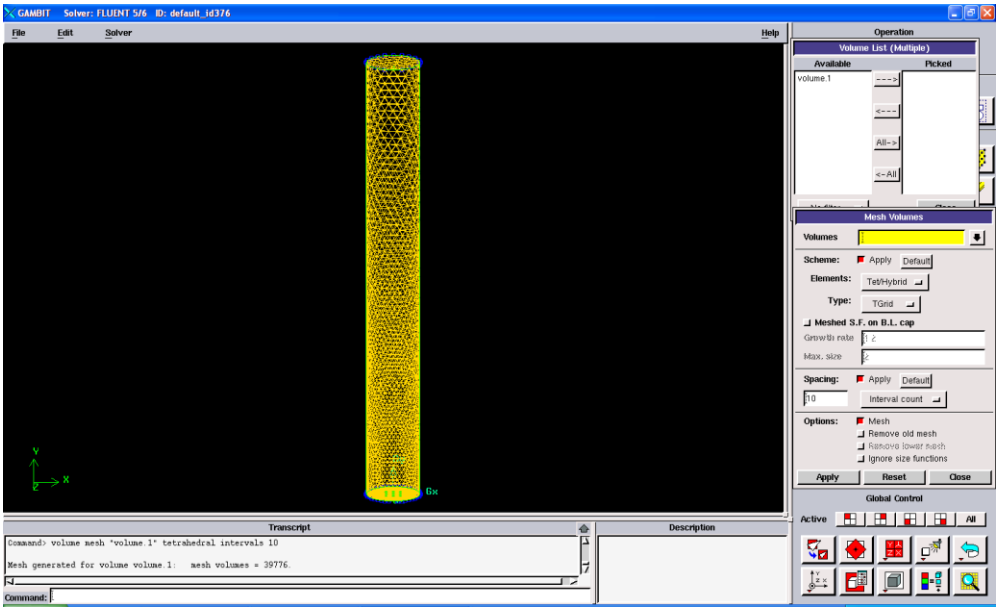

Figure 3.6 The created model represent to acrylic reactor.

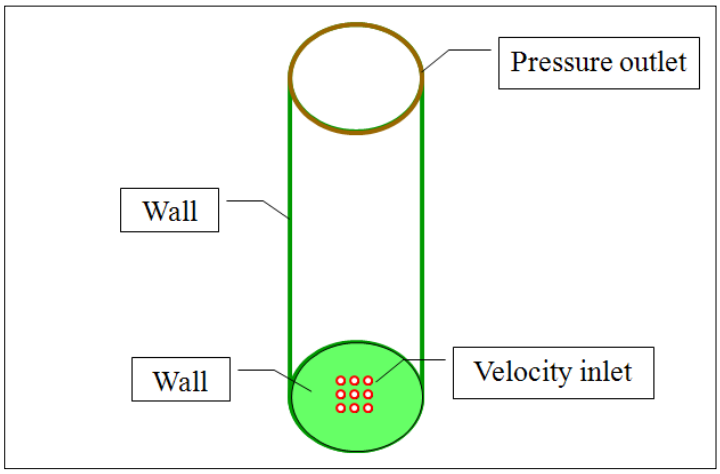

Figure 3.7 Boundary setting.

Boundaries of the acrylic model were set as presented in Figure 3.7. For the solid phase, it was set with the same properties of silica sand that had been used as a bed material in the acrylic reactor. It was also patched into the acrylic model with the same height as that of the silica sand in the acrylic reactor. For gas phase, it was set with the same properties of air that had been used as a gasification medium in acrylic reactor. The minimum fluidization velocity of 0.206 m/s obtained from Equation 3.3 was set on the velocity inlet boundary.

$$U_{mf} = 0.00114 \frac{g d_p^2 (\rho_p - \rho_g)}{\mu_g} \quad \text{(E 3.3)}$$

where d_p is a diameter of particle in solid phase (m), ρ_p is a density of particle in solid phase (kg/m^3), ρ_g is a density of gas in gas phase (kg/m^3), and μ_g is a gas viscosity (kg/m-s).

The parameters of input conditions, such as a specularity coefficient of the momentum-shear condition, a restitution coefficient of the multiphase-granular property, and the optional model selections to represent the term of an interphase exchange coefficient, were studied and tested. Then the simulation results in terms of the pressure drop across the bed at a minimum fluidization velocity, the solid volume fraction which represents to the bubble appearance inside bed zone, and the bed expansion ratio were compared with the experimental results obtained from acrylic reactor performance for a confirmation of CFD model validations.

3.3.2 Simulation investigations: Under cold flow (ambient temperature and non-reactive consideration) conditions and elevated temperature (hot sand with heat transfer and non-reactive consideration) conditions

In this simulation setup part, there are two created models. The first one represents a non-simplified air distributor model that was set up following the dimensions of the BFBG with a complete set of air distributor. While a simplified one had the same dimension, but the air distributor part was simplified to be a plate with 9 holes. Figure 3.7 zoomed in the symmetrical 3-D section of non-simplified and simplified model to clearly see their difference from the air distributor part.

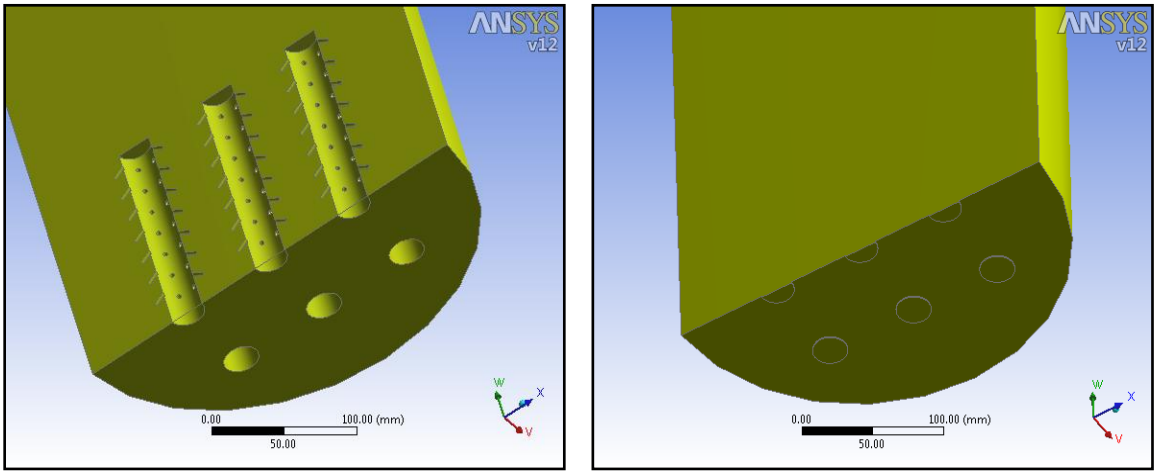

a. Non-simplified air distributor model b. Simplified air distributor model

Figure 3.8 The symmetrical 3-D section of non-simplified and simplified air distributor model.

To simulate both of these created models in FLUENT, the boundaries were set following Figure 3.6. The input parameters and the optional model selections, which had been studied and validated as described in the section above, were set in the Solution Setup step. The silica sand, which was used as a bed material in the BFBG experiment part, was set as a solid phase in the model simulation. It was patched to have an initial height at 300 mm. The ambient air, which was used as a gasification medium in the BFBG experiment part, was set as a gas phase in the model simulation. An air inlet velocity was set at 3.8137 m/s following the air velocity, which corresponded to the air flow rate, of the gasification experiment part.

The main purpose of this part is to investigate the hydrodynamic behavior inside the bed zone of a non-simplified and simplified air distributor in a bubbling fluidized bed gasifier model. The model simulation, under cold flow condition, results obtained from these two models in terms of solid volume fraction (which represents to the formation and motion of bubbles inside bed zone, gas-solid flow pattern, and bed expansion ratio) and pressure drop across the bed were compared.

Furthermore, the effect of mesh element number and the presence of a feeding pipe existence on the model simulation were also investigated.

For the mesh element number effect investigation, the non-simplified and simplified models were meshed several times in the Meshing step to vary the mesh element

number. All of them were simulated in FLUENT simulation step to be able to find out the optimum one for simulation.

For the feeding pipe existence effect investigation, the simplified model was created two times in the Design Modeler step to be the one with the feeding pipe and the other one without it. Both of them were simulated in FLUENT simulation step to be able to see if there are any effects on the simulation result.

After finishing the simulations on both non-simplified and simplified model under cold flow condition, the models were investigated again under elevated temperature conditions. The solid phase, which was patched to has an initial height of the bed material at 300 mm, was re-patched again with temperature of 800°C follow as the gasifier system in experiment part which was heated up to approximately 800°C before the biomass was fed into the gasifier. The model of "Energy" in Solution Setup step was turned on to allow the heat from solid phase transfers to gas phase. Then the effect of this hot sand with heat transfer on the model simulation was studied

In addition, the usage times for all model simulations were also compared and discussed.

CHAPTER 4
RESULTS AND DISCUSSION

4.1 Gasification Experiments in the 100 kWth Lab-Scale Bubbling Fluidized Bed Reactor

The photograph of shredded plastic bag (SPB) and high-moisture rubber woodchip after the preparation is presented in Figure 4.1, while Figure 4.2 shows examples of the prepared fuel mixture at different proportions of SPB.

Figure 4.1 The prepared shredded plastic bag and high-moisture rubber woodchips.

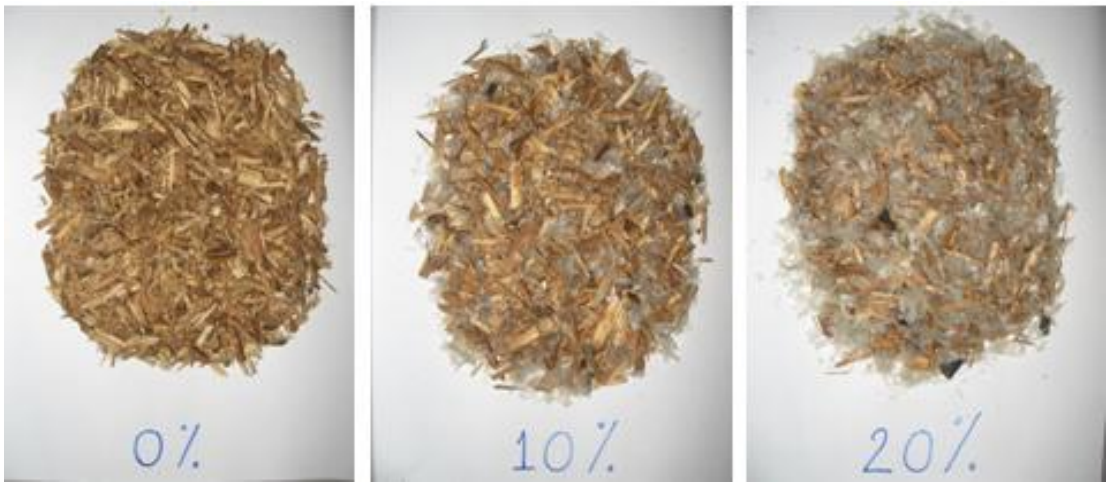

Figure 4.2 The fuel mixtures at various proportions of SPB.

After the fuels were prepared, the gasification experiments were processed in the 100 kWth lab-scale bubbling fluidized bed reactor. The experimental results are presented as follows:

4.1.1 Improvement of fuel mixture properties

The properties of rubber woodchips and SPB are presented in Table 4.1. SPB has much higher carbon and hydrogen content, i.e. 83.6 and 14.9 wt%, as compared to 46.1 and 6.0 wt% for rubber woodchips on a dry-ash-free basis. This higher hydrocarbon content of SPB also leads to a significant increase in HHV by 32.2 MJ/kg as compared to that of rubber woodchip.

Table 4.1 Properties of used fuels

	Rubber woodchips	SPB
Proximate analysis (wt%, dry basis)		
Volatile matter	88.9	99.6
Fixed carbon	10.0	0.0
Ash	1.1	0.4
Higher heating value (MJ/kg)	13.0	45.2
Ultimate analysis (wt%, dry-ash-free basis)		
Carbon	46.1	83.6
Hydrogen	6.0	14.9
Nitrogen	0.7	0.0
Oxygen	47.2	1.5
Sulfur	0.0	0.0

Table 4.2 Analysis of the fuel mixture at various proportions

Mixture	0% SPB	10% SPB	20% SPB	100% SPB
Elemental composition (wt%, wet basis)				
Carbon	33.5	38.5	43.5	83.2
Hydrogen	4.3	5.4	6.5	14.9
Nitrogen	0.5	0.4	0.4	0.0
Oxygen	34.3	31.0	27.7	1.5
Sulfur	0.0	0.0	0.0	0.0
Ash	0.3	0.3	0.3	0.4
Moisture	27.0	24.3	21.6	0.0
Higher heating value (MJ/kg)	13.0	16.2	19.4	45.2

As mentioned earlier, the moisture content of high-moisture rubber woodchips was controlled at 27%. Taking that into account, the properties of fuel mixtures of high-moisture rubber woodchips with different addition ratios of SPB were calculated, and are presented in Table 4.2. The increased proportion of SPB in the fuel mixture from 0% to

10% and 20% helped decrease the average moisture content in the mixture from 27% to 24.3% and 21.6%, respectively. Furthermore, the higher heating value (HHV) in the fuel mixture also increased from 13.0 to 16.2 and 19.4 MJ/kg, respectively, due to the relatively high hydrocarbon contents of SPB.

4.1.2 Improvement of average bed temperature

The average bed temperature resulted from the high-moisture rubber woodchip gasification significantly dropped from that of the low-moisture rubber woodchip (i.e. the case of 0% SPB, 8.5% M.C.) throughout the range of studied ERs as presented in Figure 4.3. About 50-60°C temperature decrease could be observed when the moisture content of the fuel increased from 8.5% to 27% due to the higher amount of energy demand for a moisture evaporation, which would otherwise be used by the endothermic pyrolysis and char gasification reactions [64]. This is one of the main effects caused from gasifying high-moisture biomass, which is in line with the results from the other study [65].

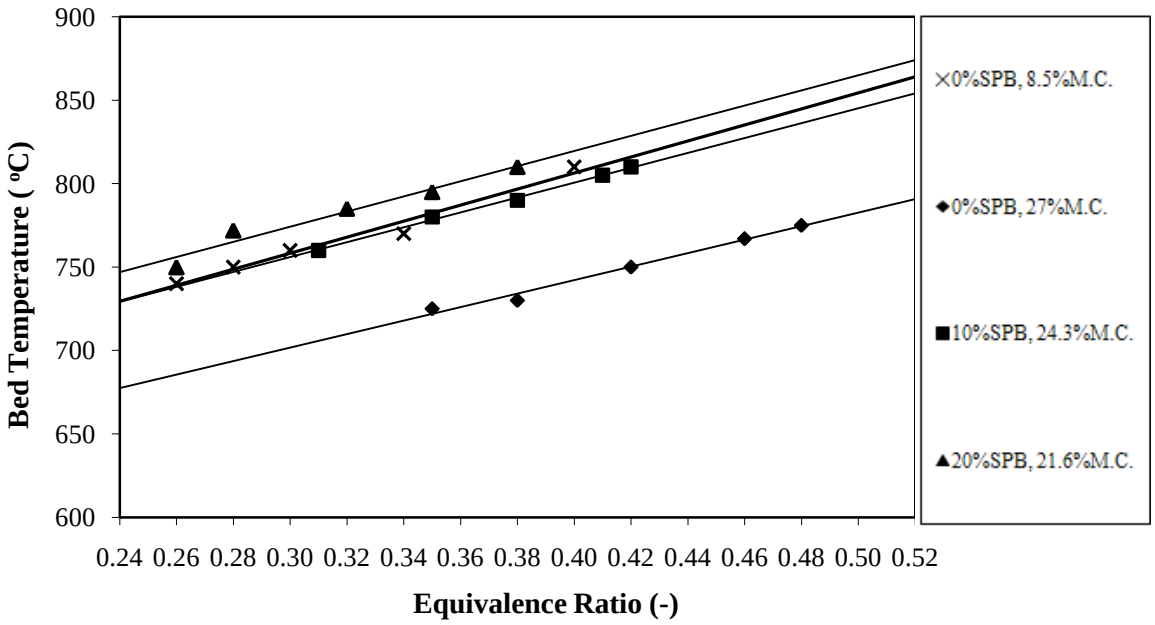

Figure 4.3 Average bed temperature at various ERs and the proportions of SPB in the fuel mixture as compared to that of low-moisture rubber woodchips.

An improvement in bed temperature was found when adding SPB into the fuel mixture. The average bed temperature was increased by about 60 and 80°C when the SPB proportion was increased from 0 to 10 and 20%, respectively. This is mainly attributed to the decreased moisture content and increases heating value of the fuel mixture with

increasing the weight proportion of SPB in the fuel mixture, as presented in Table 4.2. The higher the proportion of SPB added, the higher the average bed temperatures for all ERs. It was found that the average bed temperature when gasifying the fuel mixture with 20% SPB was higher than that of the low-moisture rubber woodchip gasification. Figure 4.3 also shows that the average bed temperature increased with increasing ER for all proportions of SPB in the fuel mixture. The increase of ER would increase the rate of the exothermic reaction (promoting the oxidation reaction) resulting in more heat released and the rise of temperature in the gasifier [15, 66].

4.1.3 Improvement of synthesis gas quality

All the reactions determining the final gas composition for biomass gasification are generally agreed to happen through three steps. The first step, called devolatilization or pyrolysis, and also called partial gasification, is initiated at low temperature when the thermally unstable components are broken down and evaporated with other volatile components, resulting in char, tar, and light gases, such as H_2, CO, CO_2, CH_4, H_2O, as presented in Reaction 4.1.

Pyrolysis reaction: Biomass + Heat → Char + Gases + Vapor or Liquid (Tar) (R 4.1)

Then the second step, called oxidation or combustion, starts to take place to provide practically all the thermal energy demanded for endothermic reactions. Oxygen supplied to the gasifier reacts with the combustible substance resulting in the formation of CO_2 and CO, as seen in Reactions 4.2 to 4.3. Consequently, the reduction of char is produced in the first step. The oxidation of hydrogen in fuel to produce steam is also presented by Reaction 4.4. Reactions 4.5 and 4.6 are the carbon monoxide oxidation and methane oxidation, respectively.

Oxidation reactions:

$$C + O_2 \rightarrow CO_2 + \text{Heat} \quad \text{(R 4.2)}$$

$$C + \tfrac{1}{2} O_2 \rightarrow CO + \text{Heat} \quad \text{(R 4.3)}$$

$$H_2 + \tfrac{1}{2} O_2 \rightarrow H_2O\ (\text{Steam}) + \text{Heat} \quad \text{(R 4.4)}$$

$$CO + \tfrac{1}{2} O_2 \rightarrow CO_2 + \text{Heat} \quad \text{(R 4.5)}$$

$$CH_4 + 2O_2 \rightarrow CO_2 + 2H_2O + \text{Heat} \quad \text{(R 4.6)}$$

And in the last step, the gasification reactions of the remaining carbonaceous residue happen with steam and carbon dioxide, as shown in Reactions 4.7 to 4.9. Methane could also form in the gasifier through the reaction, as seen in Reaction 4.10.

Water gas reaction:	$C + H_2O \rightarrow CO + H_2 - Heat$	(R 4.7)
Boudouard reaction:	$C + CO_2 \rightarrow 2CO - Heat$	(R 4.8)
Water gas shift reaction:	$H_2O + CO \Leftrightarrow CO_2 + H_2 + Heat$	(R 4.9)
Methanation reaction:	$C + 2H_2 \rightarrow CH_4 + Heat$	(R 4.10)

Considering all the processes mentioned above, the product gas composition after the fuel mixtures were gasified is investigated in this part. Figure 4.4 shows that CO_2 generation was diminished, while the release of CO and H_2 increased with increasing the weight proportion of SPB in the fuel mixture at all ERs. This is probably due to the increase of reactor temperature with increasing the SPB in the fuel mixture as presented in Figure 4.3. The average bed temperature of high-moisture rubber woodchip gasification (i.e. 0% SPB, 27%M.C.) was around 700-750°C at ER in the range of 0.35-0.48. Within this range of temperature, the water gas shift reaction (R 4.9) was probably one of the most important reactions defining the final gas composition. While the average bed temperature of 10% and 20%SPB in the fuel mixture increased to 750-800°C at ER in the range of 0.26-0.43, the forward reaction of the Boudouard reaction (R 4.8) and water gas reaction (R 4.7) were favored resulting in the reduction of CO_2 formation and increasing of CO and H_2 production [56, 67]. The production of CH_4 and C_2H_n also increased as the weight proportion of SPB increased in the fuel mixture for all ERs due to the plastic cracking, rather than the methanation reaction [68]. Adding SPB in the fuel mixture resulted in the higher content of hydrogen and carbon, as seen in Table 4.2, which means that the reactants are increased, so this might also be part of the reason why the release of H_2, CO, CH_4, and C_2H_n has increased.

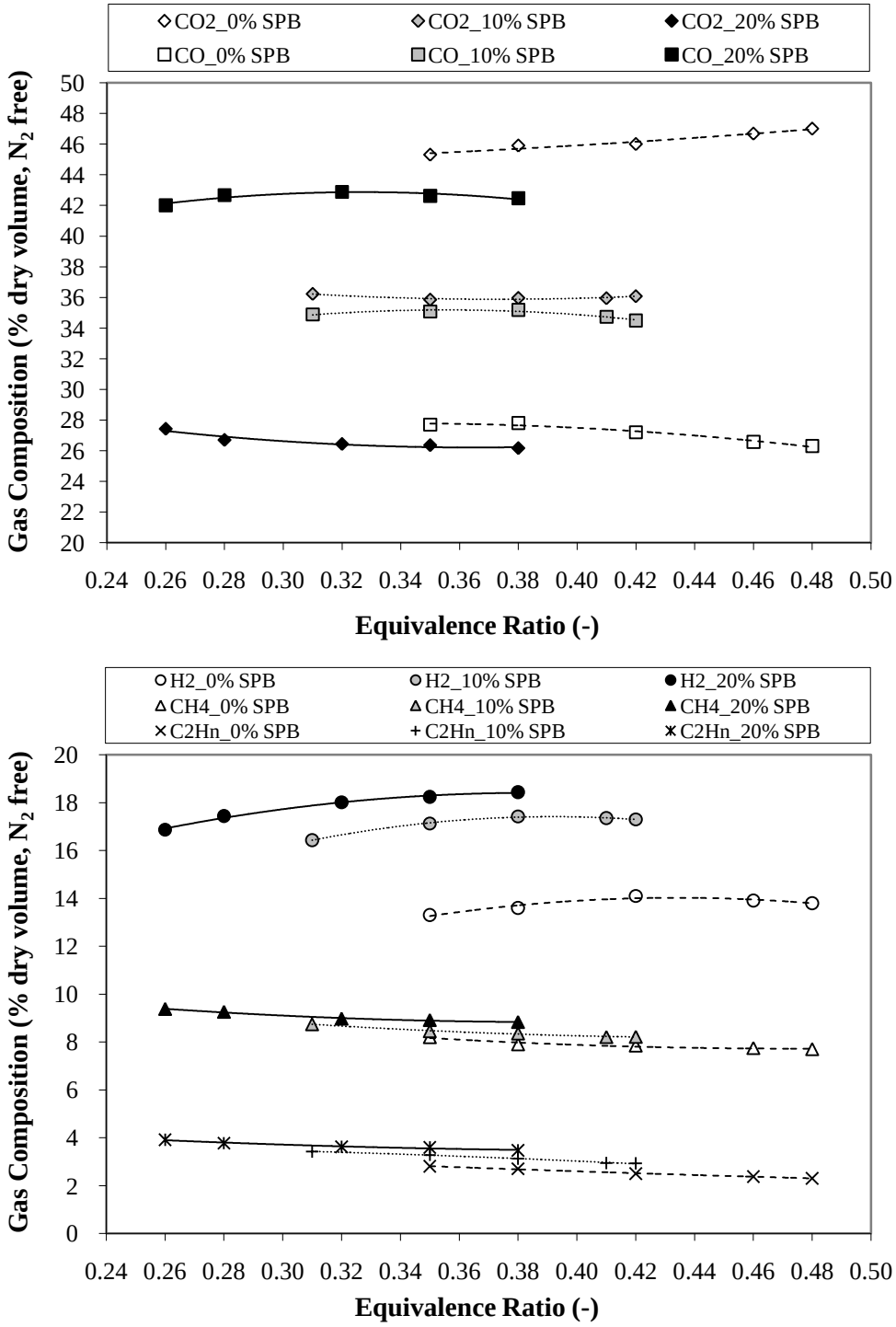

Figure 4.4 Product gas compositions at various ERs and the proportions of SPB in the fuel mixture.

The correlation between the product gas composition and the equivalence ratio (ER) is also presented in Figure 4.4. The results showed that the ER had significantly affected the gas composition. For the case of high-moisture rubber woodchip gasification

(i.e. 0% SPB, 27%M.C.), the productions of CO, CH_4, and C_2H_n slightly decreased while the productions of CO_2 and H_2 slightly increased as ER was increased from 0.35 to 0.48. This is probably due to the reactor temperature increased with increasing ER that favors the forward reaction of the water gas shift reaction (R 4.9). For the case of adding 10% and 20%SPB in the fuel mixture, the productions of CO and H_2 slightly increased as ER was increased until ER reached 0.35 after that the productions of those gases started to slightly decreased while the productions of CO_2, CH_4, and C_2H_n slightly decreased with increasing ER. This is probably due to the forward reaction of the Boudouard Reaction (R 4.8) and the water gas reaction (R 4.7) were favored as ER was in the range of 0.26-0.43.

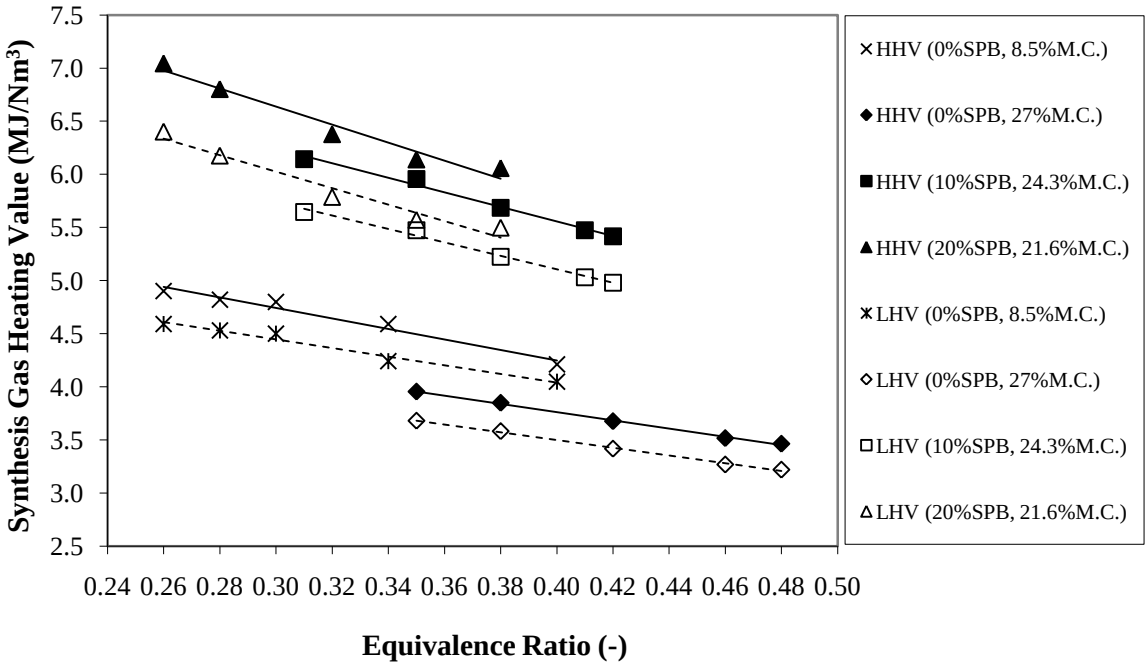

Figure 4.5 Synthesis gas heating value at various ERs and the proportion of SPB in the fuel mixture as compared to that of low-moisture rubber woodchips.

The effect of the moisture content and the SPB proportion in the fuel mixture on the synthesis gas heating value, in terms of higher heating value (HHV) and lower heating value (LHV), is shown in Figure 4.5. The high-moisture rubber woodchips (i.e. 0% SPB, 27% M.C.) produced synthesis gas having HHV and LHV lower than those of the low-moisture rubber woodchips (i.e. 8.5% M.C.) by about 0.5 MJ/Nm^3 for all ERs. By adding SPB in the fuel mixture even at 10% by weight, both HHV and LHV were increased by more than 50% that is from 3.5-4.0 MJ/m^3 to 5.3-6.3 MJ/m^3. This is likely caused by the

relatively high hydrocarbon contents of SPB in the fuel mixture (referred to Table 4.2). However, the further increase in % SPB only slightly improved the heating value of the product gas. Considering all mixture cases, the increase in ER reduced the synthesis gas heating value due to the more available O_2 favoring oxidation reaction as well as the effect of N_2 dilution. This is in line with the observation of the other studies [66, 67].

4.1.4 Improvement of carbon conversion efficiency

Carbon conversion efficiency, or the ability to convert carbon in the solid phase into the gas phase, was also investigated in this study. It is calculated as the ratio between the amount of carbon in the product gases (i.e. CO, CO_2, CH_4 and C_2H_n) and the amount of carbon in the fuel feeding [37]. The carbon conversion efficiency at various ER and proportions of SPB in the fuel mixture compared with that of low-moisture rubber woodchip is displayed in Figure 4.6. As expected, the carbon conversion efficiency for all ERs significantly dropped when the moisture content of the rubber woodchip was increased from 8.5 to 27%. With 20% mixing of SPB in the high-moisture rubber woodchip (i.e. 27% M.C.) the carbon conversion efficiency could be improved to reach the level of the pre-dried woodchip. Moreover, increasing ER could effectively increase the carbon conversion efficiency at all feedstock conditions. However, the higher availability of air at high ER gives a negative effect on the heating value of product gas, as discussed in the previous section.

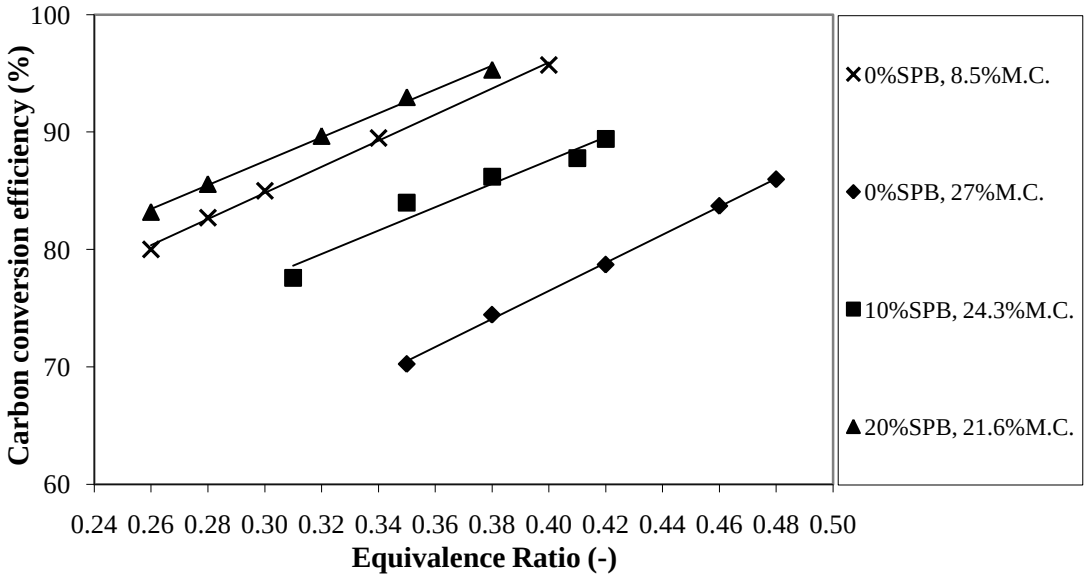

Figure 4.6 Carbon conversion efficiency at various ERs and the proportions of SPB in the fuel mixture as compared to that of low-moisture rubber woodchips.

4.2 CFD Model Validations: Under Cold Flow Conditions

The acrylic model, which was created based on the configuration of the acrylic reactor, was exported from the ANSYS Workbench to FLUENT for simulation under cold flow conditions. The input parameters and the optional model selections were varied to find the appropriate ones, as presented in Appendix B. At the beginning of using FLUENT, the use of some program default parameters resulted in strange simulation results. The simulated solid volume fraction, as shown in Figure 4.7, was an example that showed that all sand from the bed zone had flown out of the model although the air velocity used was low.

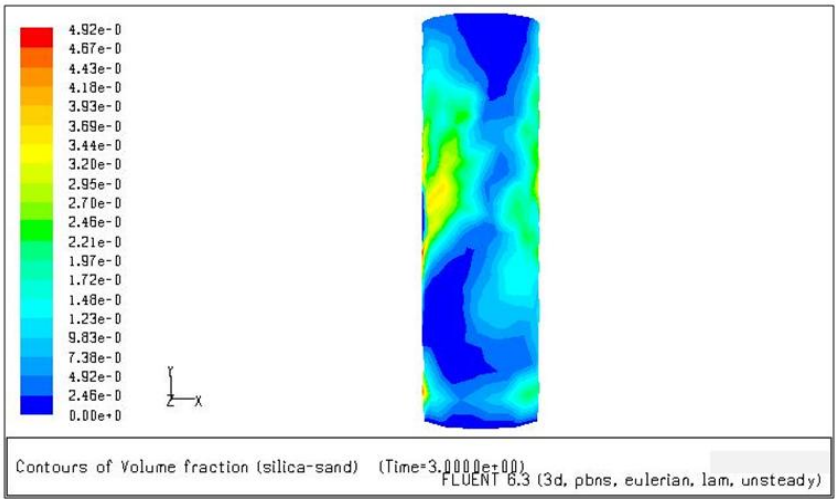

Figure 4.7 The solid volume fraction of the failure simulation result

This failure was checked and it was found that the momentum-shear and the multiphase-granular conditions of the solid phase, which had been set in a wall boundary, should have been adjusted following the nature of its behavior, according to the previous studies [69, 70]. As the particle of sand was pushed by the air force, it collided with other particles around it. Taking into account this so-called inelastic collision, the optimized value of restitution coefficient in this model was found at 0.9. During the collision, some part of energy was lost and there were a high solid concentration near the wall which prefers a small value of specularity coefficient as found from literatures [71, 72]. Here, the optimized value of specularity coefficient was found at 0.01.

To improve the simulation results, an interphase exchange coefficient was also studied. From FLUENT 6.3 [73], the fluid-solid exchange coefficients β_{gs} for granular flows can be written in the following general form:

$$\beta_{gs} = \frac{\alpha_s \rho_s f}{\tau_s} \tag{E 4.1}$$

where f is the drag function, which is defined differently for the different exchange coefficient models (as described below), and τ_s is the particulate relaxation time, which is defined as:

$$\tau_s = \frac{\rho_s d_s^2}{18\mu_g} \tag{E 4.2}$$

where d_s is the diameter of the particles of phase *s*.

There are three models of fluid-solid exchange coefficients. The first one is the Syamlal-O'Brien model, which is based on measurements of the terminal velocities of particles in fluidized or setting beds. This model is appropriate when the solids shear stress is defined according to Syamlal et al. [74]. The second one is the model of Wen and Yu which is appropriate for dilute systems. And the last one is the Gidaspow model which is a combination of the Ergun equation and the Wen and Yu model. It is recommended for dense fluidized beds. Therefore, this Gidaspow model was used to represent the terms of interphase exchange coefficient in this study as the bed zone of BFBG is a dense one.

For CFD model validation, the acrylic model simulation results in terms of the pressure drop across the bed at minimum fluidization velocity, the solid volume fraction which represents to the bubble appearance inside bed zone, and the bed expansion ratio were compared with the experimental results obtained from acrylic reactor.

4.2.1 The pressure drop across the bed at minimum fluidization velocity

For the acrylic model simulation, the pressure drop across the bed at a given minimum fluidization velocity was obtained by the difference between the absolute pressure at the height over the bed zone (around 200 mm from the air distributor level) and that at the air distributor level. The given minimum fluidization velocity was 0.206 m/s,

which was obtained from calculation (Equation (3.3)). From Figure 4.8, the absolute pressure at the height of 0 and 200 mm from the air distributor level of acrylic model were 103449 and 101325 Pa, respectively. Therefore, the pressure drop across the bed in this acrylic model simulation was 2124 Pa or 21.66 cm water gauge (cm w.g.).

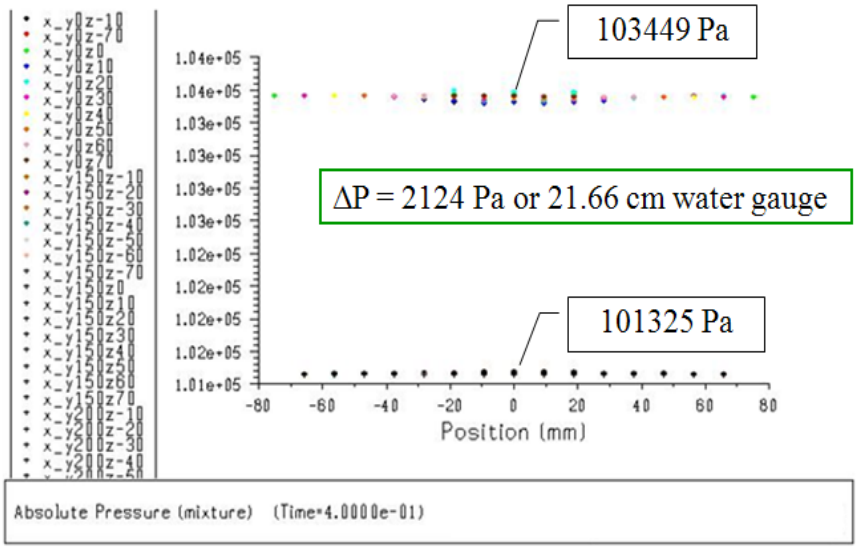

Figure 4.8 Absolute pressure at the height of 0 and 200 mm from air distributor level that resulted from the acrylic model simulation.

In the theoretical study, it was found that at the minimum fluidization velocity, all the particles were essentially supported by the air stream. The pressure drop through the bed is then equal to the bed weight divided by the cross-sectional area of the bed, $\Delta P = W/A$. In this case, the sand was patched at 150 mm high inside the acrylic model which caused to the weight of sand around 4 kilograms. The theoretical pressure drop calculated from this equation was around 2220.53 Pa or 22.64 cm w.g.. Yang [75] found that in actual practice, the pressure drop at minimum fluidization velocity is actually less than W/A because a small percentage of the bed particles is supported by the wall owing to the less than perfect design of the air distributor, to the finite dimension of the containing vessel, and to the possibility of channeling. Therefore, the pressure drop resulted from this acrylic model simulation was represented to the pressure drop across the bed at minimum fluidization velocity as it was a little bit less than W/A.

From the experiment in the acrylic reactor, the pressure drop across the bed at minimum fluidization velocity was obtained from the graph plot between air velocities versus pressure drops across the bed. After slightly increased the air velocity, by

controlling the bypass valve of acrylic reactor, from 0 to 0.5 m/s, pressure drop across the bed changed as seen in Figure 4.9. The pressure drop across the bed increased following the increase of air velocity until it reached the minimum fluidization velocity at around 0.218 m/s, where the highest pressure drop across the bed was found to be 21 cm w.g.. Continuing to increase the air velocity, the pressure drop across the bed was maintained at 20.5 cm w.g.. Referring to the pressure drop across the bed at 21.66 cm w.g obtained from the acrylic model simulation, the experimental and simulation values agree well. Furthermore, these values are also close to those obtained from calculation.

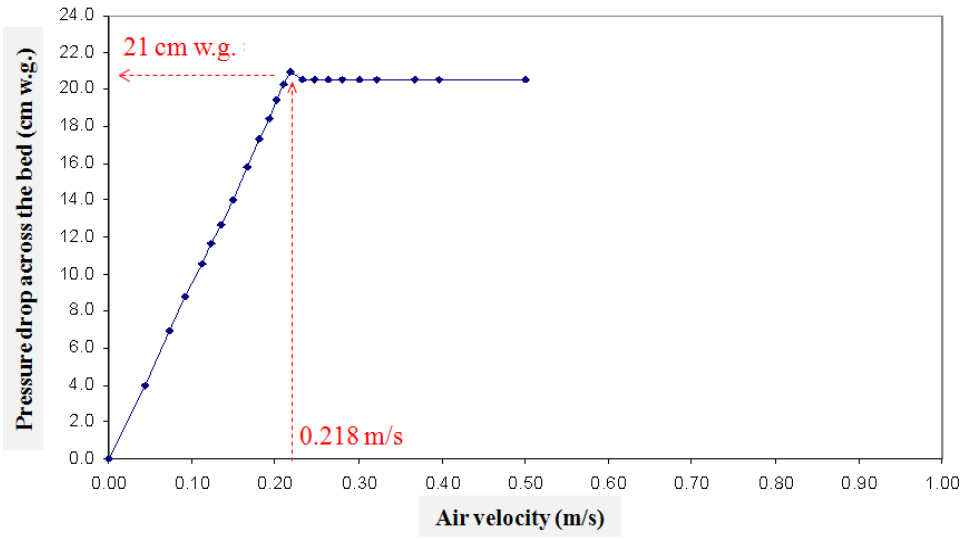

Figure 4.9 Pressure drops across the bed V.S. air velocity resulting from acrylic reactor experiment.

4.2.2 The bubble appearance inside the bed zone

The visual observation of particle behavior during the cold flow experiment in the acrylic reactor was continuously recorded. The captured pictures of the solid bed movement were compared with the contour of solid volume fraction resulted from the acrylic model simulation as a function of time, as presented in Figure 4.10. The movement of contour of solid volume fraction in the acrylic model simulation and of air bubbles in the acrylic reactor coincided well during the simulation time of 0 to 0.6 s.

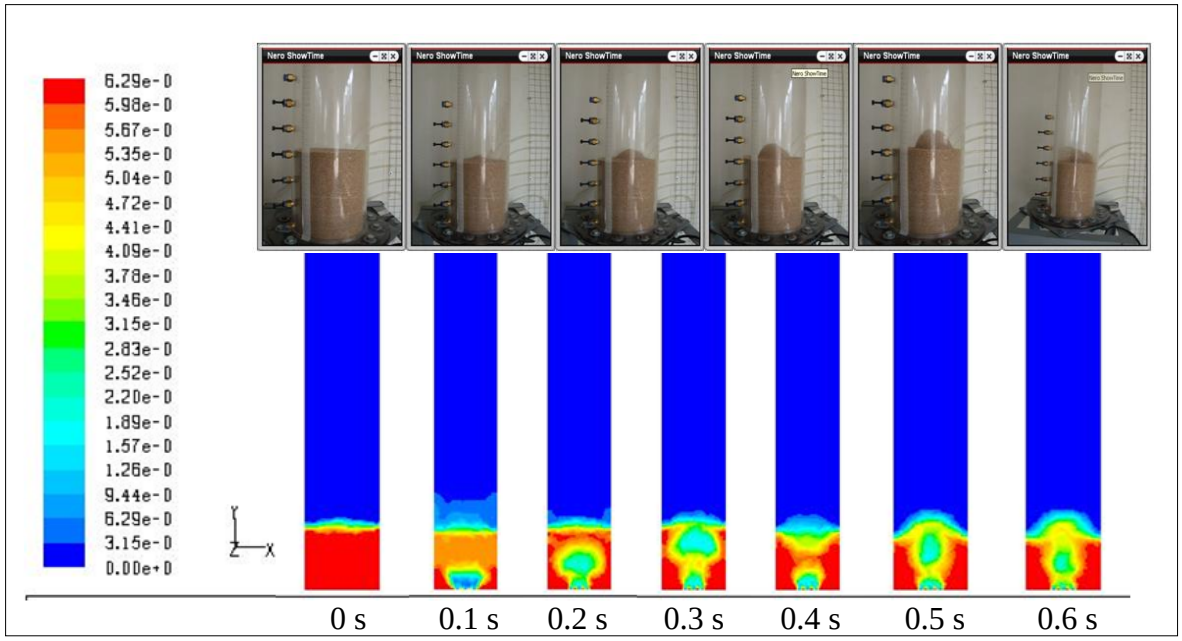

Figure 4.10 Comparison inside the bed zone of the bubble appearances resulting from experiment and simulation at U_{mf}.

4.2.3 The bed expansion ratio

The bed expansion ratio was calculated by dividing the quasi-steady state bed height with the initial bed height (H_i/H_0). The quasi-steady state bed height obtained from simulation was about 170 mm, while it was fluctuating in the range of 170 - 180 mm in acrylic reactor. Based on the same initial bed height of 150 mm, the bed expansion ratios were similar. This result also shows a similar range to that reported in the previous literature [62], that the bed expansion ratio was around 1.2 at gas velocity of 0.2 m/s.

Therefore, the input parameters and the CFD model that had been set in FLUENT and simulated under cold flow conditions on the acrylic model were acceptable as confirmed by the results for the validations above. These were applied in the next part of the model simulation of the BFBG. The input parameters of the BFBG were summarized as presented in Table 4.3.

Table 4.3 The input parameters for model simulation.

Problem Setup	**Input Parameter**
Solver	
Type	Pressure-Based
Velocity Formulation	Absolute
Time	Transient
Model	
Eulerian	2 Phases
Materials	
Air Density (ρ_g)	1.225 kg/m^3
Air Viscosity (μ_g)	1.7893 e-05 kg/m-s
Silica Sand Density (ρ_s)	2647 kg/m^3
Diameter of Silica Sand (d_s)	0.352 mm
Phases	
Primary Phase	Air
Secondary Phase	Silica Sand
Phase Interaction	
- Drag Coefficient	Gidaspow
- Collisions	0.9 (Constant)
Boundary Conditions	
For “Wall” set “Silica Sand”	
- Restitution Coefficient between Silica Sand and Wall (e_w)	0.9
- Specularity Coefficient ($ø$)	0.01
For “Velocity Inlet” set “Air”	
- Air Inlet Velocity (v_g)	3.8137 m/s
Patch	
Phase	Silica Sand
Initial Bed Height (H_0)	300 mm
Initial Solid Volume Fraction (ε_s)	0.538
Solid Inlet Volume Fraction at Maximum Packing Limit ($\varepsilon_{s,max}$)	0.63
Run Calculation	
Time Step Size	0.0001 s
Iterations per Time Step	50

4.3 Simulation Investigations: Under Cold Flow Conditions – Mesh Element Number Effect

To reduce the computational time, the number of the mesh element is minimized while not affecting the accuracy of the simulation process. Therefore, the non-simplified air distributor model was meshed, in ANSYS Meshing, with different mesh resolution to check the effect of mesh element number on the simulation process.

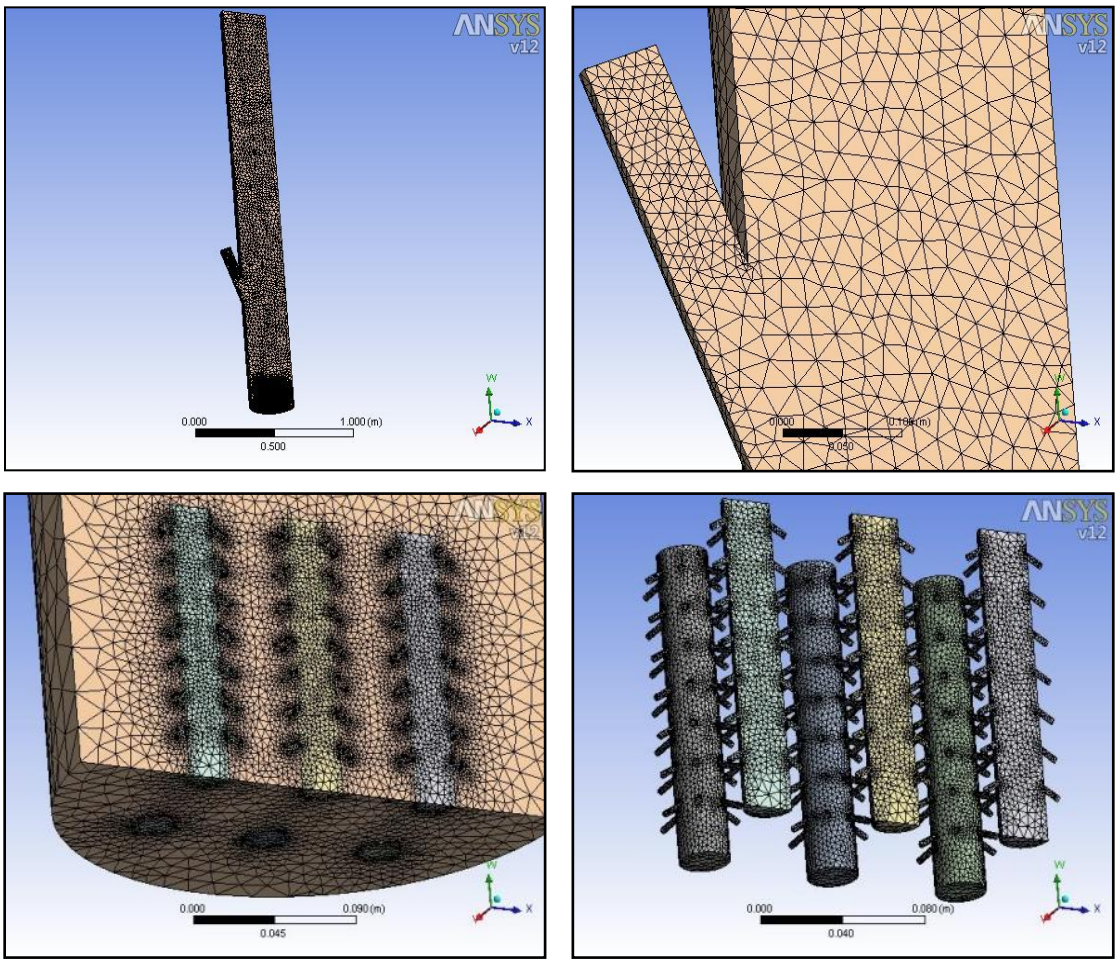

Figure 4.11 The symmetrical 3-D section of non-simplified air distributor model after being meshed in ANSYS Meshing

Figure 4.11 presents the non-simplified air distributor model after meshing with 3.1 million mesh elements. After trials with different mesh element numbers, i.e. 3.1, 3.5, 3.8, 4.7 and 6.7 million elements, it was found that the simulation still faced a divergence with 3.5 million elements, as presented in Figure 4.12. At 3.8 million elements, the simulation

model started to face a good convergence, as presented in Figure 4.13, and was therefore selected to use for further simulation to minimize memory usage and computational time (referring to the effect of mesh element number summarized in Table 4.4). The simplified air distributor model was also checked on the same process to find out the acceptable and suitable mesh element number before being used in this study. The effect of the mesh element number is shown in Table 4.5. At around 67,000 elements, the simulation model started to face a good convergence for the simplified air distributor model.

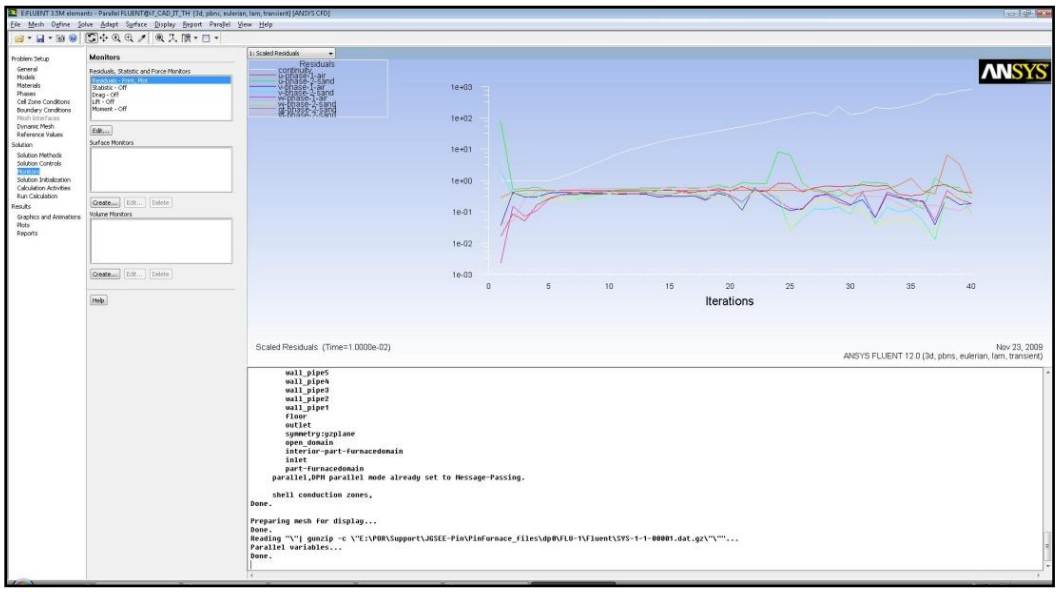

Figure 4.12 The simulation showing divergence

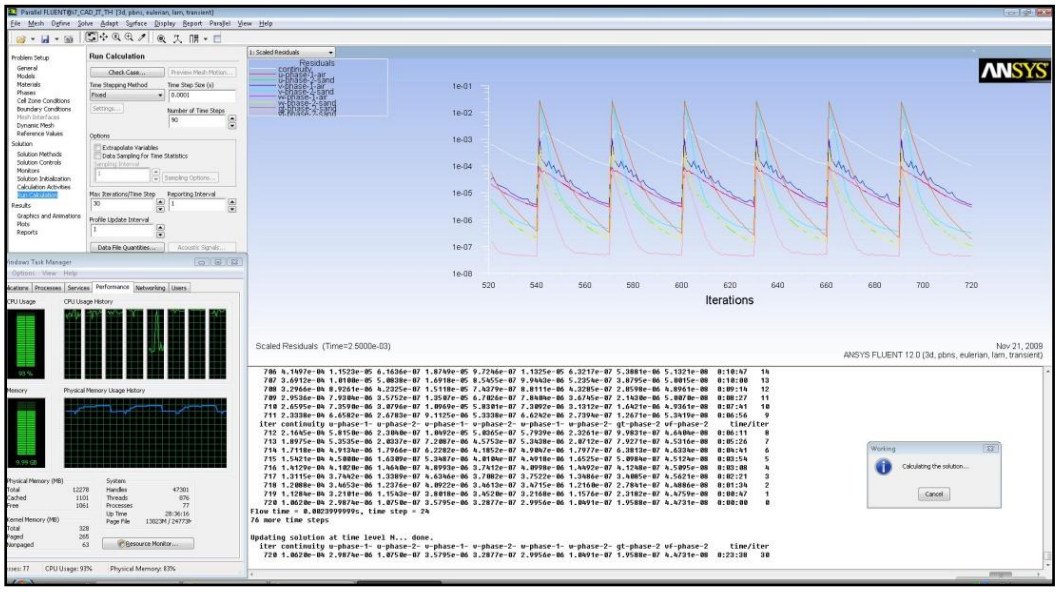

Figure 4.13 The simulation showing good convergence

Table 4.4 Mesh element number effect on simulation process for non-simplified air distributor model.

Number of mesh elements (Million)	Simulation process	Usage time for simulation (min/time step)
3.1	Facing divergence	-
3.5	Facing divergence	-
3.8	Facing convergence	7
4.7	Facing convergence	15
6.7	Facing convergence	24

Table 4.5 Mesh element number effect on simulation process for simplified air distributor model.

Number of mesh elements	Simulation process	Usage time for simulation (second/time step)
41,117	Facing divergence	-
53,735	Facing divergence	-
66,963	Facing convergence	30

4.4 Simulation Investigations: Under Cold Flow Conditions – Feeding Pipe Existence Effect

For the first simplification, an air distributor was designed to be a plate with 9 holes and called the simplified air distributor model. In this simplified air distributor model, the effect of feeding pipe on the simulation result was studied. The simplified air distributor model with feeding pipe (located at about 600 mm above the bottom) named “P9_1” and the simplified air distributor model without feeding pipe named “P9_2”. Figure 4.14 shows the symmetrical 3-D section of these two simplified air distributor models which were created in Design Modeler. The boundary on both P9_1 and P9_2 was set as seen in Figure 4.15. The initial conditions (input parameters) for these two simplified air distributor models were the same and concluded, as presented in Table 4.3.

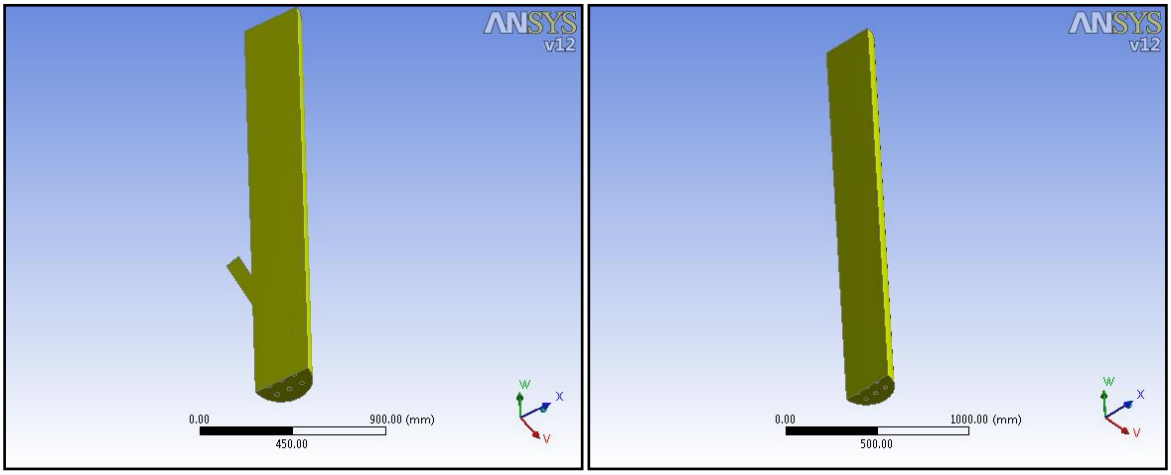

P9_1 P9_2

Figure 4.14 Symmetrical 3-D section of simplified air distributor model with and without feeding pipe.

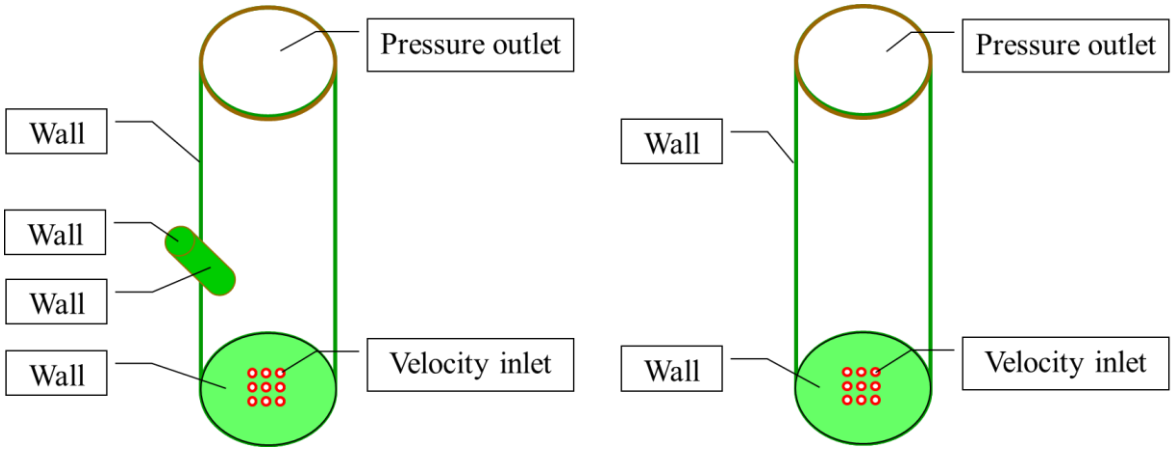

P9_1 P9_2

Figure 4.15 Boundary setting on the simplified air distributor models.

The simulation results showed that the behavior of the silica sand movement inside the bed zone of the "P9_1" model and "P9_2" model were the same. It indicated that the feeding pipe existence had no effect on the model simulation (under cold flow condition) result in terms of both solid volume fraction inside bed zone and absolute pressure along the height of model, as shown in Figure 4.16 and Figure 4.17, respectively. This probably because the bed surface, while fluctuating, did not expand to reach the level of feeding pipe position. Therefore, the other models were created and meshed without feeding pipe before simulation the model under cold flow condition to reduce the complexity of the model and hence to save the computer usage time for simulation.

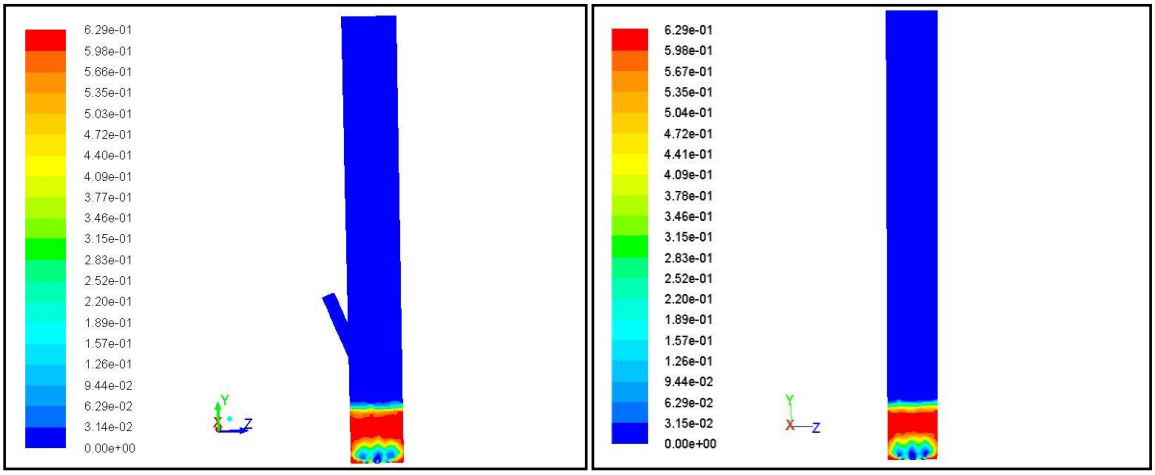

P9_1 P9_2

Figure 4.16 The contour of solid volume fraction at time = 0.3 s.

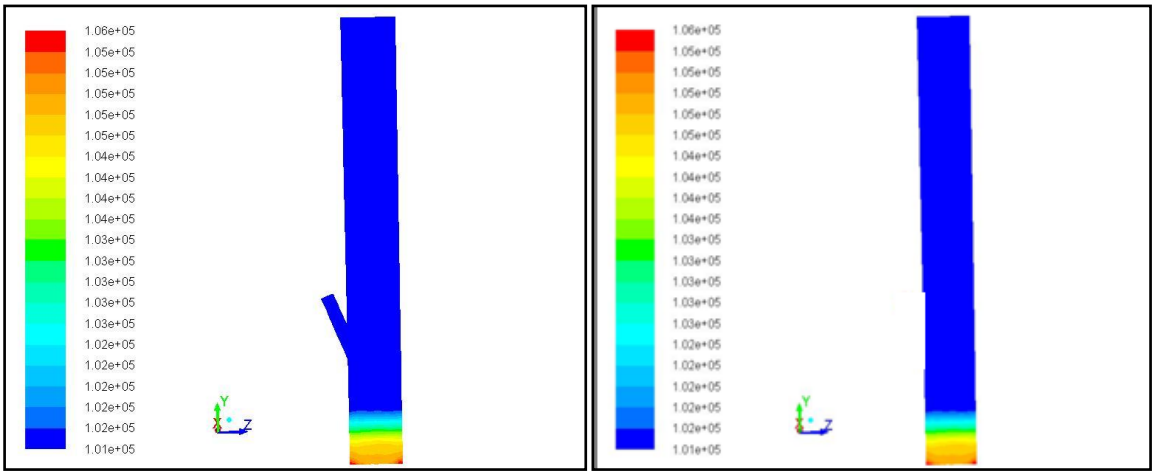

P9_1 P9_2

Figure 4.17 The contour of absolute pressure (Pascal) at time = 0.3 s.

4.5 Simulation Investigations: Under Cold Flow Conditions – Hydrodynamic Behavior inside Bed Zone of Non-Simplified and Simplified Air Distributor in BFBG Model

The simulation results in terms of the solid volume fraction which represents the formation and motion of bubbles inside the bed zone, the gas-solid flow pattern, and the bed expansion ratio. These were compared to show the differences in hydrodynamic behavior obtained from the non-simplified and simplified air distributor model. In addition, the pressure drop across the bed at minimum fluidization velocity resulted from both models were checked.

4.5.1 The bubble formation and motion inside bed zone

The formation and motion of bubbles inside the bed zone of both non-simplified and simplified air distributor model are indicated with solid volume fraction in Figure 4.18 and Figure 4.19. Figure 4.18 shows the differences of solid volume fraction contour, at time of 0 to 0.8 s, obtained from non-simplified and simplified air distributor model. For non-simplified air distributor model, air starts to come out through the 378 air distributing holes around the 9 closed-end nozzles. Due to the less effect of bed weight, more air bubbles occur at the upper part of the nozzles. The small bubbles are formed and grow as ascending toward the bed surface. Bubbles also collide with each other to form larger ones. As the bubbles reach to the bed surface, they burst out. On the other hand, small bubbles are formed near the bottom of the bed for simplified air distributor model, which was designed to be a plate with holes. Larger bubbles were also formed but at time earlier than observed for the non-simplified air distributor model. Other behaviors were also found similar for both models.

Both non-simplified and simplified air distributor models show that, when the bubbles reach the bed surfaces, they erupt and splash solids into the freeboard. This results in the fluctuation of bed surface observed. However, more fluctuation is observed in non-simplified air distributor model and that the loops of bubble formation and motion are also faster in non-simplified air distributor model.

The solid volume fraction is also plotted with the reactor height for both models at time = 0 – 0.4 s, as illustrated in Figure 4.19. The bubbles begin to form at the height of 50 mm from the bottom level for non-simplified air distributor model, while they begin to form at the bottom level for simplified air distributor model. For non-simplified air distributor model, it can clearly be seen that the bubble volume changes from nozzles zone to upper part of bed zone, while the bubbles are more gradually changed from the bottom level to upper part of bed zone in simplified air distributor model as seen by the smaller decreasing of solid volume fraction inside bed zone from about 0.5 at 0.0 s to about 0.3 at 0.4 s. In addition, the bubbles reach faster to the bed surface in non-simplified air distributor model.

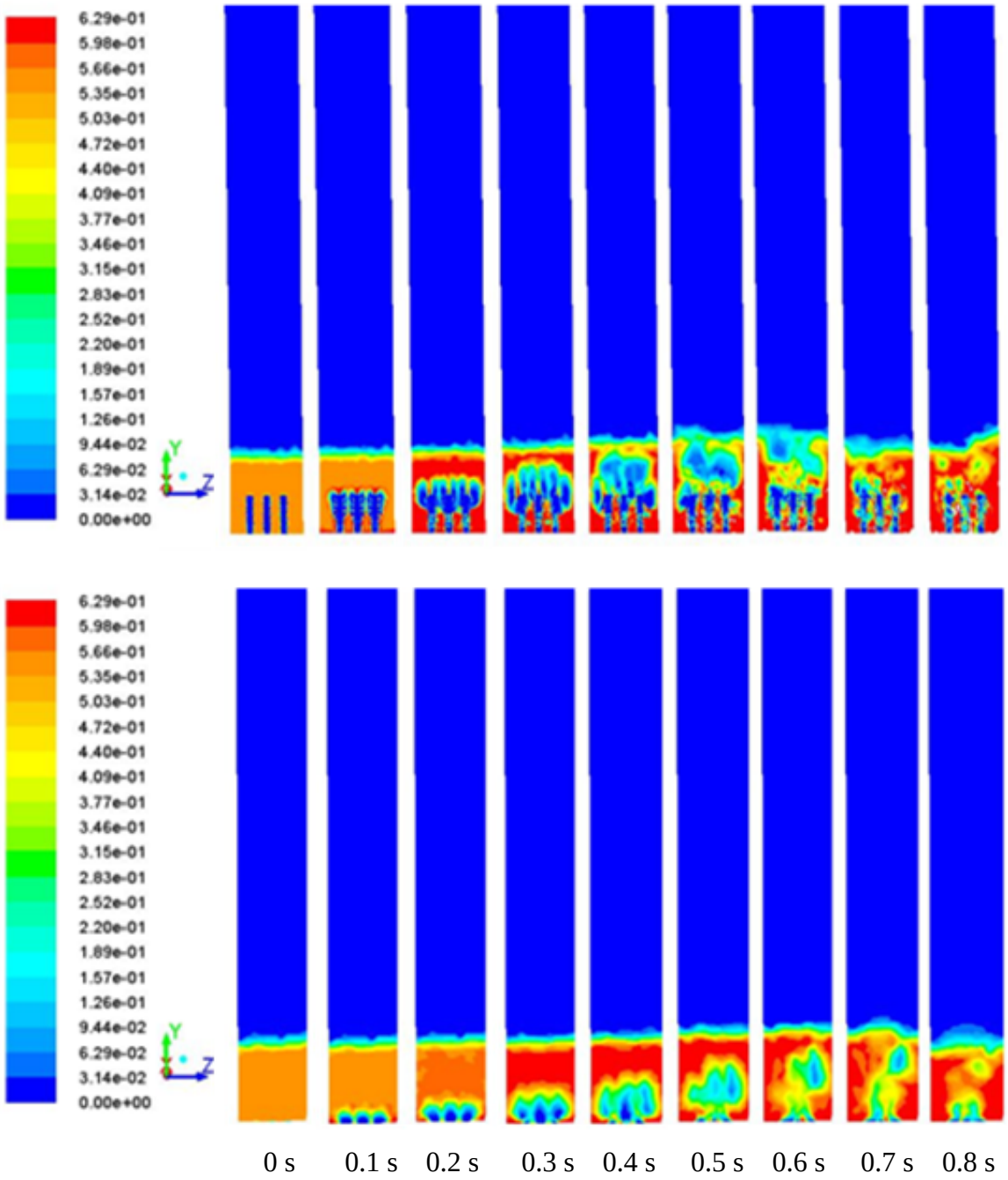

Figure 4.18 Contours of solid volume fraction at time = 0 to 0.8 s obtained from non-simplified model (top) and simplified model (below).

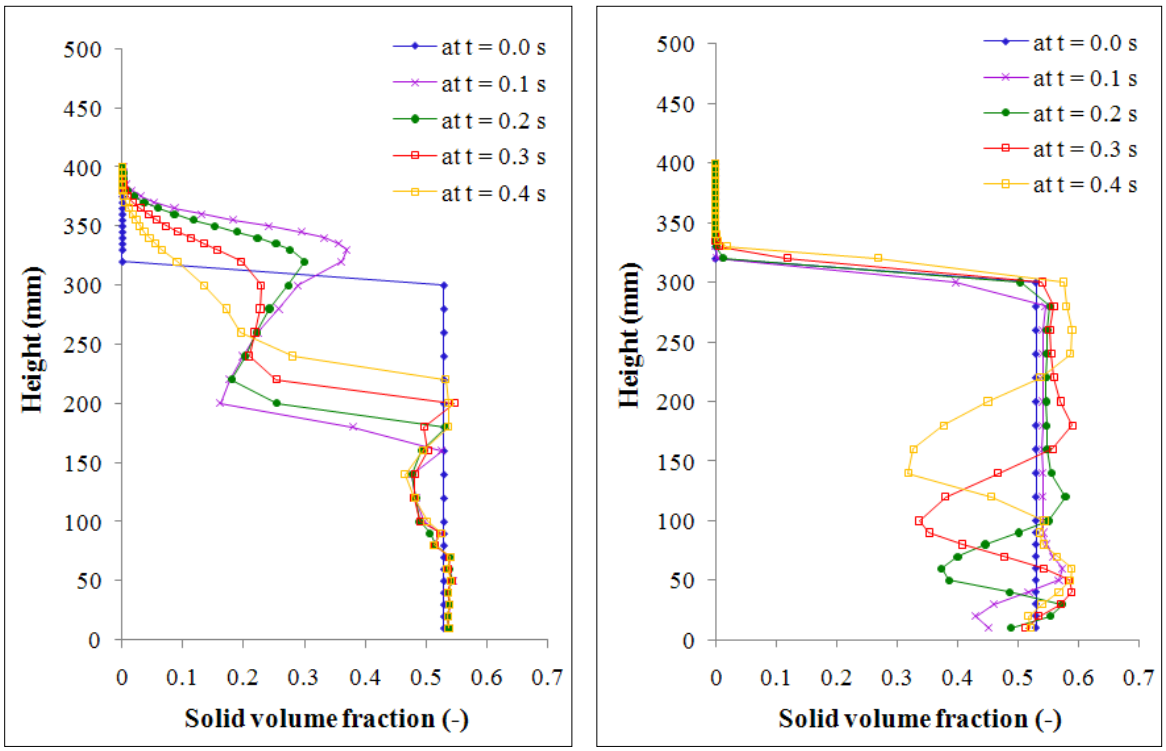

Figure 4.19 Solid volume fraction along the height of non-simplified air distributor model (left) and simplified air distributor model (right) at time = 0 to 0.4 s.

4.5.2 The gas-solid flow pattern

Figure 4.20 compares the results of the solid velocity and flow directions inside the bed zone of the non-simplified and simplified air distributor model during the beginning period of fluidization, i.e. at time of 0.05 and 0.50 s. The differences in gas-solid flow patterns were already seen at these times. For non-simplified air distributor model, solids around nozzles zone start to move downward after gas begins to flow through the air distributors as seen in Figure 4.20 (left) at time of 0.05 s. Higher gas flow preferably happens at the upper part of nozzles due to less solid weight load and as a consequence pushes the solids toward the bottom until the force of gas at the bottom is high enough to push the solids back to move upward as shown in Figure 4.20 (left) at time of 0.50 s. By this force (continuing simulation), the solids in upper zone still remain at rest until a rising bubble moves up to their vicinity. Then on the way up through the bed, bubbles retreat solids into the wake underneath them and thereby set the solids in motion.

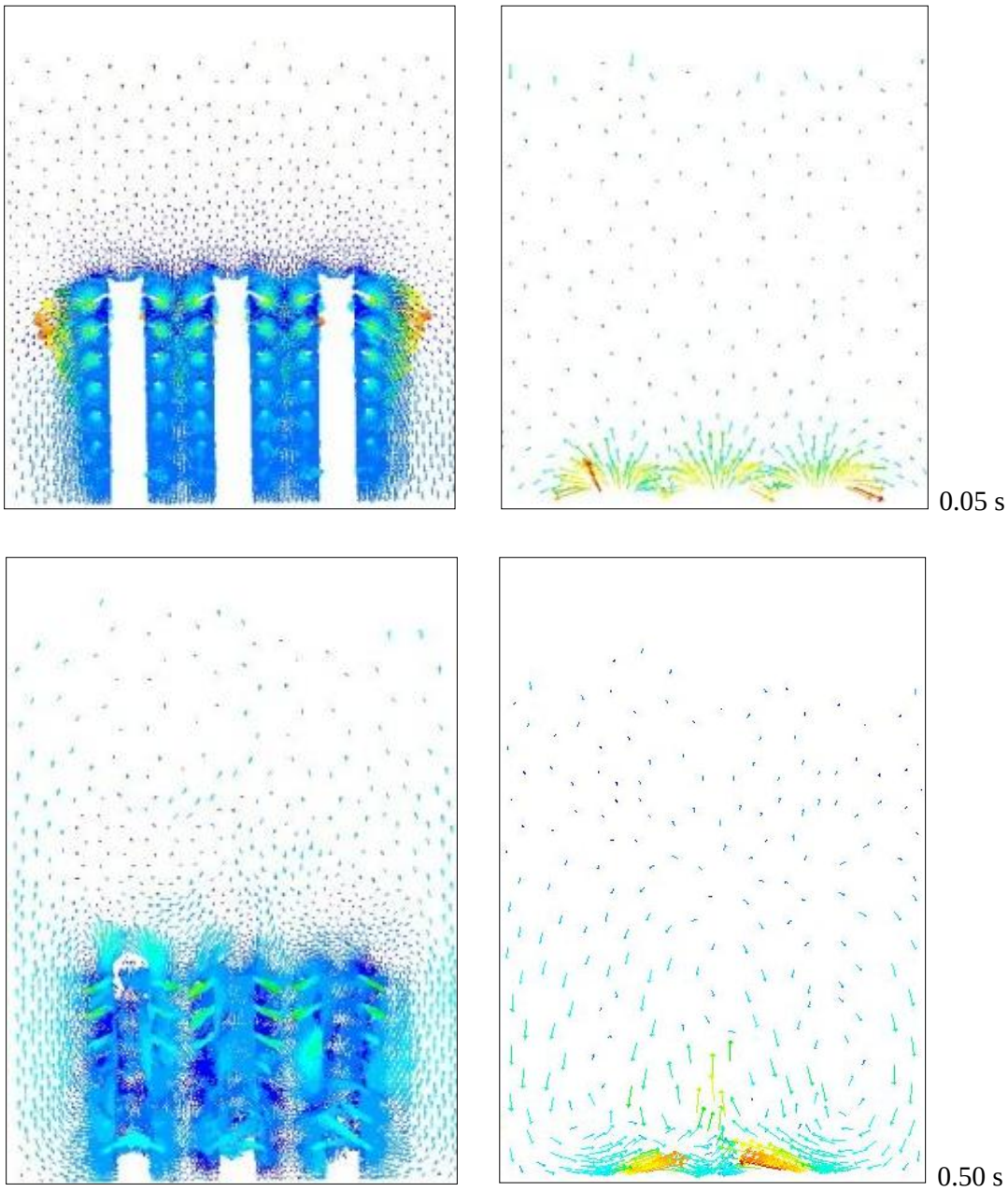

Figure 4.20 Solid velocity and direction inside bed zone of non-simplified air distributor model (left) and simplified air distributor model (right) at time = 0.05 s (top) and 0.50 s (below).

For the simplified air distributor model, the solids near the bottom had high acceleration due to the action of the gas flow inlet, while the solids on the top of the bed moved downward by gravity, as presented in Figure 4.20 (right) at time of 0.05 s. Gas drives solids until an ascending flow occurs around the center and a descending flow is near the wall when vortex patterns are created inside the bed as illustrated in Figure 4.20 (right) at time of 0.50 s.

The gas-solid flow pattern in the simplified air distributor model is different from that in the non-simplified air distributor model as there were large vortexes in the lower part of the bed in the simplified air distributor model, while the gas-solid flow mainly occurred around the nozzles in the non-simplified air distributor model, resulting in large vortexes in the upper part of the bed.

4.5.3 The bed expansion ratio

The quasi-steady state bed height obtained from the non-simplified model simulation was about 400 mm, while it was about 350 mm in the simplified model. Based on the same initial bed height for both non-simplified and simplified model was 300 mm, the bed expansion ratio of non-simplified and simplified model was 1.33 and 1.16, respectively. The bed expansion ratio is an important parameter as it is normally used for fixing the height of fluidized bed required for a particular service [76]. The difference of these comparison bed expansion ratios indicated that even though the simulation on simplified model had also shown the bed movement, the expansion height of fluidized bed was underestimated as compared to the non-simplified model which is closer to the actual BFBG.

4.5.4 The pressure drop across the bed at minimum fluidization velocity

The simulation results obtained from both the non-simplified and simplified air distributor models show the same pressure drop of 40.79 cm w.g. across the bed, as presented in Figure 4.21.

However, the profiles of absolute pressure along the height are different. The absolute pressure at each height in the simplified air distributor model was nearly constant, while the fluctuations were clearly observed in the non-simplified air distributor model, especially in the upper zone of the bed.

In the hot flow (reaction considered) model, the different absolute pressure contours may have affected the chemical equilibrium state, following Boyle's Law, which states that the absolute pressure exerted by a given mass of an ideal gas is inversely proportional to the volume it occupies if the temperature and the amount of gas remain unchanged within a closed system.

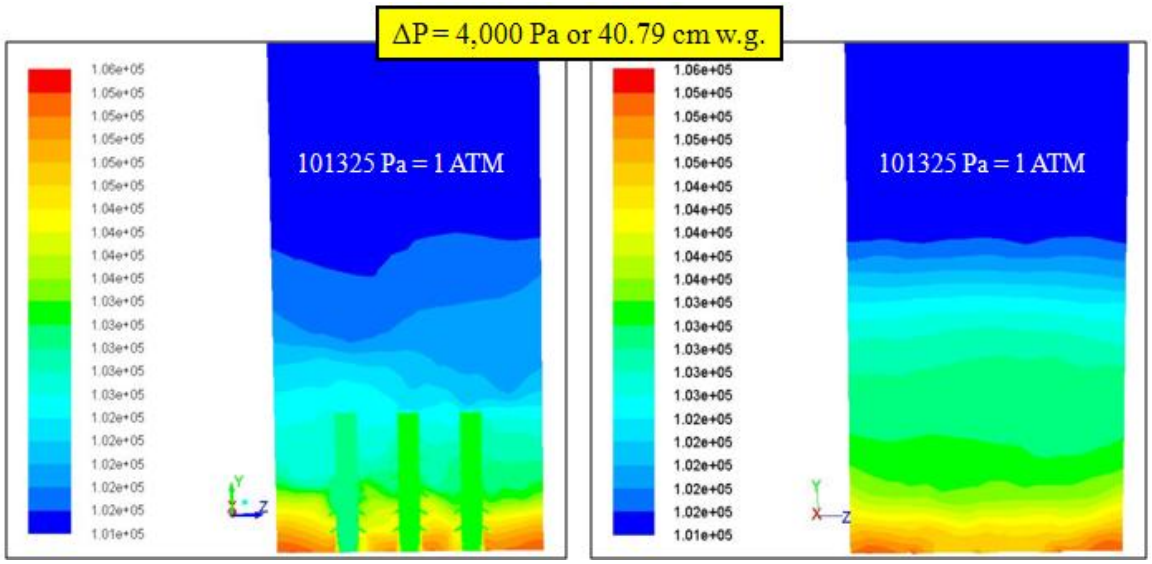

Figure 4.21 Contour of absolute pressure along the height of non-simplified air distributor model (left) and simplified air distributor model (right) at time = 0.5 s.

4.6 Simulation Investigations: Under Elevated Temperature Conditions

After the silica sand (bed material), in terms of the solid phase, was re-patched with the temperature at 800°C in both the non-simplified and simplified air distributor models, the model of "Energy" in Solution Setup step was turned on to allow the heat transfer between the solid and gas phases. The effect of this hot sand with heat transfer on the hydrodynamic behavior inside bed zone of non-simplified and simplified air distributor in BFBG model was investigated and found that the bubbles which occurred under elevated temperature condition moved up to the bed surface faster than that occurred under cold flow condition in both non-simplified and simplified air distributor model as presented in Figure 4.22 and Figure 4.23, respectively. This is because the density of any gas, including air, decrease as the temperature increase. With this less density, the molecules of air move further apart and easily move up toward the bed surface. Under elevated temperature condition, the air temperature was increased by heat transfer from hot sand when the air flew pass through it.

Furthermore, the simulation under elevated temperature conditions also showed a lower pressure drop across the bed compared to the simulation under cold flow conditions in both non-simplified and simplified air distributor models, as presented in Figures 4.24 and 4.25, respectively. A similar study by Gimbun et al. [77] explained that the lower gas

density due to the higher temperature creates a lower dynamic pressure resulting in the lower pressure drop.

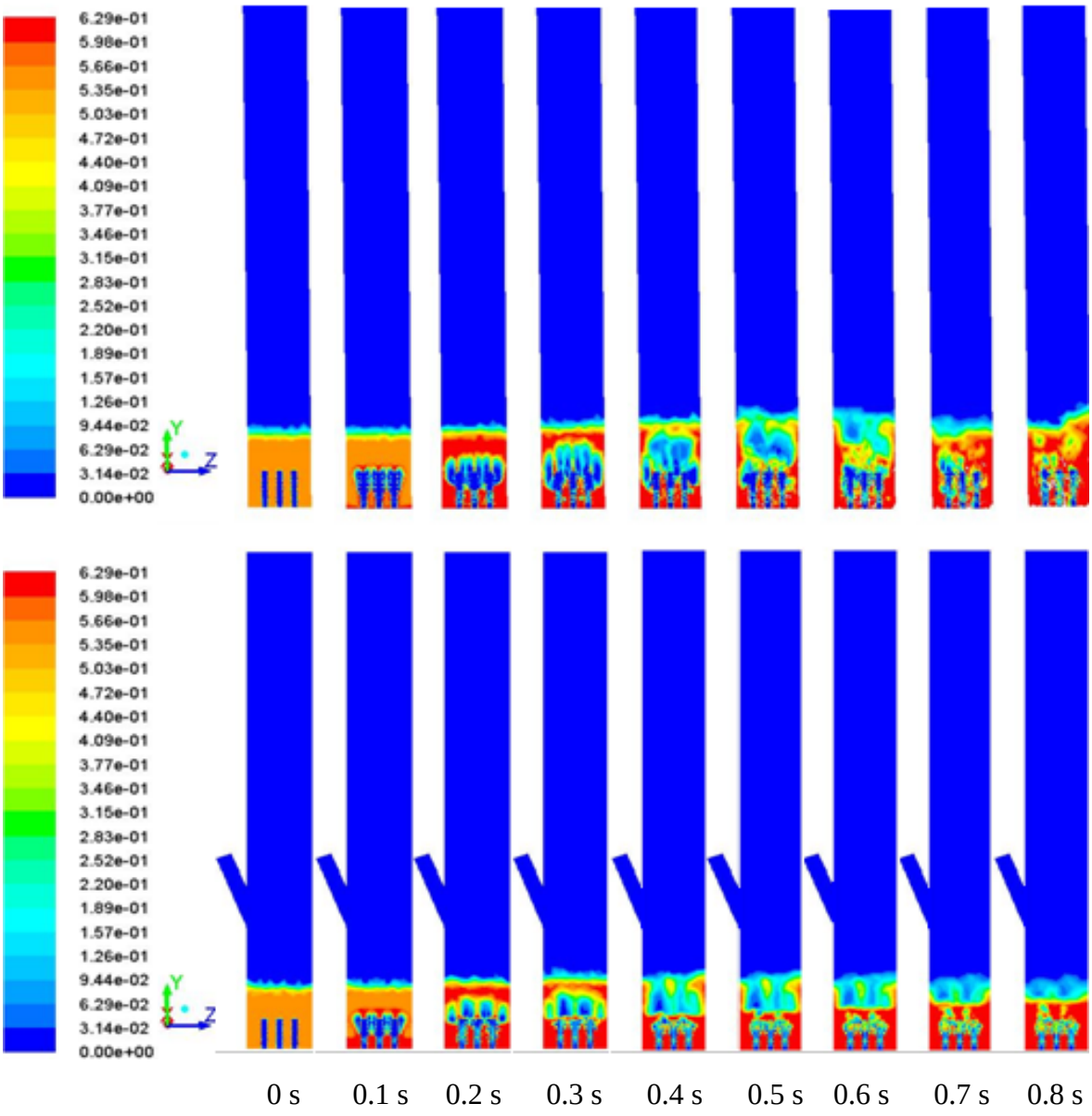

Figure 4.22 Comparison of the contours of solid volume fractions resulting from cold flow conditions (top) and elevated temperature conditions (below) in the non-simplified air distributor model at time = 0 to 0.8 s.

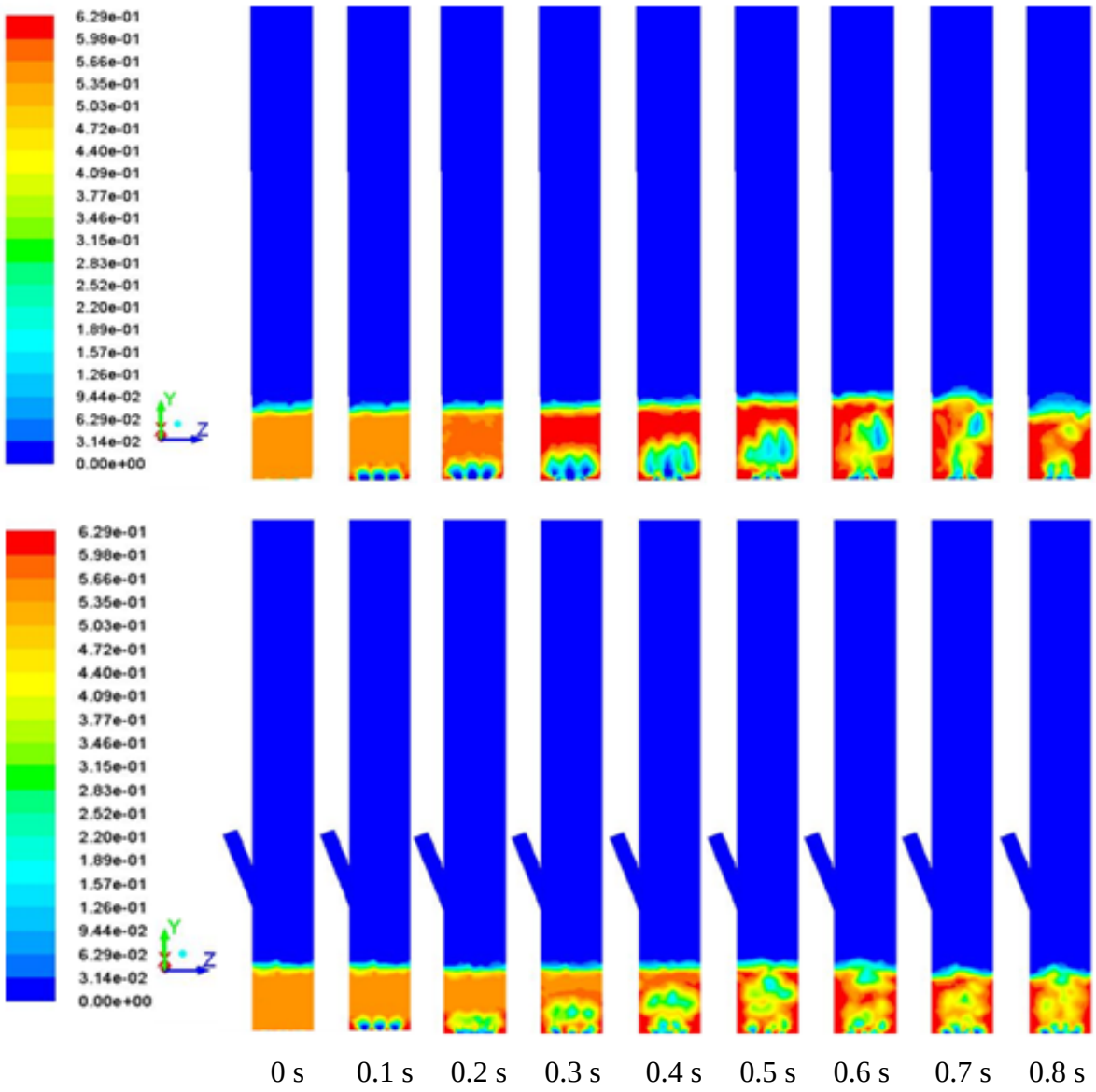

Figure 4.23 Comparison of the contours of solid volume fractions resulting from cold flow conditions (top) and elevated temperature conditions (below) in the simplified air distributor model at time = 0 to 0.8 s.

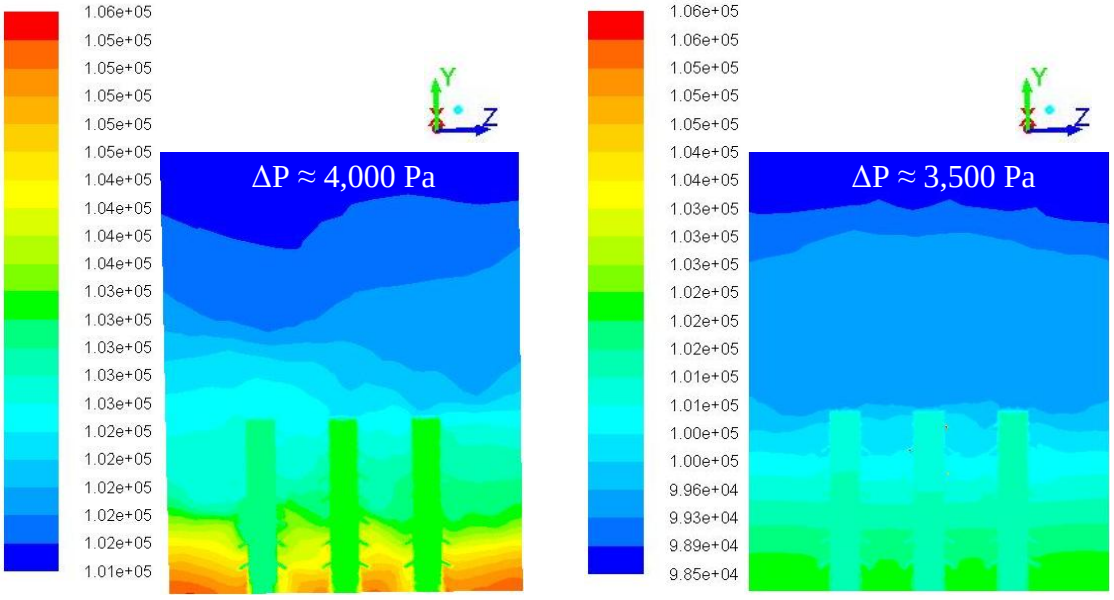

Cold flow Elevated temperature

Figure 4.24 Comparison inside the bed zone of the contours of absolute pressure resulting from cold flow conditions (left) and elevated temperature conditions (right) in the non-simplified air distributor model at time = 0.5 s.

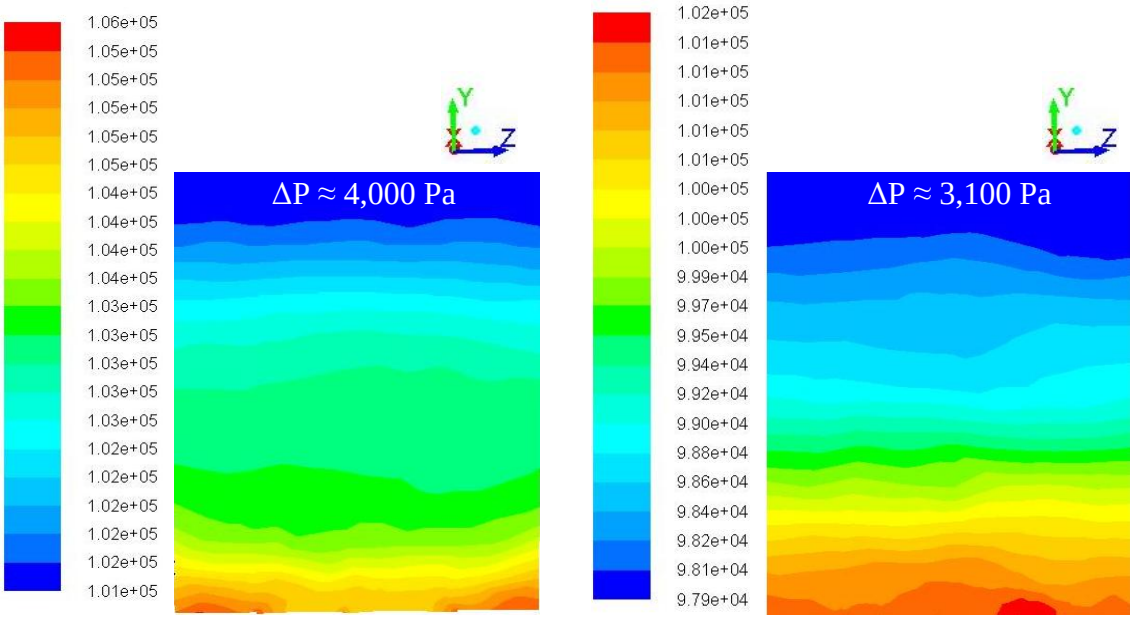

Cold flow Elevated temperature

Figure 4.25 Comparison inside the bed zone of the contours of absolute pressure resulting from cold flow conditions (left) and elevated temperature conditions (right) in the simplified air distributor model at time = 0.5 s.

Figures 4.24 and 4.25 also show that the non-simplified air distributor model causes a higher pressure drop across the bed than does the simplified one when the model was simulated under elevated temperature conditions, while there was the same pressure drop across the bed in both air distributor models when the models were simulated under cold flow condition. This is probably due to the effect from the "Energy" in Solution Setup step was turned on to allow heat transfer from solid phase to gas phase in the case of simulation under elevated temperature condition. Then the physical structure of the model plays important role in the energy equation (e.g. the convective energy transfer due to rotational or translational motion of the solids, the velocity field which is computed from the motion specified for the solid zone, the heat flux due to conduction, and the volumetric heat sources within solid) and dominates the pressure drop across the bed.

4.7 Simulation Investigation: The Usage Time for Simulations

A stand-alone computer with 8 core processors was used in this research for model simulations. The time step size (s), which is the size of incremental change in time for solving the governing equations, was varied from $1x10^{-4}$ to $1x10^{-7}$ depending on the complexity of the model. A more complex model would need the smaller time step size. The usage time for all model simulations are summarized in Tables 4.6 and 4.7.

Table 4.6 The usage time for simulation under cold flow conditions.

Model	Time step size (s)	Usage time for simulation	
		(seconds/time step)	Computational time needed for 1 second in simulation (days)
Non-simplified	$1x10^{-4}$	420	49
Simplified	$1x10^{-4}$	30	4

Table 4.7 The usage time for simulation under elevated temperature conditions.

Model	Time step size (s)	Usage time for simulation	
		(seconds/time step)	Computational time needed for 1 second in simulation (days)
Non-simplified	$1x10^{-6}$	33	382
Simplified	$1x10^{-4}$	177	21

Tables 4.6 and 4.7 show that under both cold flow and elevated temperature conditions, the usage time for the non-simplified air distributor model simulation was more than ten times longer than that for the simplified one. This is due to the non-simplified air distributor model has higher number of mesh element and more complex when compared to the simplified one.

For the non-simplified air distributor model simulation, the usage time for simulation under elevated temperature conditions was about eight times longer than under cold flow conditions. While it was about five times longer in case of simplified air distributor model simulation. This is because the number of equation which had been used in FLUENT to simulate the model under elevated temperature condition is more than that to simulate the model under cold flow condition.

In addition, the non-simplified air distributor model simulation took 420 seconds per time step under cold flow conditions while it took only 33 seconds per time step under elevated temperature conditions. However, the computational time needed for 1 second in simulation under elevated temperature was 382 days which is much longer than that of 49 days for the simulation under cold flow condition. This contrast occurred from the difference of time step size that had been used for the simulations. While using the same time step size, this contrast was not happened as seen in the case of simplified air distributor model simulation.

CHAPTER 5
CONCLUSIONS AND RECOMMENDATIONS FOR FUTURE WORK

5.1 Conclusions

There were two main parts in this research. The first one focused on the experimental gasification in the 100 kWth lab-scale bubbling fluidized bed reactor. The second part was the CFD simulation of a BFBG model. This second part had also been separated into two parts: the CFD model validation under cold flow condition and the model simulation investigation which studies the hydrodynamic behaviors inside bed zone of non-simplified and simplified air distributor in a BFBG model under cold flow condition and elevated temperature condition. In the CFD simulation of a BFBG model part, the mesh element number effect, the feeding pipe existence effect, and the usage time for all model simulations had also been studied. Moreover, both CFD model validation part and model simulations investigation part were studied in case of three-dimensional simulation by using a commercially available CFD code called FLUENT.

For the experimental gasification part, the potential of the co-gasification of high-moisture (27% M.C.) rubber woodchips mixed with plastic waste (SPB) at different weight ratios was investigated in a bubbling fluidized bed gasifier. The main objective is to examine the technical feasibility of the operation of plastic waste gasification, with the purpose of developing an environmentally acceptable process to decrease the amount in the waste stream through energy recovery. The proportion of plastic waste to biomass was studied to solve the moisture problem on biomass gasification. The effect of air to fuel ratio (presented in term of equivalence ratio - ER) and plastic waste addition ratio on gasification performance and quality of gas product were investigated and compared with those obtained from the pre-dried woodchip (8.5% M.C.).

The SPB addition was found to significantly improve the gasification performance for both the product gas quality and carbon conversion efficiency. CO_2 generation was diminished while CO and H_2 release increased with the increasing weight proportion of SPB in the fuel mixture at all ERs. This is probably due to the increase of reactor temperature with increasing the SPB in the fuel mixture. Even at 10% mixing ratio, the HHV of the product gas increased by about 50% and 25% compared to the case of high-moisture rubber woodchips and pre-dried rubber woodchips (8.5% M.C.), respectively. At

20% mixing ratio, the HHV of product gas was increased from 3.85 (the case of high-moisture rubber woodchips) to 6.06 MJ/Nm^3. The carbon conversion efficiency could be significantly improved to reach the level of the pre-dried woodchip when mixing with 20% SPB. Moreover, increasing ER could effectively increase the carbon conversion efficiency at all feedstock conditions. From the results obtained, therefore, the co-gasification with plastic waste can be considered as a promising solution for utilizing high-moisture biomass like rubber woodchip. Moreover, it can also be an effective way for waste management because not only the waste is eliminated but also used as fuel.

Prior to the model simulation investigation part, the acrylic reactor was built (to have the ratio of diameter to height the same as that of the BFBG used in the first part of this research) and used in the experiment part to compare with the acrylic model simulation results for the CFD model validation. Thereby, the input parameters (such as a specularity coefficient of the momentum-shear condition, and a restitution coefficient of the multiphase-granular property) and the optional model selections (e.g., the model of fluid-solid exchange coefficient) were studied. There were found that the model simulation results under the cold flow condition start to be close to the nature behavior after decreasing in the restitution coefficient and specularity coefficient for the solid phase. Furthermore, the Gidaspow model which is recommended for dense fluidized beds was used to represent the terms of interphase exchange coefficient in this study as the bed zone of BFBG is a dense one.

After all the input parameters and optional model selection were studied and validated until they were acceptable, they were used for the next part in the model simulation investigation, for which the model was created by using the BFBG as a prototype. There was found that the acceptable and suitable mesh element number for non-simplified and simplified air distributor model were around 3.8 million elements and 67,000 elements, respectively. In addition, the feeding pipe existence had no effect on model simulation (under cold flow condition) result in terms of both solid volume fraction inside bed zone and absolute pressure along the height of model. The model simulations (under cold flow condition) results also show that although the bubbles formation and motion obtained from both non-simplified and simplified air distributor model were occurred with the same processes, there still were a lot differences in hydrodynamic behavior, i.e. bed expansion ratio, bubble appearance, and gas-solid flow patterns inside the bed zone. More fluctuation is presented in non-simplified air distributor model. The

loops of bubble formation and motion are also faster in non-simplified air distributor model. For the gas-solid flow pattern, there are large-size vortexes in lower part of the bed in simplified air distributor model while the gas-solid flow mainly occurs around the nozzles in non-simplified air distributor model resulting in large-size of vortexes in upper part of the bed. Furthermore, the bed expansion ratio obtains from simplified air distributor model is lower than that obtains from non-simplified one. In addition, the model simulation under elevated temperature resulted to a lower pressure drop across the bed when compared to the one that obtained from the simulation under cold flow condition and the occurred bubbles under elevated temperature condition move up to the bed surface faster than that occurred under cold flow condition in both non-simplified and simplified air distributor model because the decrease in air density and dynamic pressure with increasing the temperature.

This model simulation investigation part, under both cold flow and elevated temperature conditions, proposed to illustrate the differences in hydrodynamic behaviors inside the bed zones of both the non-simplified and simplified air distributors, which is probably useful for further BFBG study and development.

5.2 Recommendations for Future Work

To gain more understanding of the hydrodynamic and thermodynamic behaviors of the gasification process for further BFBG study and development, the model simulation under hot flow (reaction considered) conditions is essential. With limitations in computer power and time, the model simulation under hot flow condition had been studied but not yet finished in this research, as presented in Appendix C. To complete this part, a computer cluster is needed.

To quickly improve and develop a CFD model to simulate the thermodynamic and hydrodynamic behaviors of a bubbling fluidized bed reactor for biomass gasification, a good understanding of the software’s nature and how to use it (as new versions are regularly released) is important. Therefore, continuous learning of the software is necessary. Furthermore, an understanding of the nature of bubbling fluidized bed gasification is also important for creating the model and setting conditions for simulation.

In this study, there was only one type of plastic waste, i.e. High Density Polyethylene (HDPE) type, which had been used to gasify with high-moisture rubber woodchips. Therefore, using the different types of plastic waste might cause to the different results. An example of other plastic type is the Polypropylene (PP) which was studied by Aznar et al. [67] and found that the PP type has the content of carbon and hydrogen about 70% and 12%, respectively which are lower than those in HDPE type. Therefore, adding PP in the fuel mixture may result in the lower content of hydrogen and carbon, which means that the reactants are decreased, so this might cause of the lower H_2, CO, CH_4, and C_2H_n release when compared to the adding of HDPE in the fuel mixture. In addition, the characteristics in each type of plastic are also different and probably plays an important role in the gasification system.

Not just the fuel composition, but also the variations in reactor temperature and the variations in ER play an important role in the gasification system, as seen in this study. The optimization of these factors affecting the gasification system is essential. Most studies had been using the experiment to find out these optimizations, but using CFD with the computer cluster to simulate the reactor model might be a tool to reduce cost and time for further optimizations study.

REFERENCES

[1] Quaak, P., Knoef, H. and Stassen, H. (1999), Energy from Biomass a Review of Combustion and Gasification Technologies, World Bank Technical Paper, Energy Series, 422.

[2] Jurado, F., Cona, A. and Carpio, J. (2003), Modelling of combined cycle power plants using biomass, Renewable Energy, 28, pp. 743-753.

[3] Herguido, J., Corella, J. and González-Saiz, J. (1992), Steam gasification of lignocellulosic residues in a fluidized bed at a small pilot scale. Effect of the type of feedstock, Industrial & Engineering Chemistry Research, 31, pp. 1274–1282.

[4] Narváez, A.O., Corella, J. and Aznar, M.P. (1996), Biomass gasification with air in an atmospheric bubbling fluidized bed. Effect of six operational variables on the quality of the produced raw gas, Industrial & Engineering Chemistry Research, 35, pp. 2110–2120.

[5] Gil, J., Aznar, M.P., Caballero, M.A., Francés, E. and Corella, J. (1997), Biomass gasification in fluidized bed at pilot scale with steam–oxygen mixtures. Product distribution for very different operating conditions, Energy and Fuels, 11, pp. 1109–1118.

[6] Gibbs, A. (2002). "Energy from Waste". Available online: http://www. wasteresearch.co.uk/ade/efw/rig.htm

[7] Gómez-Barea, A.G., Arjona, R. and Ollero, P. (2005), Pilot-plant gasification of olive stone: a technical assessment, Energy & Fuels, 19, pp. 598-605.

[8] Kaewluan, S. and Pipatmanomai, S. (2007), Preliminary Study of Rubber Wood Chips Gasification in a Bubbling Fluidised-Bed Reactor: Effect of Air to Fuel Ratio, paper presented in the, PSU-UNS International Conference on Engineering and Environment, Prince of Songkhla University, Faculty of Engineering, Hat Yai, Songkhla, Thailand.

[9] Wilson, L. and John, G.R. (2011), Effects of moisture content in biomass gasification, Second International Conference on Advances in Engineering and Technology, pp. 565-571.

[10] Sanz, A. and Corella, J. (2006), Modeling circulating fluidized bed biomass gasifiers, Results from a pseudo-rigorous 1-dimensional model for stationary state, Fuel Processing Technology, 87, pp. 247-258.

[11] Lyubina, Y.L. and Suris, A.L. (1999), Thermodynamic model of the plasma gasification of organic solid waste, Chemical and Petroleum Engineering, 35, pp. 403-406.

[12] NNFCC. (2009), "Final report: Review of technologies for gasification of biomass and wastes", E4Tech, Available online: http://www.ecolateral.org/review-of-technologies-for-gasification-of-biomass-and-wastes/

[13] Elliott, D.C. (2008), Catalytic hydrothermal gasification of biomass, Biofuels Bioproducts & Biorefining, 2, pp. 254-265.

[14] André, R.N., Pinto, F., Franco, C., Dias, M., Gulyurtlu, I., Matos, M.A.A. and Cabrita, I. (2005), Fluidised bed co-gasification of coal and olive oil industry wastes, Fuel, 84, pp. 1635-1644.

[15] Kaewluan, S. and Pipatmanomai, S. (2011), Gasification of high moisture rubber woodchip with rubber waste in bubbling fluidized bed, Fuel Processing Technology, 92, pp. 671-677.

[16] Yuu, S., Umekage, T. and Johno, Y. (2000), Numerical simulation of air and particle motions in bubbling fluidized bed of small particles, Powder Technology, 110, pp. 158-168.

[17] Yu, L., Lu, J., Zhang, X. and Zhang, S. (2007), Numerical simulation of the bubbling fluidized bed coal gasification by the kinetic theory of granular flow (KTGF), Fuel, 86, pp. 722-734.

[18] Rhodes, M.J., Wang, X.S., Nguyen, M., Stewart, P. and Liffman, K. (2001), Use of discrete element method simulation in studying fluidization characteristics: influence of interparticle force, Chemical Engineering Science, 56, pp. 69-76.

[19] Kuwagi, K. and Hoiro, M. (2002), A numerical study on agglomerate formation in a fluidized bed of fine cohesive particles, Chemical Engineering Science, 57, pp. 4737-4744.

[20] Kaneko, Y., Shiojima, T. and Horio, M. (1999), DEM simulation of fluidized beds for gas-phase olefin polymerization, Chemical Engineering Science, 54, pp. 5809-5821.

[21] Limtrakul, S., Chalermwattanatai, A., Unggurawirote, K., Tsuji, Y., Kawaguchai, T. and Tanthapanichakoon, W. (2003), Discrete particle simulation of solids motion in a gas-solid fluidized bed, Chemical Engineering Science, 58, pp. 915-921.

[22] Wang, X.S. and Rhodes, M.J. (2003), Determination of particle residence time at the walls of gas fluidized beds by discrete element method simulation, Chemical Engineering Science, 58, pp. 387-395.

[23] Kafui, K.D., Thornton, C. and Adams, M.J. (2002), Discrete particle-continuum fluid modelling of gas-solid fluidised beds, Chemical Engineering Science, 57, pp. 2395-2410.

[24] Gera, D., Gautam, M., Tsuji, Y., Kawaguchi, T. and Tanaka, T. (1998), Computer simulation of bubbles in large-particle fluidized beds, Powder Technology, 98, pp. 38–47.

[25] Chiesa, M., Mathiesen, V., Melheim, J.A. and Halvorsen, B. (2005), Numerical simulation of particulate flow by the Eulerian–Lagrangian and the Eulerian–Eulerian approach with application to a fluidized bed, Computers & Chemical Engineering, 29, pp. 291–304.

[26] Ding, J. and Gidaspow, D. (1990), A bubbling fluidization model using kinetic theory of granular flow, AlChE Journal, 36, pp. 523-538.

[27] Gamwo, I.K., Soong, Y. and Lyczkowski, R.W. (1999), Numerical simulation and experimental validation of solids flows in a bubbling fluidized bed, Powder Technology, 103, pp. 117-129.

[28] Gidaspow, D. (1994), Multiphase flow and fluidization: Continuum and kinetic theory descriptions, Academic Press, New York.

[29] Enwald, H. and Almstedt, A.E. (1999), Fluid dynamics of a pressurized fluidized bed: comparison between numerical solutions from two-fluid models and experimental results, Chemical Engineering Science, 54, pp. 329-342.

[30] Huilin, L., Gidaspow, D., Bouillard, J. and Wentie, L. (2003), Hydrodynamic simulation of gas–solid flow in a riser using kinetic theory of granular flow, Chemical Engineering Journal, 95, pp. 1–13.

[31] Cooper, S. and Coronella, C.J. (2005), CFD simulations of particle mixing in a binary fluidized bed, Powder Technology, 151, pp. 27-36.

[32] Sun, J. and Battaglia, F. (2006), Hydrodynamic modeling of particle rotation for segregation in bubbling gas-fluidized beds, Chemical Engineering Science, 61, pp. 1470-1479.

[33] Huilin, L., Yunhua, Z, Ding, J., Gidaspow, D. and Wei, L. (2007), Investigation of mixing/segregation of mixture particles in gas-solid fluidized beds, Chemical Engineering Science, 62, pp. 301-317.

[34] Benyahia, S., Arastoopour, H., Knowlton, T.M. and Massah, H. (2000), Simulation of particles and gas flow behavior in the riser section of a circulating fluidized bed using the kinetic theory approach for the particulate phase, Powder Technology, 112, pp. 24-33.

[35] Breault, R.W. (2010), Gasification Processes old and new: A basic review of the major technologies, Energies, 3, pp. 216-240.

[36] Gerber, S., Behrendt, F. and Oevermann, M. (2010), An Eulerian modeling approach of wood gasification in a bubbling fluidized bed reactor using char as bed material, Fuel, 89, pp. 2903-2917.

[37] Basu, P. (2006), Combustion and Gasification in Fluidized Beds, Taylor & Francis Group, Boca Raton.

[38] Kunii, D. and Levenspiel, O. (1991), Fluidization Engineering, Butterworth-Heinemann, Newton, MA.

[39] Rhodes, M. (1998), Introduction to Particle Technology, Wiley, Chichester.

[40] Ravelli, S., Perdichizzi, A. and Barigozzi, G. (2008), Description, applications and numerical modelling of bubbling fluidized bed combustion in waste-to-energy plants, Progress in Energy and Combustion Science, pp. 224-253.

[41] Davidson, J.F. and Harrison, D. (1963), Fluidized Particles, Cambridge University Press, New York.

[42] Versteeg, H.K. and Malalasekera, W. (1995), An Introduction to Computational Fluid Dynamics: The Finite Volume Method, Longman Scientific & Technical, England.

[43] Singh, R.I., Brink, A. and Hupa, M. (2013), CFD modeling to study fluidized bed combustion and gasification, Applied Thermal Engineering, 52, pp. 585-614.

[44] Wang, Y. and Yan, L. (2008), Review CFD studies on biomass thermochemical conversion, International Journal of Molecular Sciences, 9, pp. 1108-1130.

[45] Eaton, A.M., Smoot, L.D., Hill, S.C. and Eatough, C. N. (1999), Components, formulations, solutions, evaluation, and application of comprehensive combustion models. Progress in Energy and Combustion Science, 25, pp. 387-436.

[46] Warnatz, J., Maas, U. and Dibble, R.W. (2001), Combustion Physical and Chemical Fundamentals, Modeling and Simulation, Experiments, Pollutant Formation, Springer, New York.

[47] Bakul, C.E.J., Gershtein, V.Y. and Xianming, L. (2000), Computational Fluid Dynamics in Industrial Combustion, CRC Press, New York.

[48] Armstrong, L.M., Gu, S. and Luo, K.H. (2011), Parametric study of gasification processes in a BFB coal gasifier, Industrial and Engineering Chemistry Research, 50, pp. 5959-5974.

[49] Lun, C.K.K., Savage, S.B., Jeffrey, D.J. and Chepurniy, N. (1984), Kinetic theories for granular flow: inelastic particles in Couette flow and slightly inelastic particles in a general flowfield, Journal of Fluid Mechanics, 140, pp. 223-256.

[50] Jenkins, J. and Savage, S. (1983), A theory for the rapid flow of identical smooth nearly elastic spherical particles, Journal of Fluid Mechanics, 130, pp. 187-202.

[51] Gunn, D.J. (1978), Transfer of heat or mass to particles in fixed and fluidized beds, International Journal of Heat and Mass Transfer, 21, pp. 467-476.

[52] Santos, M.L.D. (2005), Solid Fuels Combustion and Gasification, Marcel Dekker Inc.

[53] FLUENT 6 (2002), User's Guide, Fluent Incorporated, Centerra Resource Park, 10 Cavendish Court, Lebanon NH 03766.

[54] Kobayashi, H., Howard, J.B. and Sarofim, A.F. (1976), Coal devolatilization at high temperatures, in proceeding, 16th International Symposium on Combustion.

[55] Krukanont, P. and Prasertsan, S. (2004), Geographical distribution of biomass and potential sites of rubber wood fired power plants in Southern Thailand, Biomass and Bioenergy, 26, pp. 47-59.

[56] Pinto, F., Franco, C., André, R.N., Miranda, M., Gulyurtlu, I. and Cabrita, I. (2002). Co-gasification study of biomass mixed with plastic wastes, Fuel, 81, pp. 291-297.

[57] Schiffer, H.P. and Adlhoch, W. (1995), Co-gasification of used plastics at the HTW demonstration plant: results from R&D activities. Braunkohle, 47, pp. 19-25.

[58] Davison, R. (1997), Coprocessing waste with coal, IEA Coal Research.

[59] Choi, Y.C., Lee, J.G., Kim, J.H., Park, T.J. and Kim, J.H. (2007), High temperature airblown gasification of Korean anthracite and plastic waste mixture, Korean Journal of Chemical Engineering, 24 (4), pp. 706-710.

[60] Wang, L., Weller, V.L., Jones, D.D. and Hanna, M.A. (2008), Review contemporary issues in thermal gasification of biomass and its application to electricity and fuel production. Biomass and Bioenergy, 32, pp. 573-581.

[61] Waldheim, L. and Nilsson, T. (2001), Heating value of gases from biomass gasification, Report prepared for IEA Bioenergy Agreement-Thermal Gasification of Biomass, 20.

[62] Chalermsinsuwan, B., Gidaspow, D. and Piumsomboon, P. (2011), Two- and three-dimensional CFD modeling of Geldart A particles in a thin bubbling fluidized bed: Comparison of turbulence and dispersion coefficients, Chemical Engineering Journal, 171, pp. 301-313.

[63] Hoomans, B.P.B., Kuipers, J.A.M. and van Swaaij, W.P.M. (2000), Granular dynamics simulation of segregation phenomena in bubbling gas-fluidised beds, Powder Technology, 109, pp. 41-48.

[64] Morita, H., Yoshiba, F., Woudstra, N., Hemmes, K. and Spliethoff, H. (2004), Feasibility study of wood biomass gasification/molten carbonate fuel cell power system comparative characterization of fuel cell and gas turbine systems, Journal of Power Sources, 138, pp. 31-40.

[65] Hughes, W.E.M. and Larson, E.D. (1998). Effect of fuel moisture content on biomass-IGCC performance. Journal of Engineering for Gas Turbines and Power, 120, pp. 455-459.

[66] Xiao, R., Jin, B., Zhou, H., Zhong, Z. and Zhang. M. (2007), Air gasification of polypropylene plastic waste in fluidized bed gasifier, Energy Conversion and Management, 48, pp. 778-786.

[67] Aznar, M.P., Caballero, M.A., Sabcho, J.A. and Francés, E. (2006), Plastic waste elimination by co-gasification with coal and biomass in fluidized bed with air in pilot plant, Fuel Processing Technology, 87, pp. 409-420.

[68] García-Bacaicoa, P., Mastral, J.F., Ceamanos, J., Berrueco, C. and Serrano, C. (2008), Gasification of biomass/high density polyethylene mixtures in a downdraft gasifier, Bioresource Technology, 99, pp. 5485-5491.

[69] McKeen, T. and Pugsley, T. (2003), Simulation and experimental validation of a freely bubbling bed of FCC catalyst, Powder Technology, 129, pp. 139–152.

[70] van Wachem, B.G.M., Schouten, J.C. and van den Bleek, C.M. (2001), Comparative analysis of CFD models of dense gas-solid systems, American Institute of Chemical Engineers Journal, 47, pp. 1035–1051.

[71] Benyahia, S., Syamlal, M. and O'Brien, T.J. (2005), Evaluation of boundary conditions used to model dilute, turbulent gas/solids flows in a pipe, Powder Technology, 156, pp. 62–72.

[72] Almuttahar, A. and Taghipour, F. (2008), Computational fluid dynamics of high density circulating fluidized bed riser: study of modeling parameters, Powder Technology, 185, pp. 11–23.

[73] FLUENT 6.3 (2006), "Tutorial Guide", Available online: http://cdlab2.fluid.tuwien.ac.at/LEHRE/TURB/Fluent.Inc/fluent6.3.26/help/html/tg/main_pre.htm

[74] Syamlal, M., Rogers, W. and O'Brien, T. J. (1993), MFIX Documentation: Volume 1, Theory Guide. National Technical Information Service, Springfield, VA.

[75] Yang, W.C. (1986), Particle segregation in gas-fluidized beds, Encyclopedia of Fluid Mechanics, 4, pp. 817-852.

[76] Singh, R.K., Suryanarayana, A. and Roy, G.K. (1999), Prediction of bed expansion ratio for gas-solid fluidization in cylindrical and non-cylindrical beds, Journal of the Institution of Engineers (India), Chemical Engineering Division, 79, pp. 51-54.

[77] Gimbun, J., Chuah, T.G., Fakhru'l-Razi, A., Thomas, S.Y. (2005), The influence of temperature and inlet velocity on cyclone pressure drop: a CFD study, Chemical Engineering and Processing, 44, pp. 7-12.

APPENDIXES

APPENDIX A
SCREW FEEDING SYSTEM CALIBRATIONS

From the training in the use of the bubbling fluidized bed gasifier system, it was found that the bulk density of feeding stock influenced the screw feeding rate. Therefore, the screw feeding meter needed to be calibrated before running on the gasification experiment part. The fuels used for these calibrations divided into two main groups. The first group was the rubber woodchip which had moisture content as received (36.69%) and the other group was the rubber woodchip which was controlled to have moisture content at 27%. There were two samples in each group, and each sample was test 5 times by varying the screw feeding rate (Hz) obtained from the screw feeding meter. Raw data of screw feeding meter calibration tests for first group of sample and second group of sample are presented in Table A-1 and A-2, respectively.

The calibration factor for each sample resulted from graph plotting between the screw feeding rate obtained from calculation (kg/hr) and that from the screw feeding rate meter (Hz), as shown in Figures A-1 to A-4. Then, all these obtained calibration factors are plotted versus the percent of SPB in the fuel mixture for using in gasification experiments. Theses graphs of calibration factor for these two groups of samples are displayed in Figures A-5 and A-6, respectively.

Table A-1 Raw data of screw feeding meter calibration tests for first group of sample.

Samples	Screw feeding rate (Hz)	Weight (kg)	Time (min)	Screw feeding rate (kg/hr)
0% SPB, M.C.= 36.69%	25.0	10	13.30	46.0
	20.0	10	17.30	35.2
	15.1	10	22.00	27.3
	10.0	5	16.00	18.8
20% SPB, M.C.=32.04%	40.0	5	4.55	61.0
	35.0	5	5.40	52.9
	30.1	5	6.40	45.0
	25.0	5	7.50	38.3
	20.0	5	10.00	30.0

Table A-2 Raw data of screw feeding meter calibration tests for second group of sample.

Samples	Screw feeding rate (Hz)	Weight (kg)	Time (min)	Screw feeding rate (kg/hr)
10% SPB, M.C.=24.3%	40.0	5	3.51	77.9
	35.0	5	4.21	69.0
	30.1	5	5.16	57.0
	25.0	5	6.30	46.2
	20.0	5	8.00	37.5
20% SPB, M.C.=21.6%	40.0	5	4.20	69.2
	35.0	5	4.52	31.6
	30.0	5	5.41	52.8
	25.0	5	6.53	43.6
	20.0	5	8.56	33.6

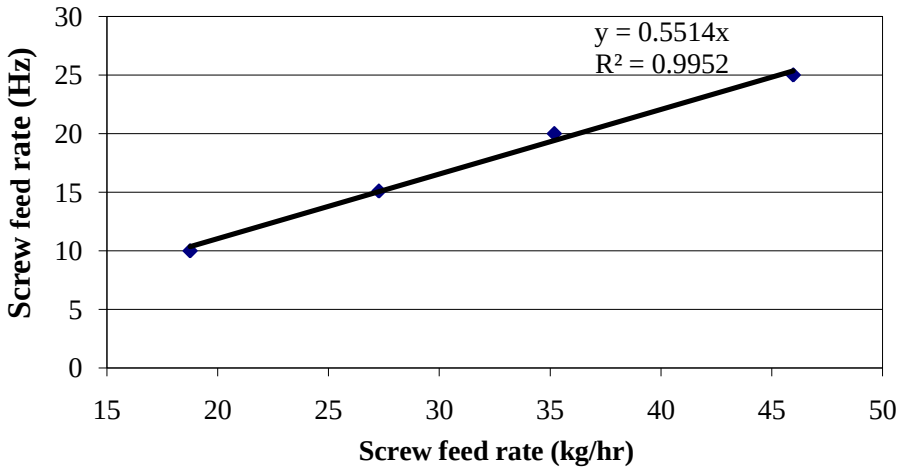

Figure A-1 Calibration graph for sample of 0% SPB, M.C. = 36.69%.

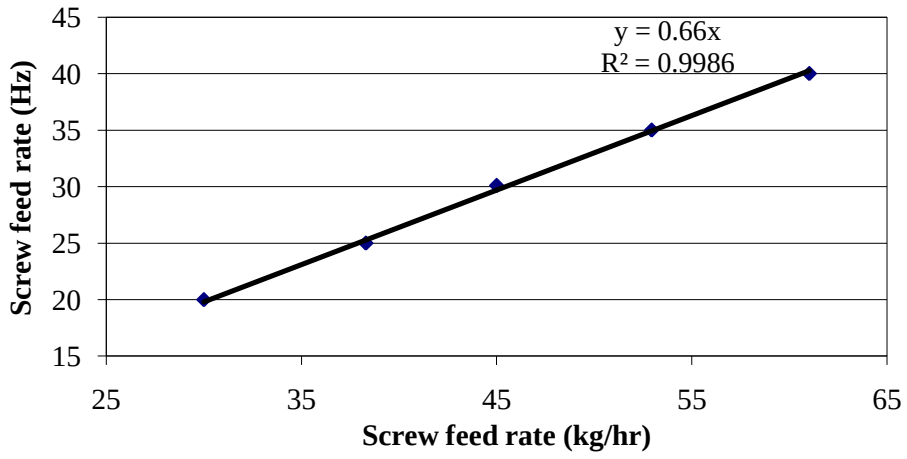

Figure A-2 Calibration graph for sample of 20% SPB, M.C. = 32.04%.

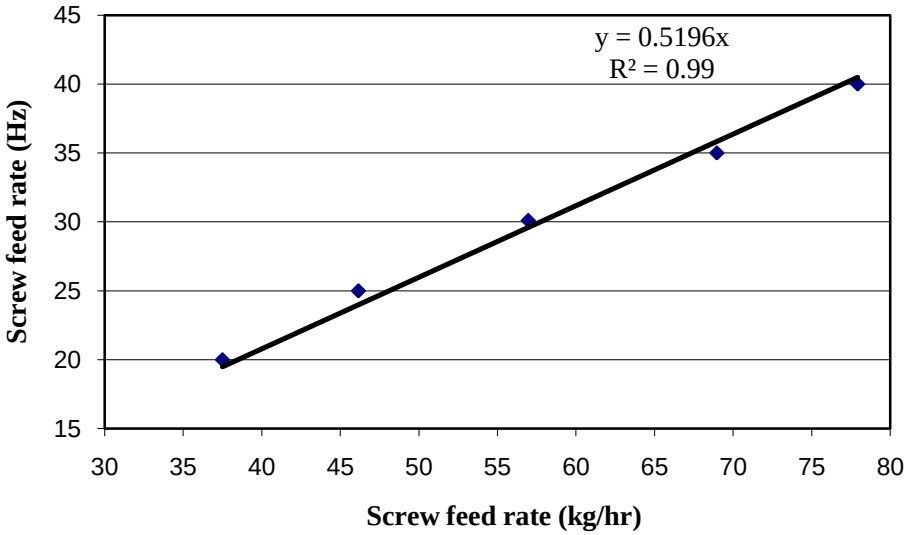

Figure A-3 Calibration graph for sample of 10% SPB, M.C. = 24.3%.

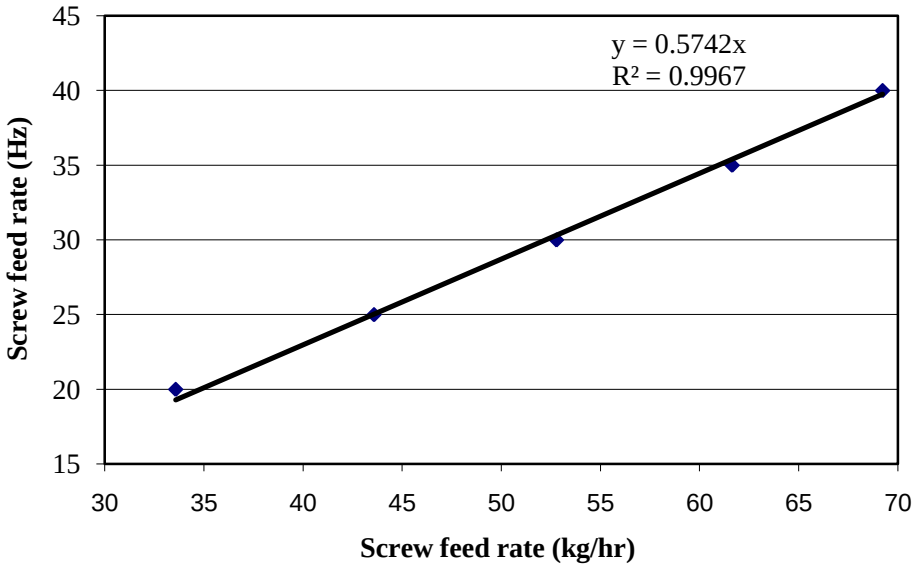

Figure A-4 Calibration graph for sample of 20% SPB, M.C. = 21.6%.

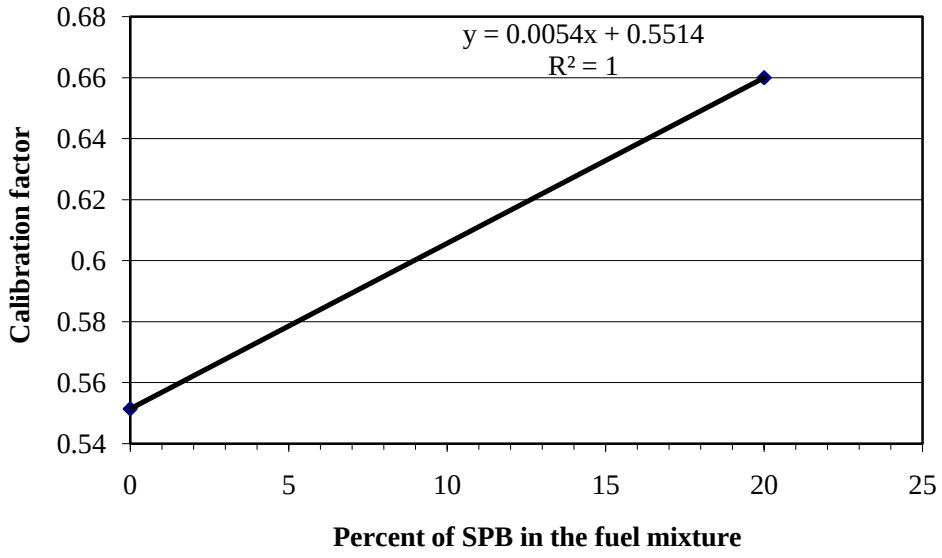

Figure A-5 Graph of calibration factor for samples in the group of rubber woodchips with the received moisture content.

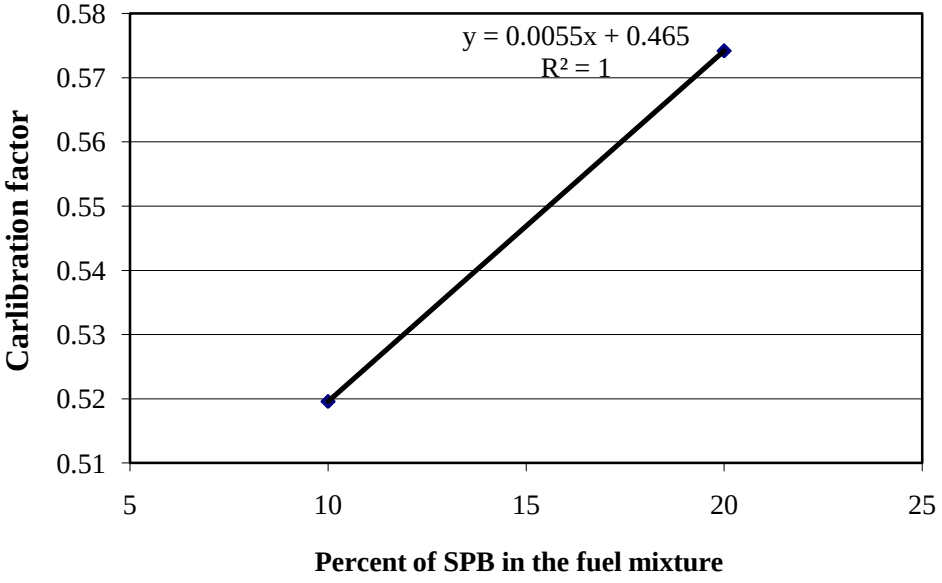

Figure A-6 Graph of calibration factor for samples in the group of rubber woodchips for which the moisture content was controlled.

APPENDIX B

SEVERAL VARIABLE STUDIES ON SIMPLIFIED MODEL SIMULATIONS

The simplified air distributor model simulation under cold flow (ambient temperature and non-reactive considered) conditions had been run through the commercial CFD package by varying the reactor models, input parameters, and optional model selection for eight cases, as shown in Table B-1.

The reactor model 1 was used in the first six cases (Run Nos. 1 – 6) while the reactor models 2 and 3 were used in cases seven and eight (Run Nos. 7 and 8) respectively. The reactor model 1 was created without the air distributor (air injector) at the lower part of the model, but the uniform flow of air at a superficial velocity was introduced through the bottom phase instead as shown in Figure B-1a. The reactor model 2 and 3 were create with the same simplification of air distributors, but used a different set of boundary condition. In reactor model 2, the nozzles of air distributor were designated as "Velocity Inlets" in FLUENT while the other parts of bottom phase were designed as "Wall" as shown in Figure B-1b. In reactor model 3, all parts of bottom phase were designed as "Velocity Inlets" with the same flow rate at a superficial velocity as shown in Figure B-1c.

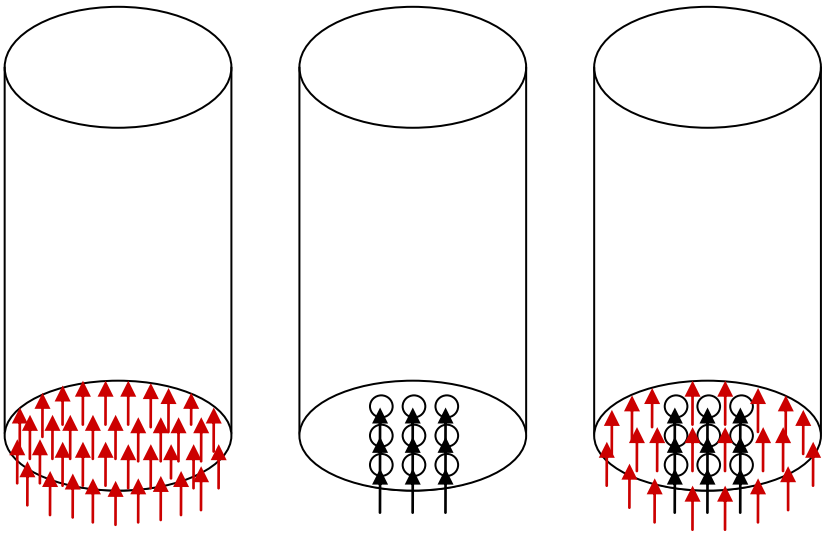

a. b. c.

Figure B-1 The simplified air distributor models (a.) Reactor Model 1, (b.) Reactor Model 2, (c.) Reactor Model 3

Table B-1 Details of the eight cases of the simplified air distributor model.

Run No.	1	2	3	4	5	6	7	8
Reactor Model	1	1	1	1	1	1	2	3
Conditions								
Flow type	Laminar	Laminar	Laminar	Laminar	Turbulent	Turbulent	Laminar	Laminar
Unsteady	Yes	Yes	Yes	Yes	Yes	Yes	Yes	Yes
Eulerian	3 Phases	3 Phases	2 Phases	2 Phases	2 Phases	3 Phases	3 Phases	3 Phases
Phase 1 (Air)								
Density (kg/m^3)	1.225	1.225	1.225	1.225	1.225	1.225	1.225	1.225
Viscosity (kg/m-s)	1.7894 e-05	1.7894 e-05	1.7894 e-05	1.7894 e-05	1.7894 e-05	1.7894 e-05	1.7894 e-05	1.7894 e-05
Velocity inlet (m/s)								
- air injection	-	-	-	-	-	-	1.466	1.466
- Umf	0.712	0.19	0.19	0.19	0.19	0.19	-	0.19
Phase 2 (Silica sand)								
Density (kg/m^3)	2647	2647	2647	2647	2647	2647	2647	2647
Granular	No	Yes	Yes	Yes	Yes	Yes	Yes	Yes
Viscosity (kg/m-s)	1 e-05	1 e-05	1 e-05	1 e-05	1 e-05	1 e-05	1 e-05	1 e-05
Diameter (mm)	0.352	0.352	0.352	0.352	0.352	0.352	0.352	0.352
Volume fraction	0.598	0.538	0.538	0.538	0.538	0.538	0.538	0.538
Packing Limit	-	0.63	0.63	0.63	0.63	0.63	0.63	0.63
Phase 3 (Biomass)								
Density (kg/m^3)	900	700	-	-	-	700	700	700
Granular	No	No	-	-	-	No	No	No
Diameter (mm)	40	2	-	-	-	2	2	2
Volume fraction	-	-	-	-	-	-	-	-
Velocity inlet (m/s)	0	0	-	-	-	0	0	0
Phase Interaction								
Drag Coefficient of								
- Silica sand and Air	Schiller-Naumann	Symmetric	Symmetric	Schiller-Naumann	Schiller-Naumann	Gidaspow	Schiller-Naumann	Schiller-Naumann
- Biomass and Air	Schiller-Naumann	Symmetric	-	-	-	Schiller-Naumann	Schiller-Naumann	Schiller-Naumann
- Biomass and Silica sand	Schiller-Naumann	Gidaspow	-	-	-	Gidaspow	Schiller-Naumann	Schiller-Naumann
Collisions								
Restitution Coefficient of Silica sand &Silica sand	0.9	0.9	0.9	0.9	0.9	0.9	0.9	0.9
Pressure (Pascal)	101325	101325	101325	101325	101325	101325	101325	101325
Gravity (m/s^2)	-9.81	-9.81	-9.81	-9.81	-9.81	-9.81	-9.81	-9.81

The simulation results are presented in seven sections as follows:

B.1 The Results of Run No. 1

After the reactor model 1 was created and meshed by GAMBIT, Run No. 1 was carried out by FLUENT for fifteen minutes. The simulated results were consist of the contour of silica sand volume fraction, the vectors of silica sand velocity, and the vectors of air velocity as presented in Figures B-2 to B-4.

It was acceptable that an introduced air had not been released through the feeding area, but had moved upward to the top of the reactor model. The air velocity was high in bed zone, but lower and uniform after passed through the bed surface as shown in Figure B-2. Anyway, there were some problems presented in this case. The bed surface was not stable, it moved up higher and higher with the time, as shown in Figure B-3. The vectors of silica sand velocity were not make sense as there were some high velocities moving down on the bed surface as shown in Figure B-4 which meant that there had another forces, outside the gravity force, air inlet force, and interaction force between silica sand, reacted to the silica sand in the bed. Therefore, the input conditions were changed in next case.

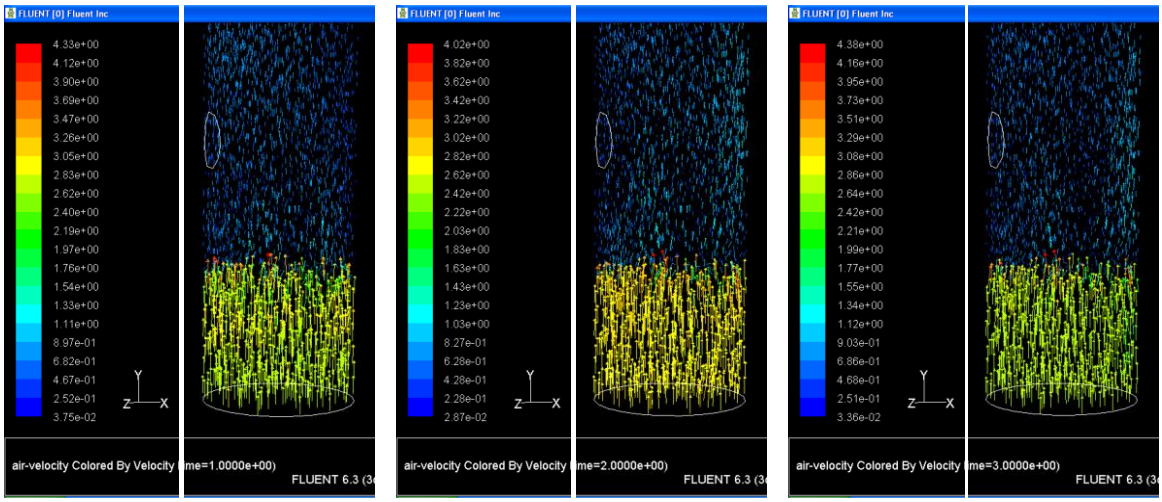

1 s 2 s 3 s

Figure B-2 Air velocity colored by velocity magnitude (m/s) at time = 1 to 3 s.

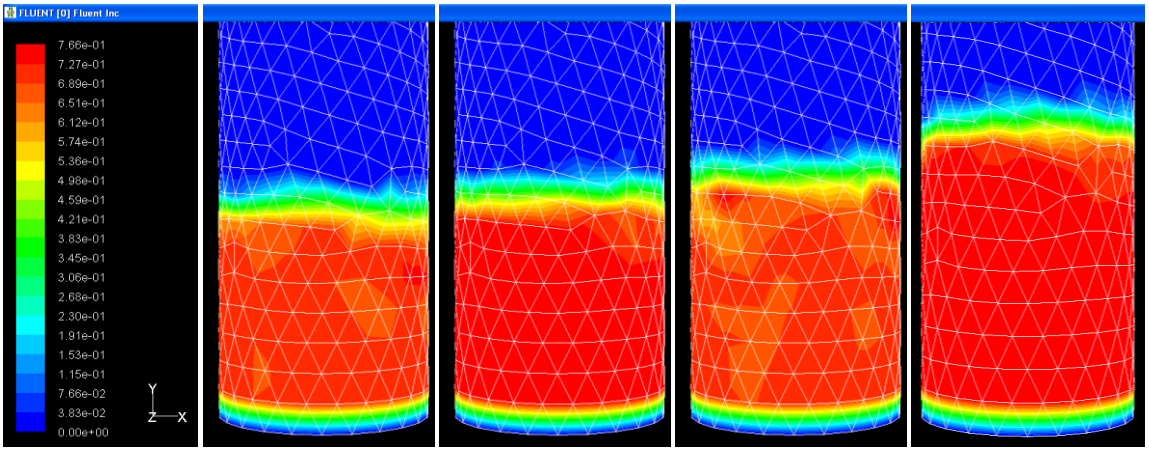

1 minute 5 minute 10 minute 15 minute

Figure B-3 Contours of silica sand volume fraction at time = 1, 5, 10, 15 minute.

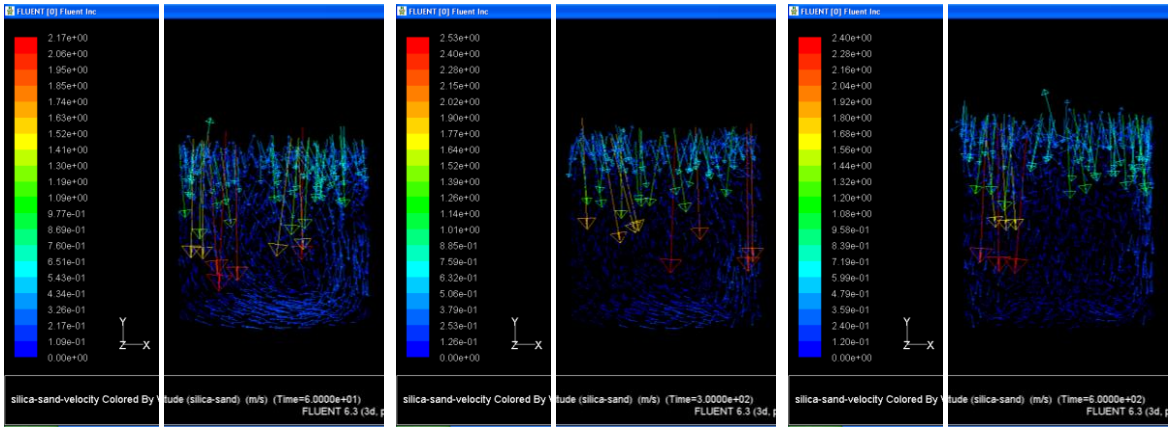

1 minute 5 minute 10 minute

Figure B-4 Silica sand velocity colored by velocity magnitude (m/s) at time = 1, 5, 10 minute.

B.2 The Results of Run Nos. 2 and 3

Run Nos. 2 and 3 used the same reactor model as did Run No. 1, but used different conditions to simulate that model. As Run No. 1 assumed that silica sand was not a granular phase, but it was in Run No. 2 and Run No. 3, and the drag coefficient of phase interactions were also changed as shown in Table B-1. The difference of Run No. 2 and Run No. 3 was the input phase number of multiphase model. Run No. 2 was set as an Eulerian three phases, including of air phase, silica sand phase, and biomass phase, while Run No. 3 was set as an Eulerian two phases, without biomass phase. After the models

were run by FLUENT, the simulated results from Run No. 2 were also compared with that from Run No. 3 to study the effect of input phase number on the simulated results.

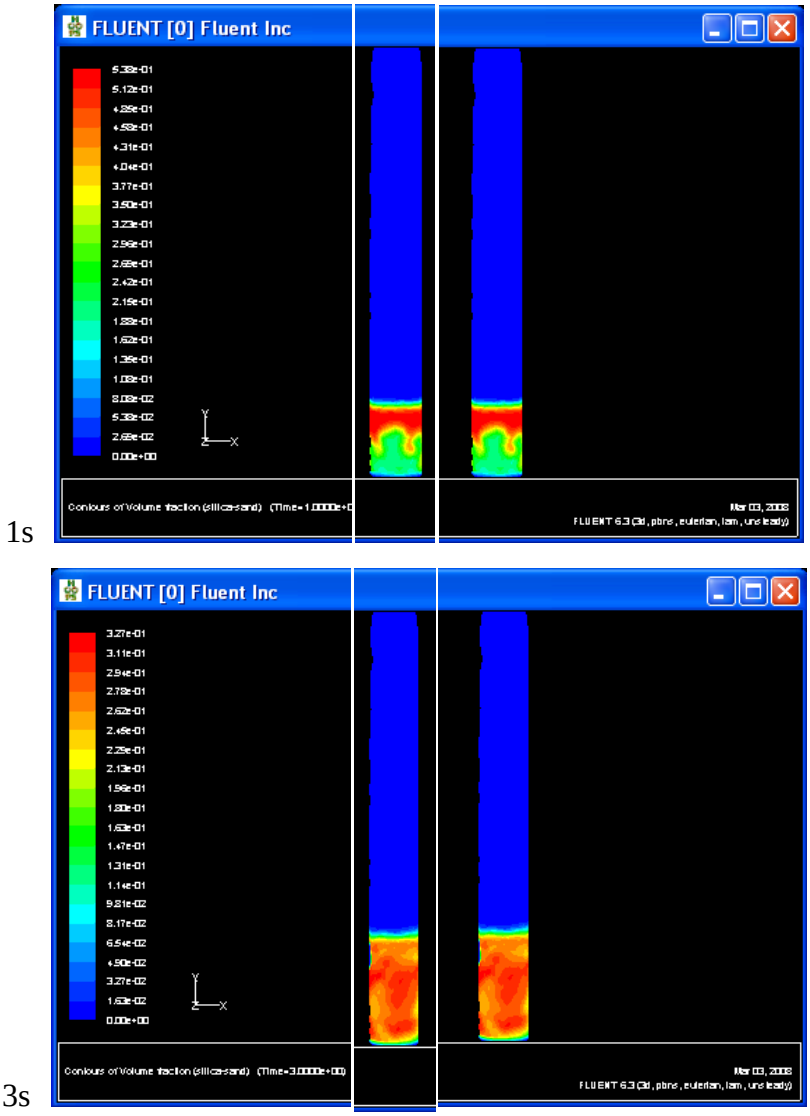

Run No. 2 Run No. 3

Figure B-5 Comparison of the contours of silica sand volume fractions resulting from Run Nos. 2 and 3 at time = 1 and 3 s.

Whenever the biomass phase was designed as “Velocity Inlets” with a “Zero” flow rate, the simulated results of the Eulerian three phases were the same as that of the Eulerian two phase, as shown in Figure B-5.

Figure B-5 also showed the problem of these two cases, as the bed surface was not stable. It moved up higher and higher with time, just as it in Run No. 1, but took a shorter time than did Run No. 1. So, the next case was run.

B.3 The Results of Run No. 4

Since the biomass phase has not affected the simulated results, as presented in Section B.2, so the Eulerian two phases was used in this case as Run No. 4. The drag coefficient of phase interaction was studied by comparing the simulated results of Run No. 3 with Run No. 4 as shown in Figure B-6. Run No. 3 used model of Symmetric for the drag coefficient between two phases of silica sand and air while Run No. 4 used model of Schiller and Naumann.

Using a different model for the drag coefficient of phase interaction affected the simulated results, as shown in Figure B-6. The model of Schiller and Naumann in Run No. 4 took longer time than the model of Symmetric in Run No. 3 to move the bed surface upward.

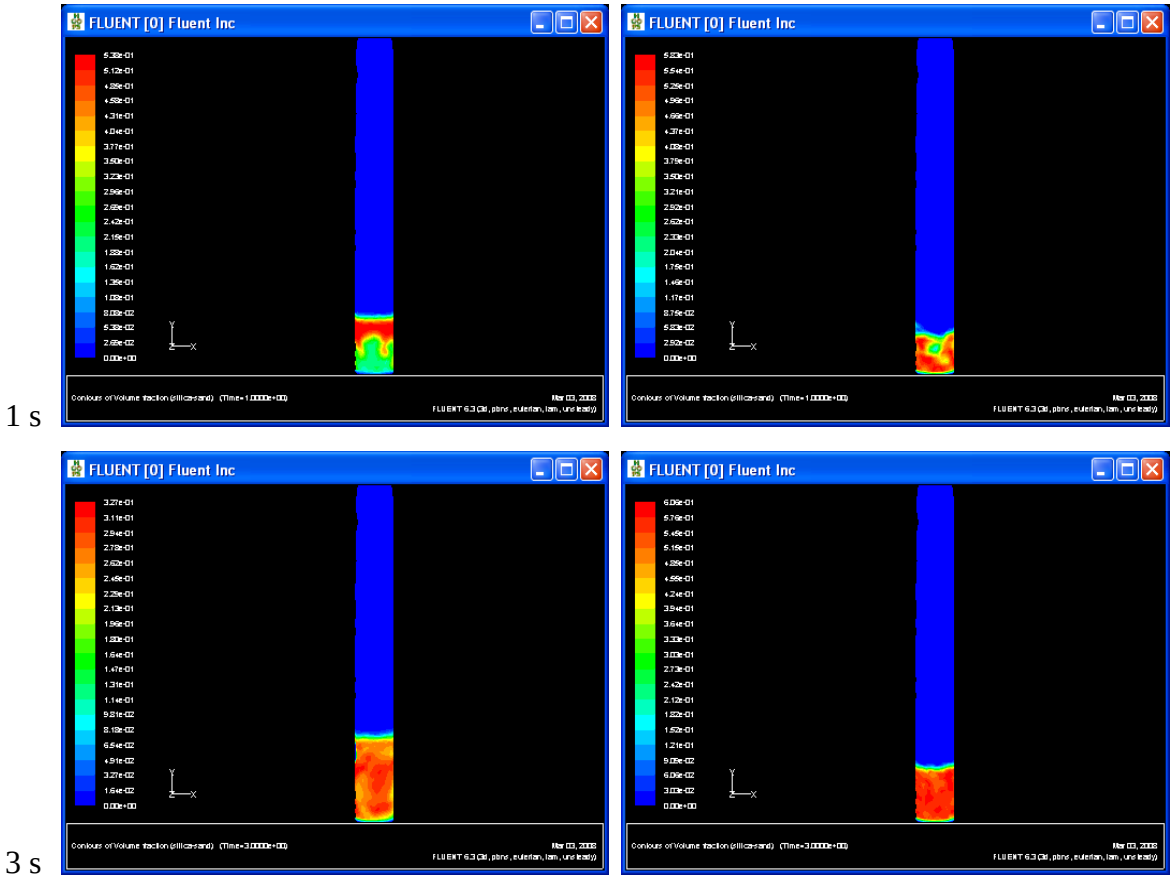

Figure B-6 Comparison of the contours of silica sand volume fractions resulting from Run Nos. 3 and 4 at Time = 1 and 3 s.

Both of these cases still could not solve the problem of the bed surface moving up, thus the next case was tested.

B.4 The Results of Run No. 5

After Run Nos. 1 to 4 were tested with the "Laminar" flow type, and since their simulated results were not acceptable, the "Turbulent" flow type was tested instead in Run No. 5. Therefore, all the input conditions in this case were the same as in Run No. 4, except for the type of flow.

The simulated results, as seen in Figures B-7 to B-9, show that the "Turbulent" flow type had changed the pattern of contours of silica sand volume fraction, and the vector velocity of air and silica sand to be more turbulent when compared to that from the "Laminar" flow type. The bed surface moved up very quickly, as shown in Figure B-7.

The vector velocity of air was high in the bed, and was lower and uniform after passing through the bed surface, as shown in Figure B-8. Most of the vector velocity of silica sand moved horizontally as presented in Figure B-9. After the model was run for a few minutes, all silica sand particles were dispersed out off the reactor model.

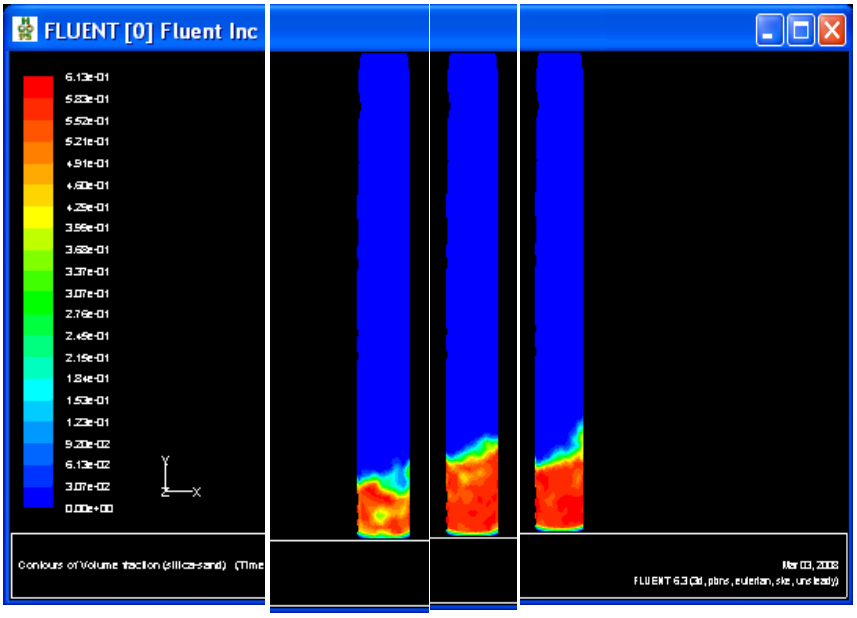

1 s 2 s 3 s

Figure B-7 Contours of silica sand volume fractions at time = 1 to 3 s.

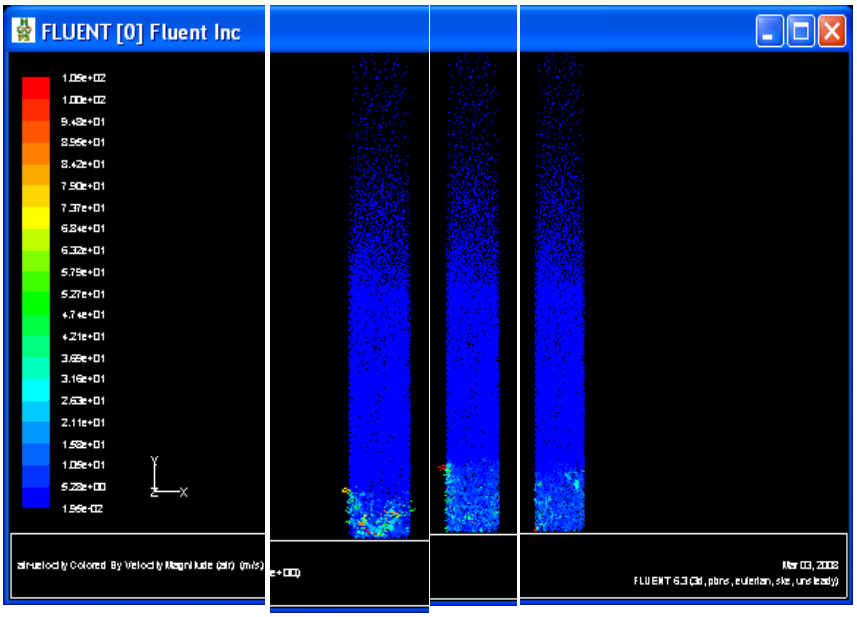

1 s 2 s 3 s

Figure B-8 Air velocity colored by velocity magnitude (m/s) at time = 1 to 3 s.

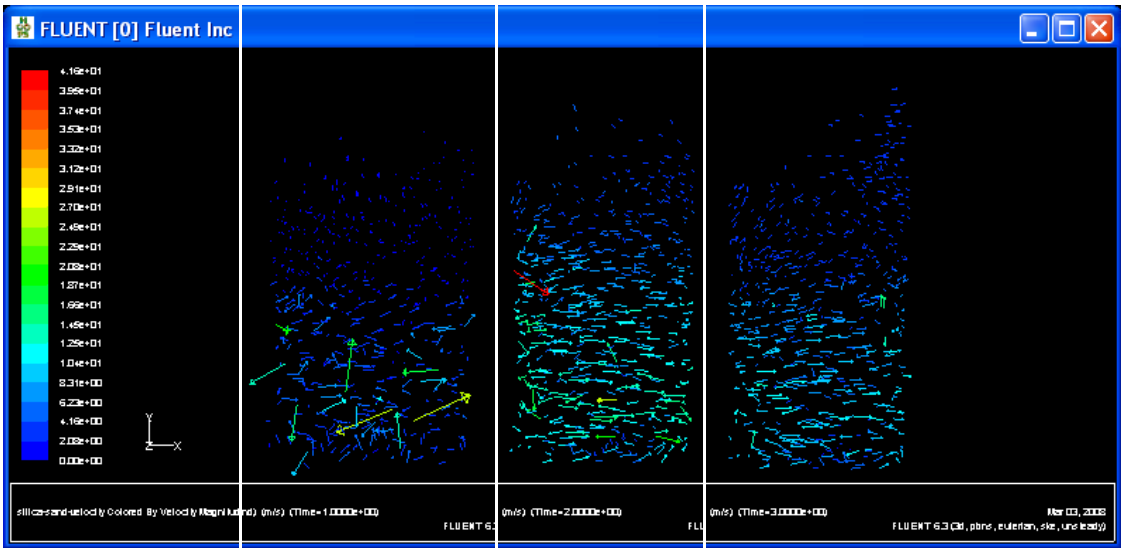

1 s 2 s 3 s

Figure B-9 Silica sand velocity colored by velocity magnitude (m/s) at time = 1 to 3 s.

Therefore, this case was still unacceptable and needed to be tested with different conditions.

B.5 The Results of Run No. 6

The “Turbulent” flow type was still handled in Run No. 6 and other input conditions were the same as in Run No.5, except that the multiphase condition in this case was an Eulerian three phases. Thus the drag coefficients of phase interaction between biomass phase and air phase and between biomass phase and silica sand were introduced into the model. The model of Gidaspow was assumed in cases of fluid-solid flow in this case.

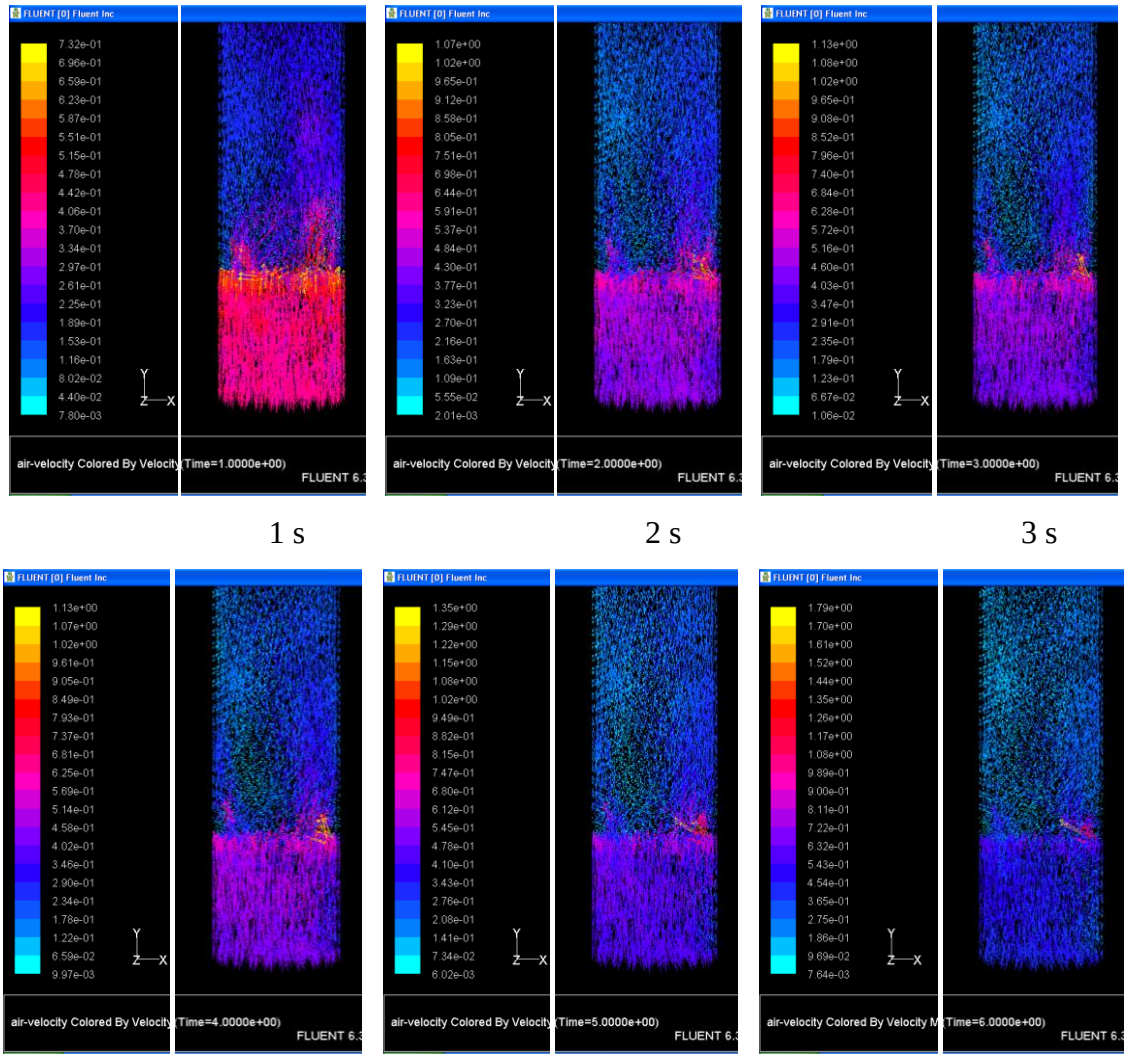

Figure B-10 Air velocity colored by velocity magnitude (m/s) at time = 1 to 6 s.

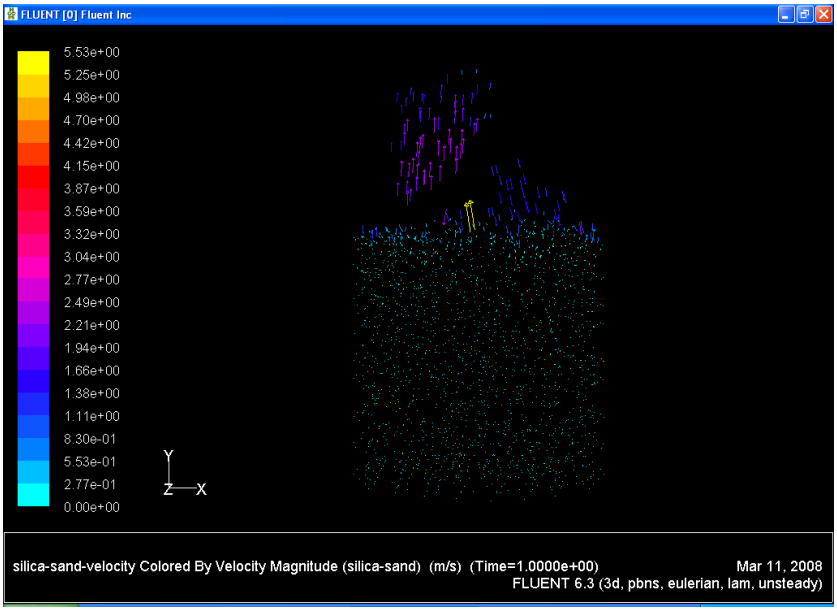

Figure B-11 Silica sand velocity colored by velocity magnitude (m/s) at time = 1 s.

The appearances of the vectors of the air and silica sand velocities are presented in Figures B-10 and B-11, respectively. Air and silica sand moved upward with high velocity in the bed and spouted like a fountain on the bed surface. Non-uniform vectors of air velocity occurred after passed through the bed surface as shown in Figure B-10. All silica sand particles were dispersed out off the reactor model after the model was run for a few minutes as same as it happened in Run No. 5.

Therefore, changing the type of flow had not been the right way to solve the problem, as seen in the simulated results of Run Nos. 5 and 6.

B.6 The Results of Run No. 7

An assumption of the reactor model changing was used in this case. To simplify the air distributors in reactor model 1, the uniform air flow was introduced through the bottom phase of the model with without any air injectors as presented in Figure B-1a, but in reactor model 2, which was used in Run No. 7, the nozzles of air distributor were created and designated as “Velocity Inlets” while the other parts of bottom phase were designed as “Wall” as shown in Figure B-1b. “Laminar” flow type and Eulerian three phases were used in this case.

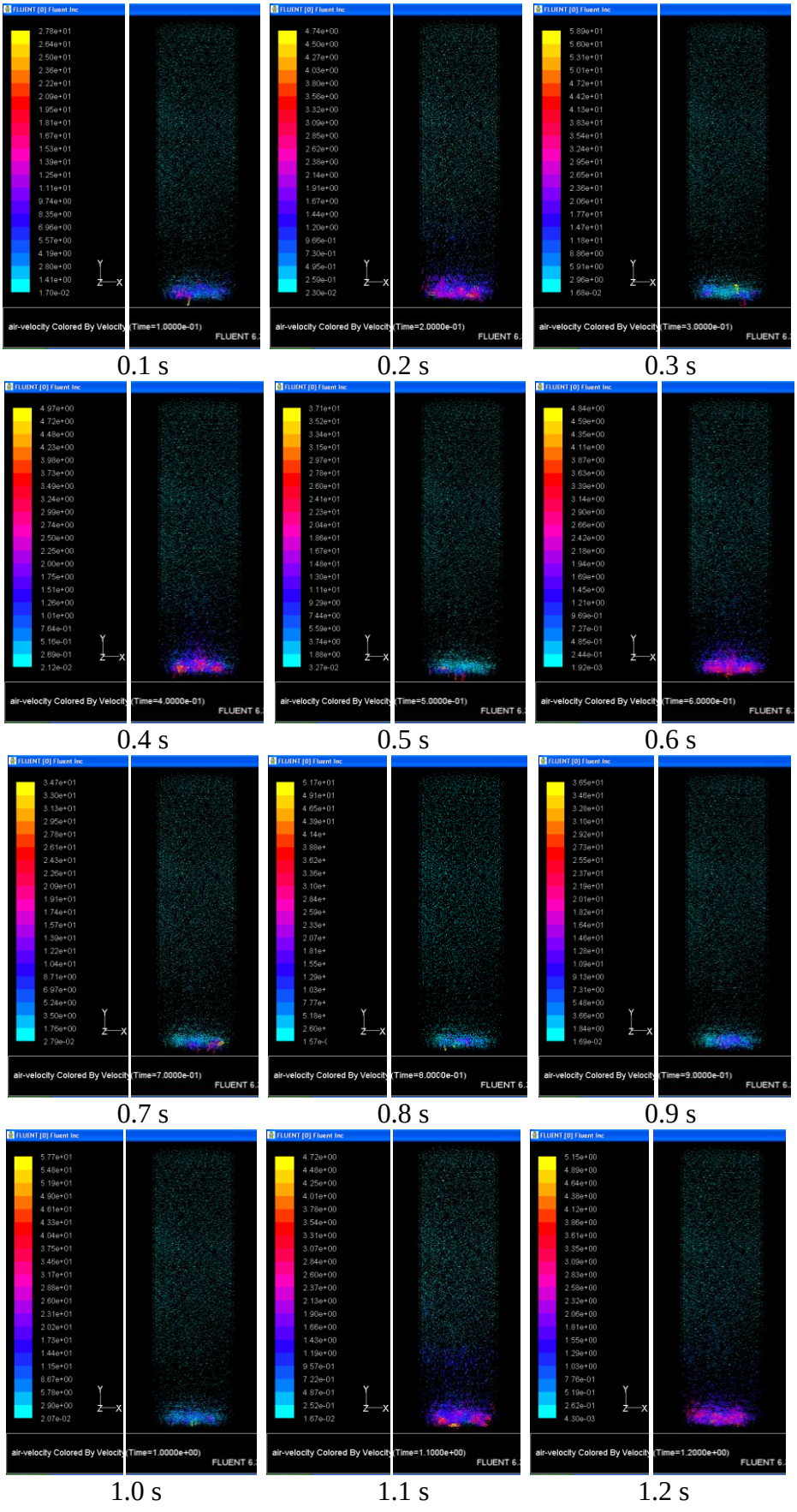

Figure B-12 Air velocity colored by velocity magnitude (m/s) at time = 0.1 to 1.2 s.

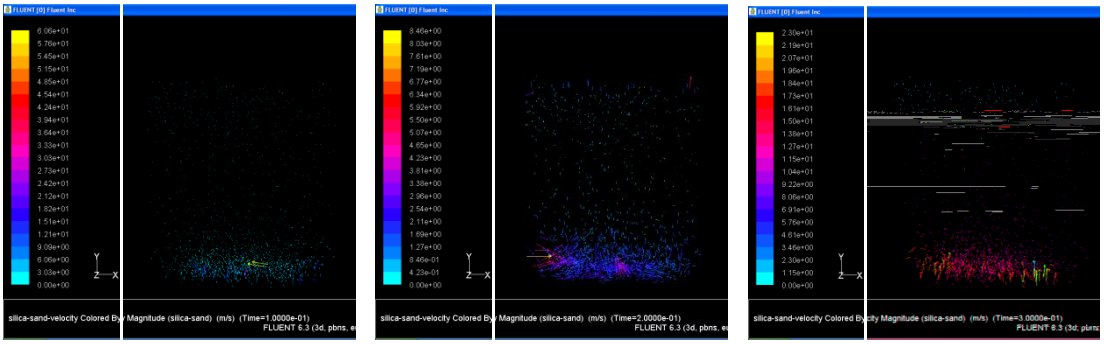

0.1 s 0.2 s 0.3 s

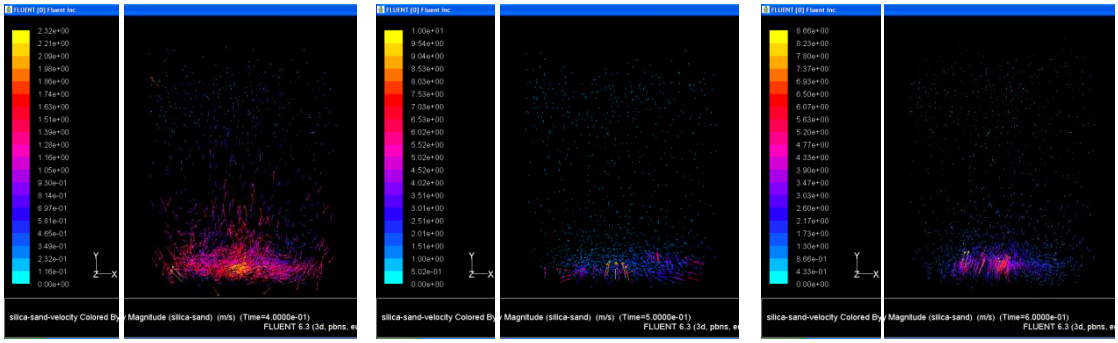

0.4 s 0.5 s 0.6 s

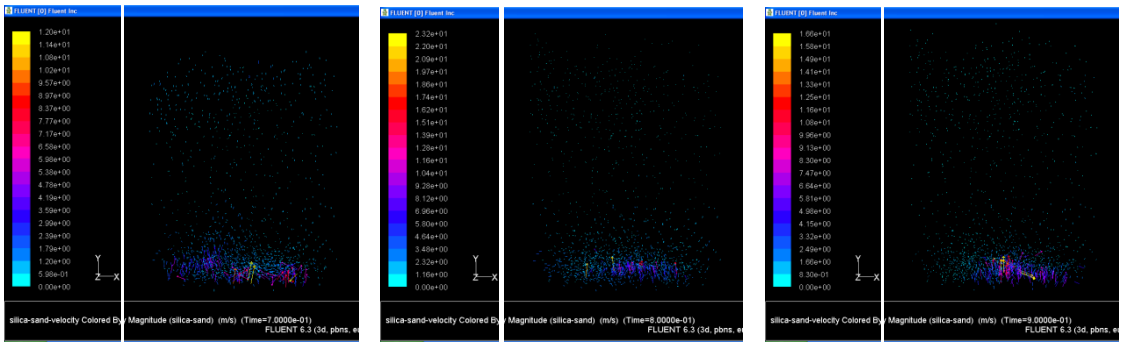

0.7 s 0.8 s 0.9 s

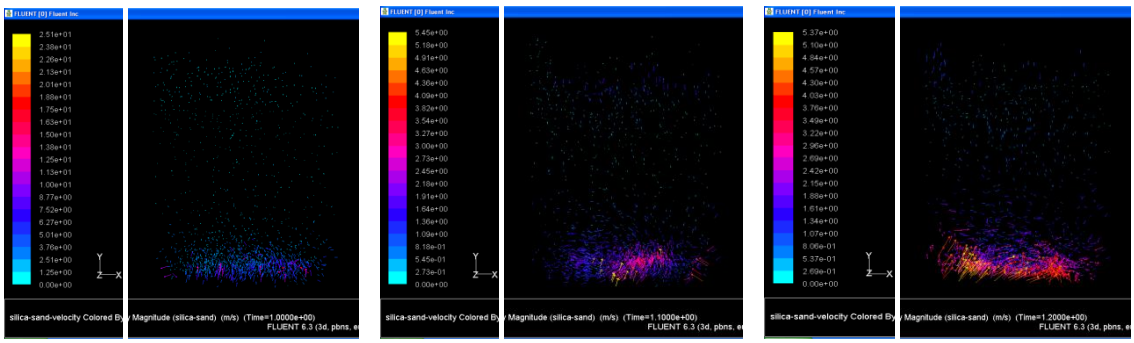

1.0 s 1.1 s 1.2 s

Figure B-13 Silica sand velocity colored by velocity magnitude (m/s) at time = 0.1 to 1.2 s.

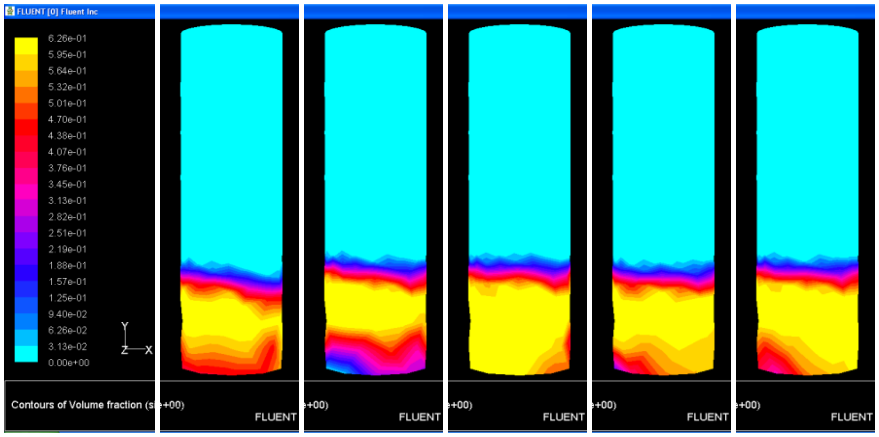

1 s 2 s 3 s 4 s 5 s

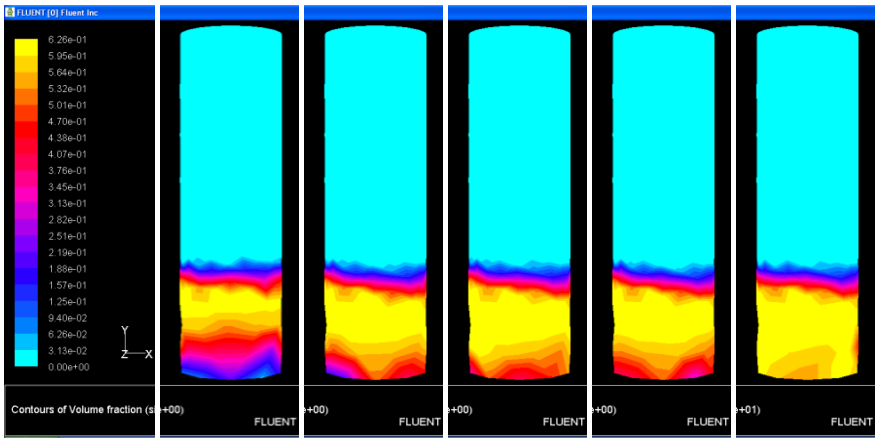

6 s 7 s 8 s 9 s 10 s

Figure B-14 Contours of silica sand volume fraction at time = 1 to 10 s.

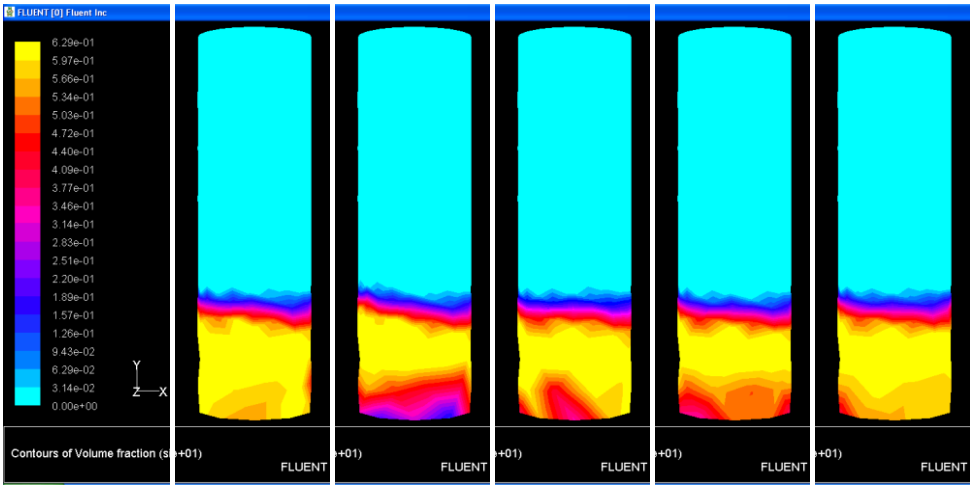

10 s 20 s 30 s 40 s 50 s

Figure B-15 Contours of silica sand volume fraction at time = 10 to 50 s.

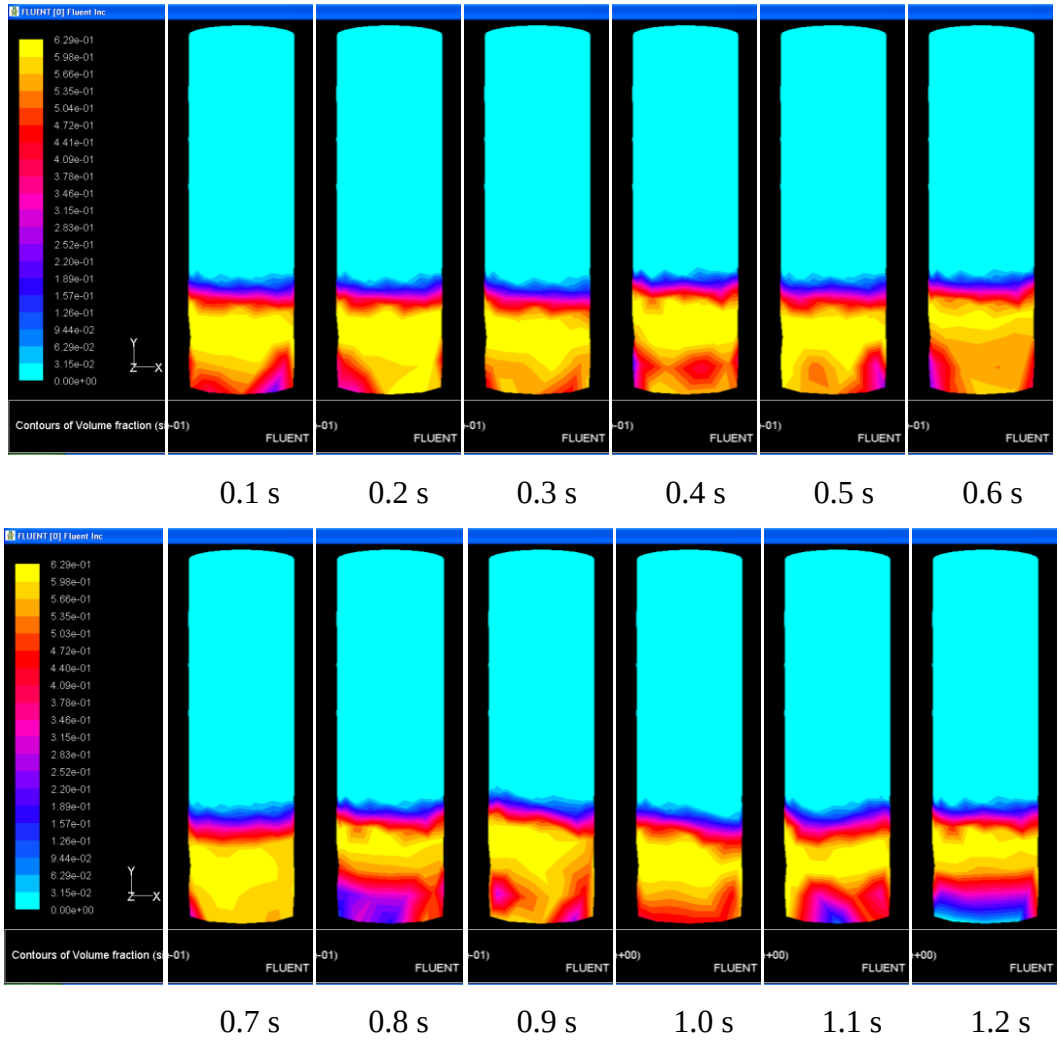

Figure B-16 Contours of silica sand volume fraction at time = 0.1 to 1.2 s.

B.7 The Results of Run No. 8

In this case, the reactor model was changed, from reactor model 2 to 3, in terms of the boundary conditions of the bottom phase. All parts of the bottom phase were designed as “Velocity Inlets” with the same flow rate at a superficial velocity, as shown in Figure B-1c, to check the effect of the boundary condition on the simulated results by comparison between Run Nod. 7 and 8.

The simulated results of Run No. 8 were the same those of Run No. 7, as seen in Figures B-17 to B-21, unless the bed moved up from the bottom phase for a little bit, as clearly shown in Figures B-19 to B-21.

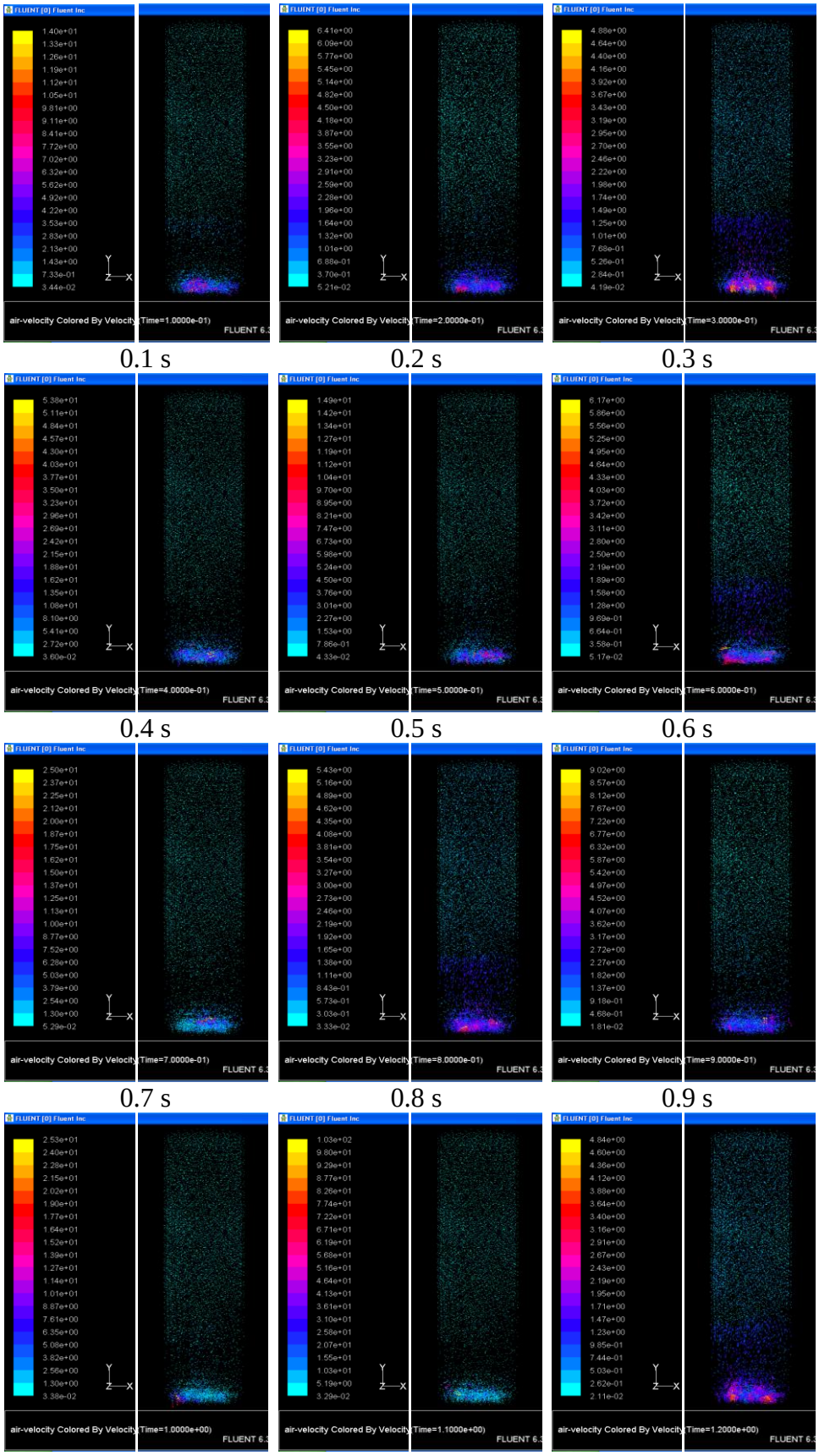

Figure B-17 Air velocity colored by velocity magnitude (m/s) at time = 0.1 to 1.2 s.

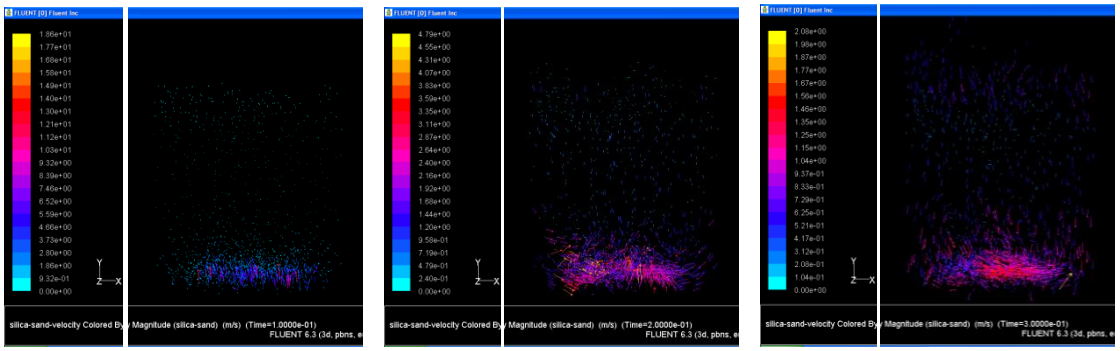

0.1 s 0.2 s 0.3 s

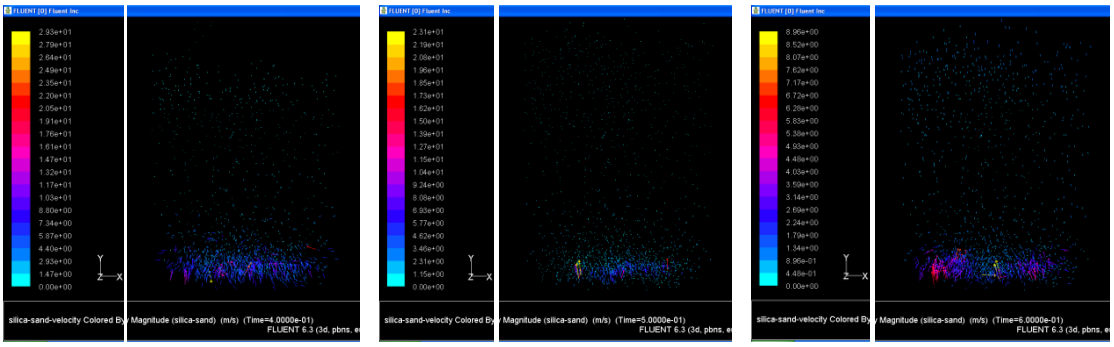

0.4 s 0.5 s 0.6 s

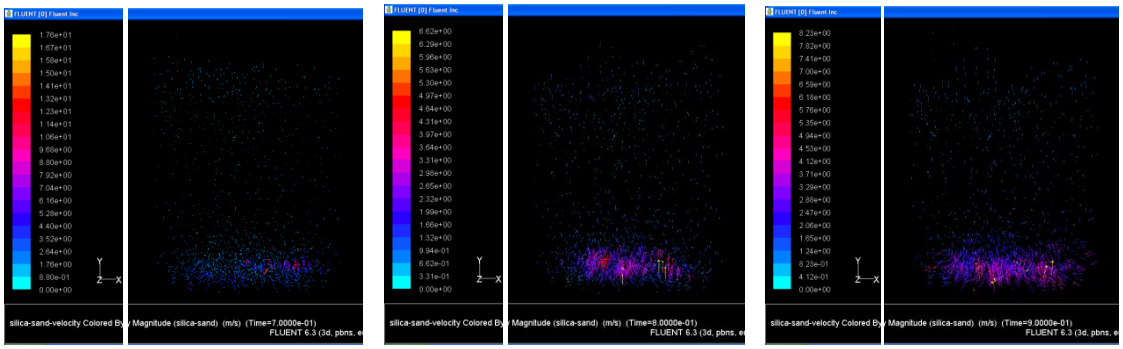

0.7 s 0.8 s 0.9 s

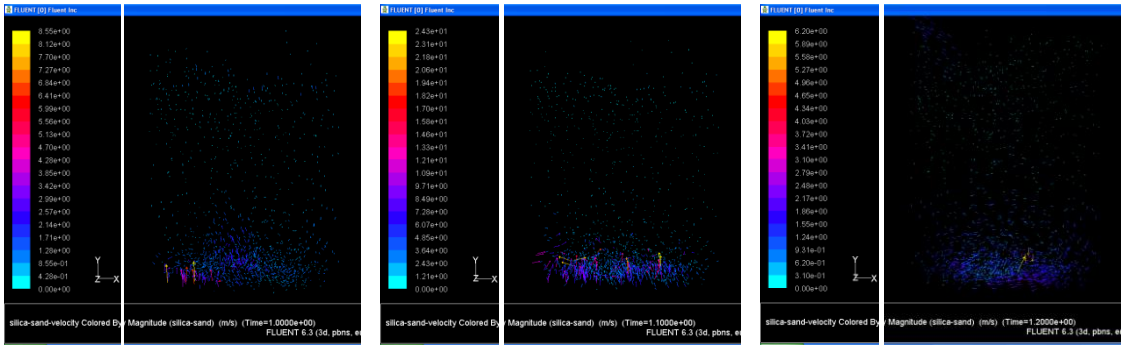

1.0 s 1.1 s 1.2 s

Figure B-18 Silica sand velocity colored by velocity magnitude (m/s) at time = 0.1 to 1.2 s.

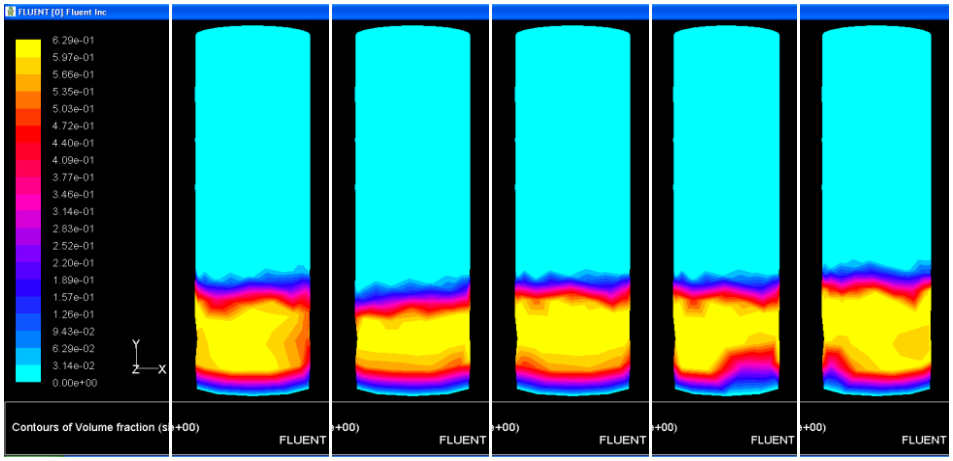

1 s 2 s 3 s 4 s 5 s

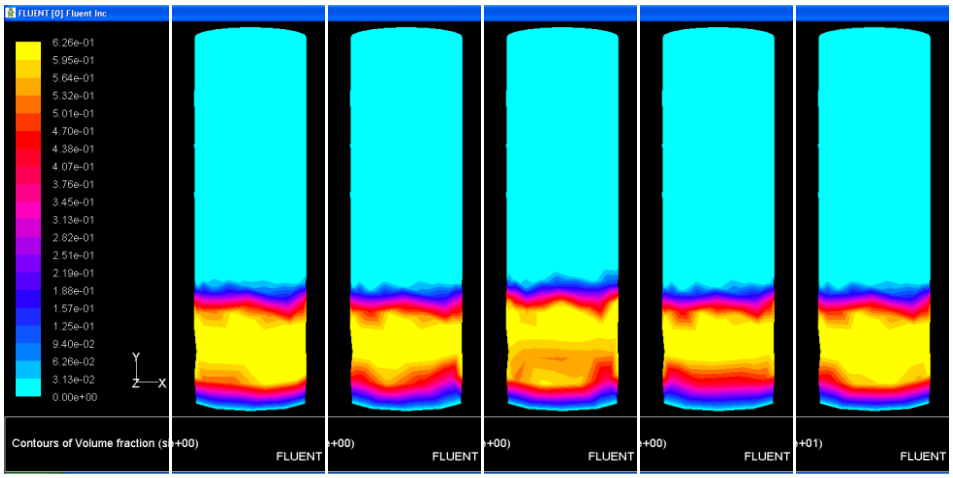

6 s 7 s 8 s 9 s 10 s

Figure B-19 Contours of silica sand volume fraction at time = 1 to 10 s.

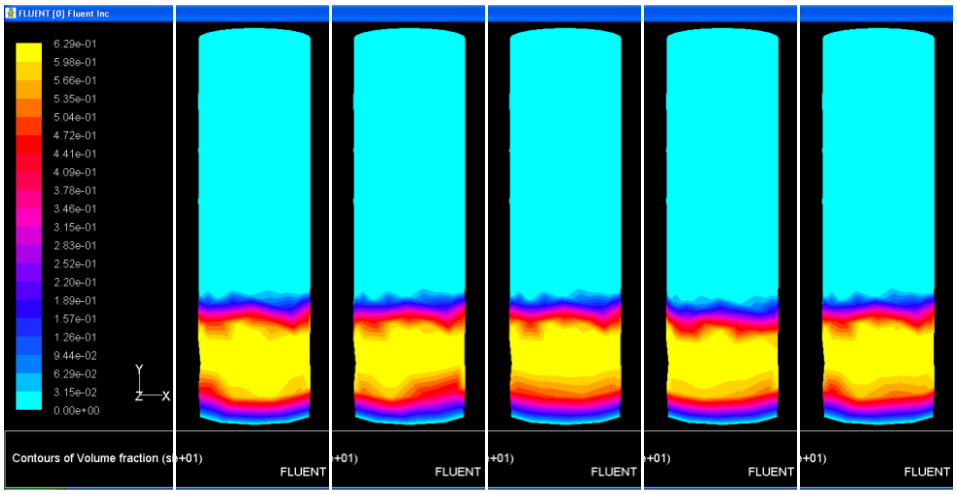

10 s 20 s 30 s 40 s 50 s

Figure B-20 Contours of silica sand volume fraction at time = 10 to 50 s.

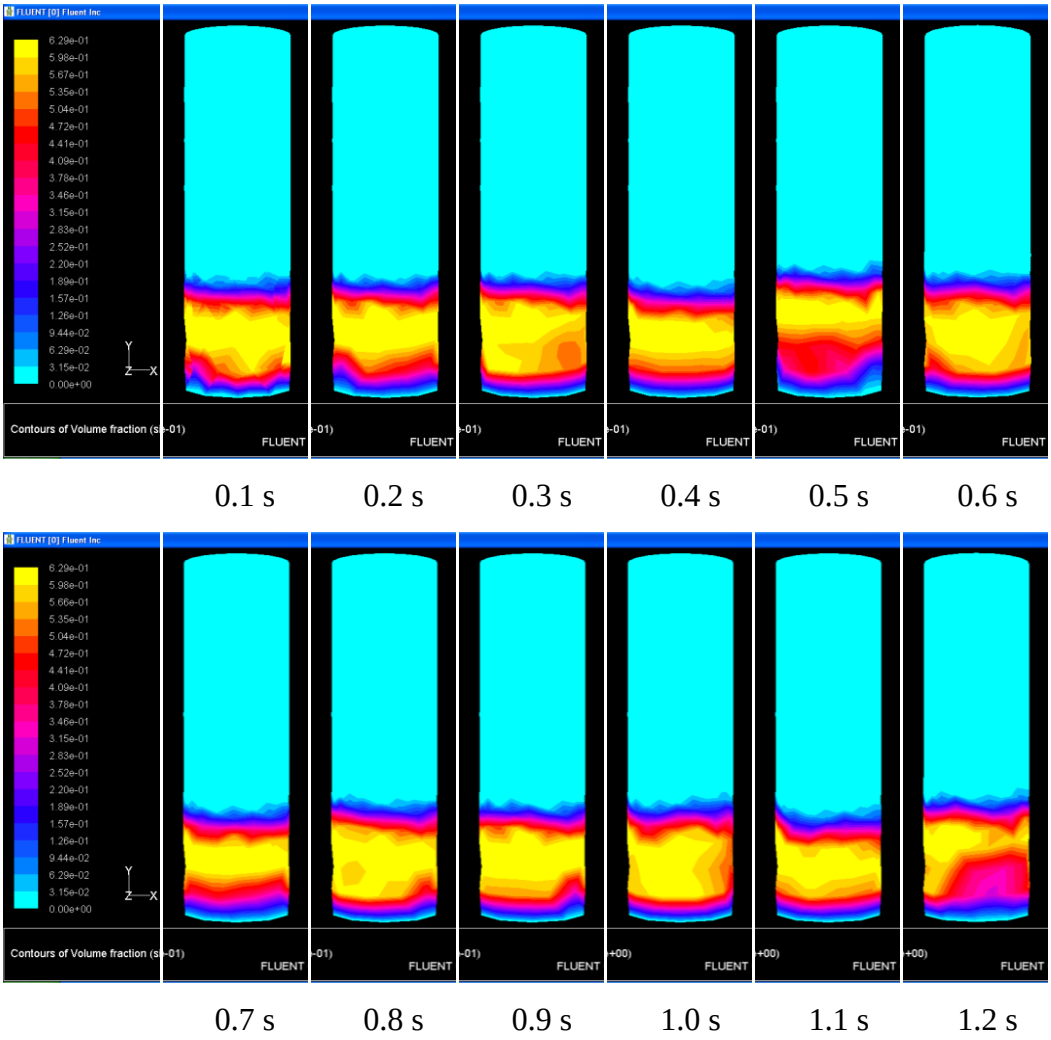

Figure B-21 Contours of silica sand volume fraction at time = 0.1 to 1.2 s.

The Run No. 7 case shows the best results from all these eight cases of the simplified model simulation under cold flow conditions. Therefore, the reactor model, the input parameters, and the optional model selections for Run No. 7 were used in this research.

APPENDIX C
HOT FLOW (REACTION CONSIDERED) CONDITIONS

For simulation time saving, the simplified air distributor model was used in this part. This simplified air distributor model was the one that had been run in the elevated temperature condition part, but its mesh was refined from 66,963 to 359,000 elements. The model in the Solution Setup step was set to be an Eulerian three phases model. Primary phase is gas-mixture, while the others phase consists of the phase of silica sand and the phase of biomass. The biomass which was studied in this part is a high-moisture rubber woodchip (27% M.C.). It was set in FLUENT step to have three materials component, i.e. wood-volatiles, carbon-solid, and water-liquid. The properties which had been set into the program are as follows:

- Density = 800 kg/ m^3
- Moisture content = 27%
- Volatile component fraction = 88.9%
- Combustible fraction = 10%
- Average diameter size = 15 mm

To simulate the BFBG model under hot flow conditions, a feeding pipe was necessary as the temperature inside the model may have affected the biomass moving down through the feeding pipe. Which the biomass feeding surface was set to located at about 500 mm high from the bottom of BFBG model. Its feeding rate was 37 kg/h (0.0102778 kg/s) which was calculated to be 0.003 m/s of velocity. This velocity was set as x-velocity = 0 m/s, y- velocity = -0.0015 m/s, and z-velocity = 0.002598 m/s follow to the velocity direction of 60 degree downward.

For the phase of gas-mixture, the components that existed in all the chemical reactions, i.e. tar, water-vapor, oxygen, nitrogen, hydrogen, methane, carbon monoxide, and carbon dioxide, were set. The chemical reactions and chemical rates, which depend on the type of biomass feedstock, were studied and introduced into the model simulation under hot flow condition by turning on the model of "Species" in Solution Setup step, as shown in Figure C-1. For Phase setting in Solution Setup step, the considered homogeneous were set

in gas-mixture phase while the considered heterogeneous reactions were set in Phase Interaction as seen in Figures C-2 and C-3, respectively.

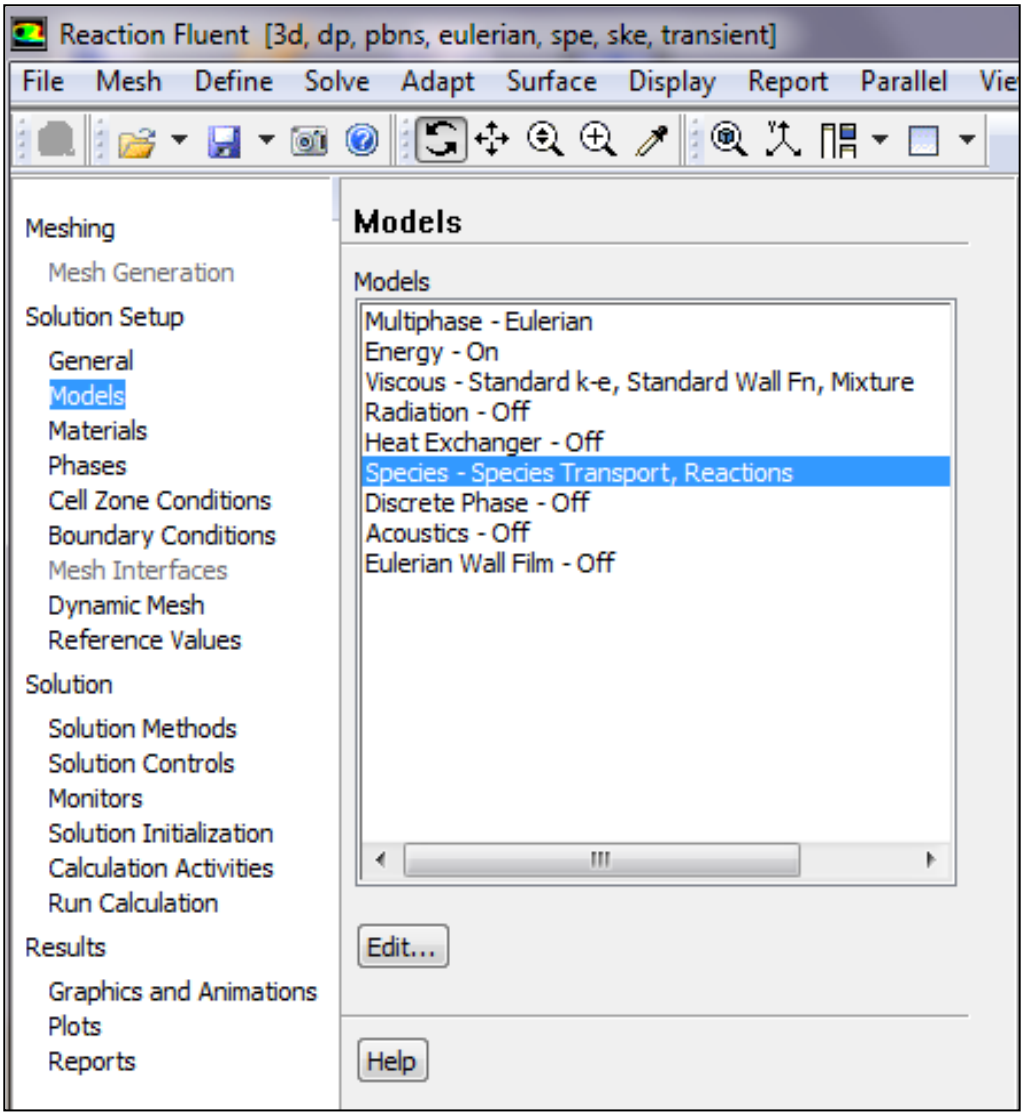

Figure C-1 FLUENT's window showing the Model settings in the Solution Setup step.

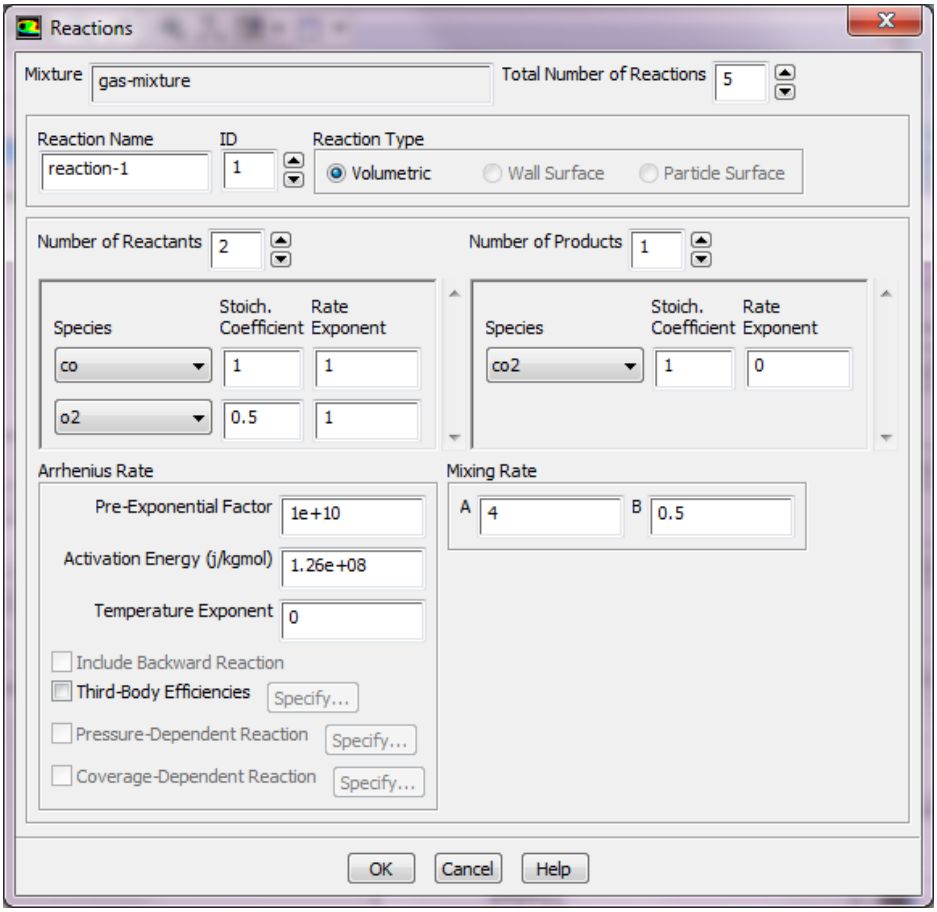

Figure C-2 FLUENT's window showing the Reaction settings in the Solution Setup step.

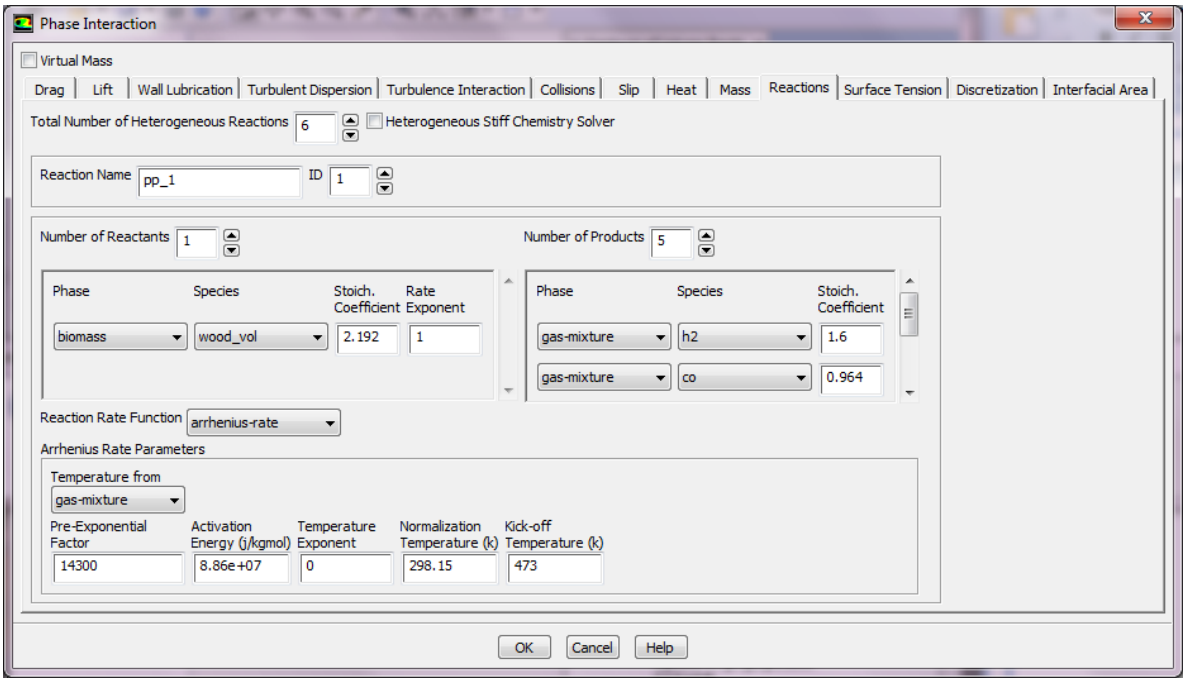

Figure C-3 FLUENT's window showing the Phase Interaction settings in the Solution Setup step.

The reactions that had been set in this research study are given as follows and their specifications are shown in Table C-1.

- Pyrolysis reaction (Devolatilisation)

Biomass + Heat --> Char + Light Gases + Vapor or Liquid (Tar) (R1)

↓

(such as H_2, CO, CO_2, CH_4, H_2O)

- Char combustion / Oxidation reaction

Partial combustion: $C + 0.5O_2 \rightarrow CO + Heat$ (R2)

Complete combustion: $C + O_2 \rightarrow CO_2 + Heat$ (R3)

- Char gasification

Boudouard reaction: $C + CO_2 \rightarrow 2CO - Heat$ (R4)

Steam gasification/ Water gas reaction: $C + H_2O \rightarrow H_2 + CO - Heat$ (R5)

Hydrogen gasification/ Methanation reaction: $C + 2H_2 \rightarrow CH_4 + Heat$ (R6)

- Homogeneous volatile oxidation

Carbon monoxide oxidation: $CO + 0.5O_2 \rightarrow CO_2 + Heat$ (R7)

Hydrogen oxidation: $H_2 + 0.5O_2 \rightarrow H_2O + Heat$ (R8)

Methane oxidation: $CH_4 + 2O_2 \rightarrow CO_2 + 2H_2O + Heat$ (R9)

Water gas shift reaction: $H_2O + CO \Leftrightarrow CO_2 + H_2 + Heat$ (R10)

At first, the simplified air distributor model was simulated under hot flow conditions on a stand-alone computer with 8 core processors, but it took such a long time, so a computer cluster was used instead, as shown in Table C-2. The computer cluster could be supported by CAD-IT Company for a little while. That is why the model simulation under hot flow condition cannot be completed.

Table C-1 Reactions specifications for the model simulation under hot flow conditions.

ID	1	2	3	4	5	6	7	8	9	10
Reaction Type	Volumetric	Particle Surface	Particle Surface	Particle Surface	Particle Surface	Particle Surface	Volumetric	Volumetric	Volumetric	Volumetric
Number of Reactants	2	2	2	2	2	2	2	2	2	2
Species	Wood-vol, O_2	C<s>, O_2	C<s>, O_2	C<s>, CO_2	C<s>, H_2O	C<s>, H_2	CO, O_2	H_2, O_2	CH_4, O_2	H_2O, CO
Stoich. Coefficient	Default Default	C<s>=1, O_2=0.5	C<s>=1, O_2=1	C<s>=1, CO_2=1	C<s>=1, H_2O=1	C<s>=1, H_2=2	CO=1, O_2=0.5	H_2=1, O_2=0.5	CH_4=1, O_2=2	H_2O=1, CO=1
Rate Exponent	Default	Default	Default	Default	Default	Default	Default	Default	Default	Default
Arrhenius Rate; - Pre-Exponential Factor - Activation Energy - Temperature Exponent	 Default Default Default	 Default Default Default	 Default Default Default	 1.11e+01 2.95e+07 Default	 1.53e-09 -2.09e+08 Default	 2.85e-10 -9.2e+07 Default	 1e+10 1.26e+08 Default	 5.16e+13 2.85e+07 Default	 3.552e+14 1.3e+08 Default	 2.78e+03 1.26e+07 Default
Number of Products	2	1	1	1	2	1	1	1	2	2
Species	CO_2, H_2O	CO	CO_2	CO	H_2, CO	CH_4	CO_2	H_2O	CO_2, H_2O	CO_2, H_2
Stoich. Coefficient	Default, Default	CO=1	CO_2=1	CO=2	H_2=1, CO=1	CH_4=1	CO_2=1	H_2O=1	CO_2=1, H_2O=2	CO_2=1, H_2=1
Rate Exponent	Default	Default	Default	Default	Default	Default	Default	Default	Default	Default
Mixing Rate - A = - B =	 Default Default	 -	 -	 -	 -	 -	 Default Default	 Default Default	 Default Default	 Default Default
Particle Surface Reaction - Diffusion Rate Constant - Effectiveness Factor	-	Default Default	Default Default	Default Default	Default Default	Default Default	-	-	-	-

Table C-2 The usage time for simulation under hot flow conditions.

Number of core processors	Time step size (s)	For 1 second need real time (day)
8	1×10^{-5}	300
24	1×10^{-5}	70
128	1×10^{-5}	30

The thermodynamic and hydrodynamic behaviors of the BFBG were deduced from the simulation results, as seen in Figures C-4 to C-30.

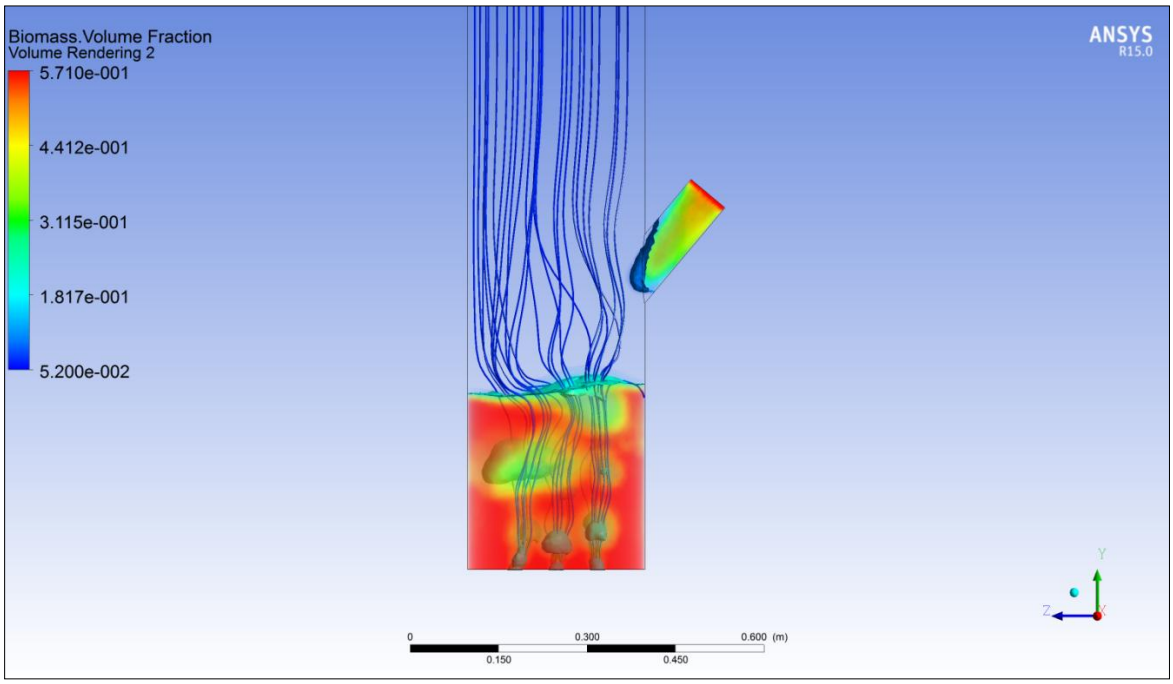

Figure C-4 Volume rendering of biomass volume fraction on a symmetrical 3-D section.

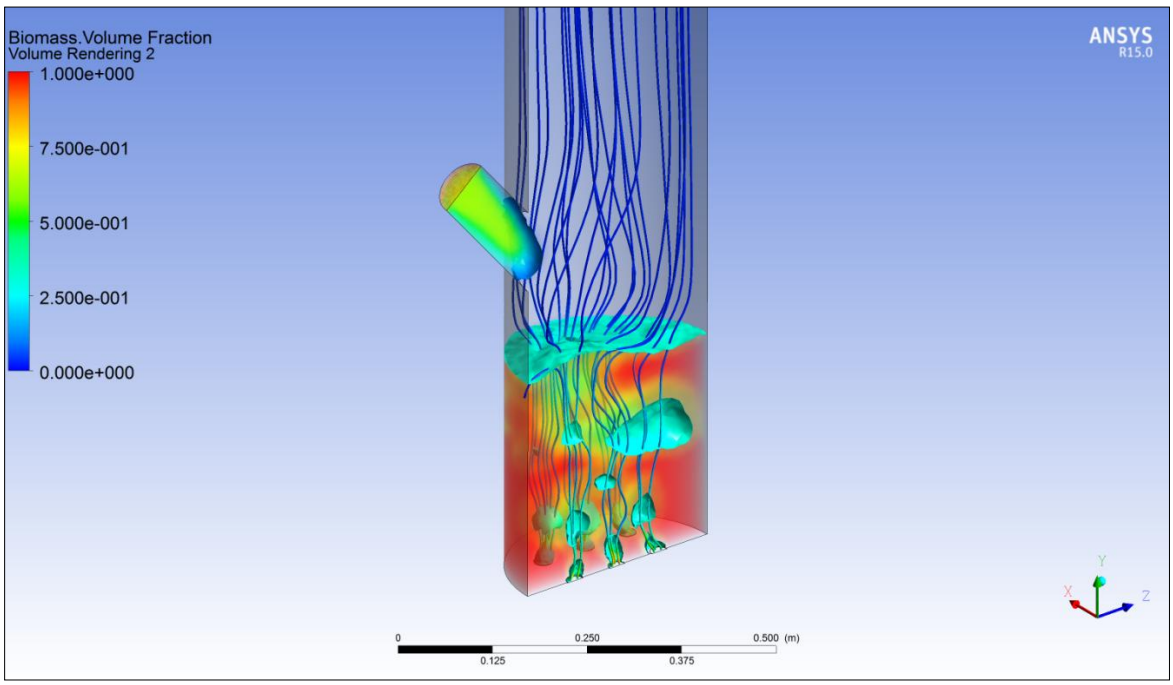

Figure C-5 Volume rendering of biomass volume fraction presented in 3-D.

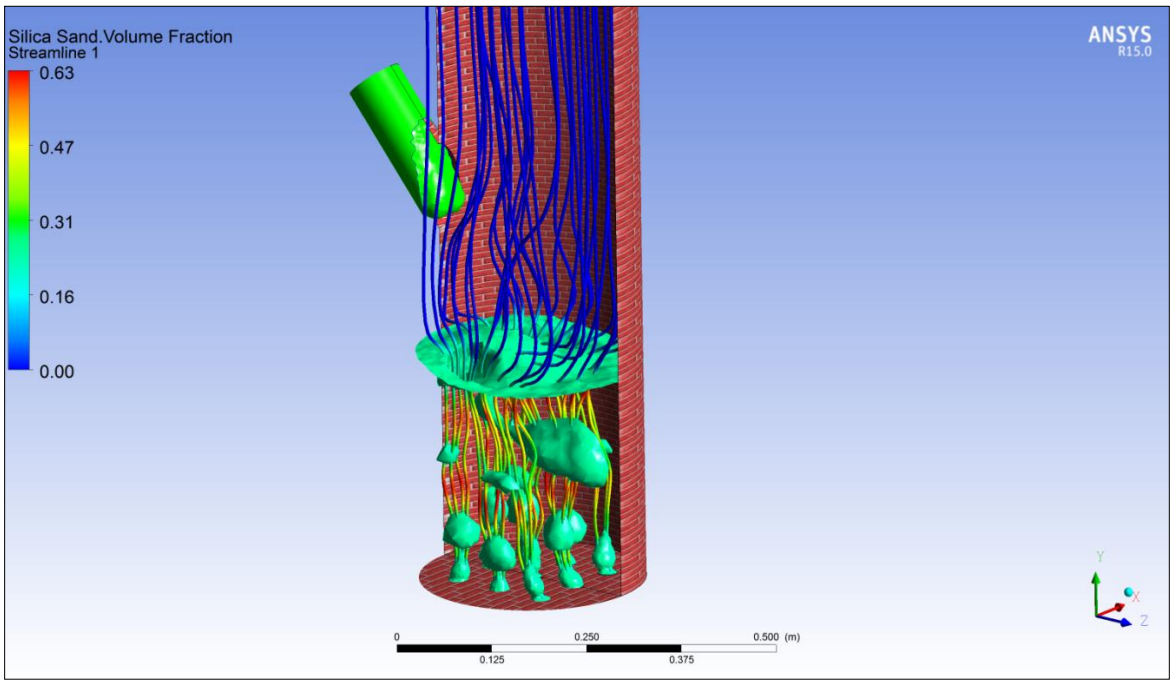

Figure C-6 Streamline of silica sand volume fraction presented in 3-D.

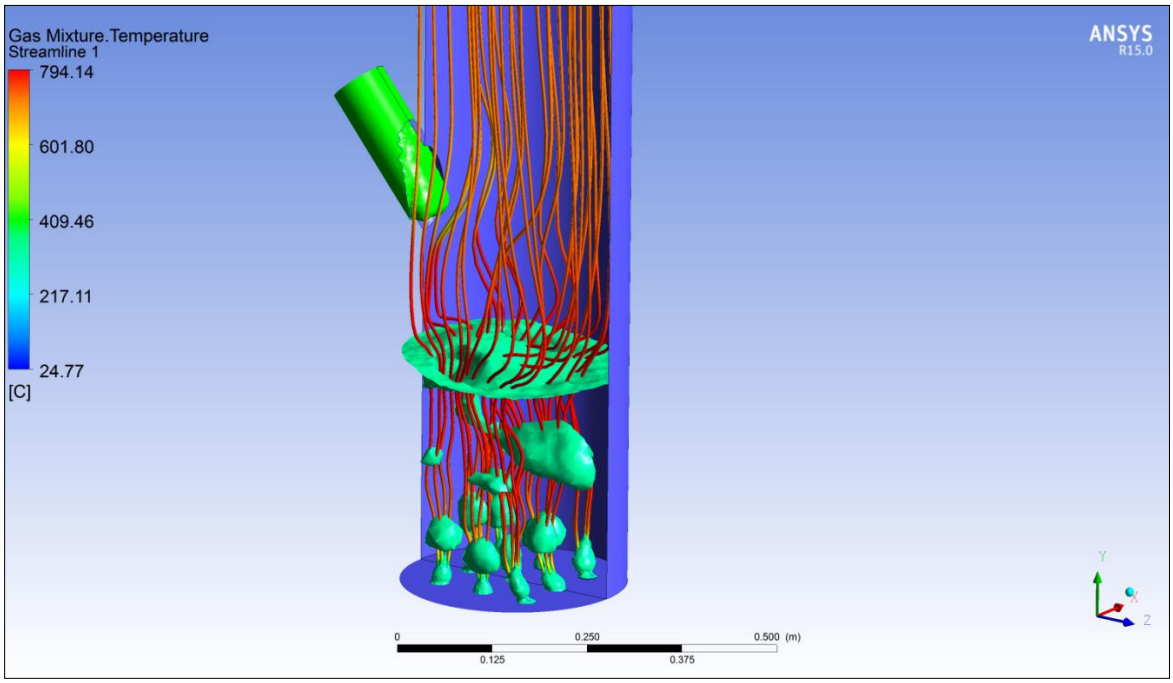

Figure C-7 Streamline of gas mixture temperature presented in 3-D.

The biomass started to flow into the reactor model through the feeding pipe, as seen in Figures C-4 and C-5, while the formation and motion of the bubbles inside bed zone were indicated with the volume fraction, as presented in Figures C-4 to C-6. The small bubbles were occurred and formed near the bottom of the bed, then collided with each

other to form the larger one at higher level inside bed zone when they were ascending toward the bed surface and bursted out finally.

After the air (gasifying agent) was introduced into the reactor model and passed through the hot sand bed (i.e. 800°C), the air temperature was increased by heat transfer from hot sand, as seen from the streamline of gas mixture temperature in Figure C-7. The air temperature was increased from room temperature to a bit lower than 800°C inside bed zone, but after it flew up through the bed surface the air temperature was gradually decreased. As checking by the contour of gas mixture temperature at each level along the height of the reactor model (as presented in Figures C-8 to C-13) and the contour of silica sand temperature at each level along the height of bed zone (as presented in Figures C-14 to C-19), the simulation results also show the same behaviors. The highest gas mixture temperature and the highest of silica sand temperature was a bit lower than 800°C inside bed zone with lower temperature than that was found inside the bubbles. The lowest gas mixture temperature (about 700°C) was happened in and around feeding pipe area due to the influence of moisture content of the introduced biomass. The gas mixture temperature was decreased from a bit lower than about 800°C to be a bit higher than 700°C after the gas mixture flew up through the bed surface, then constant at about 720°C until it reached to the outlet. For the heat from exothermic or endothermic reactions, it is still difficult to conclude that which reaction is dominating each zone at this beginning stage (0.35 s) by looking at these contours of temperature.

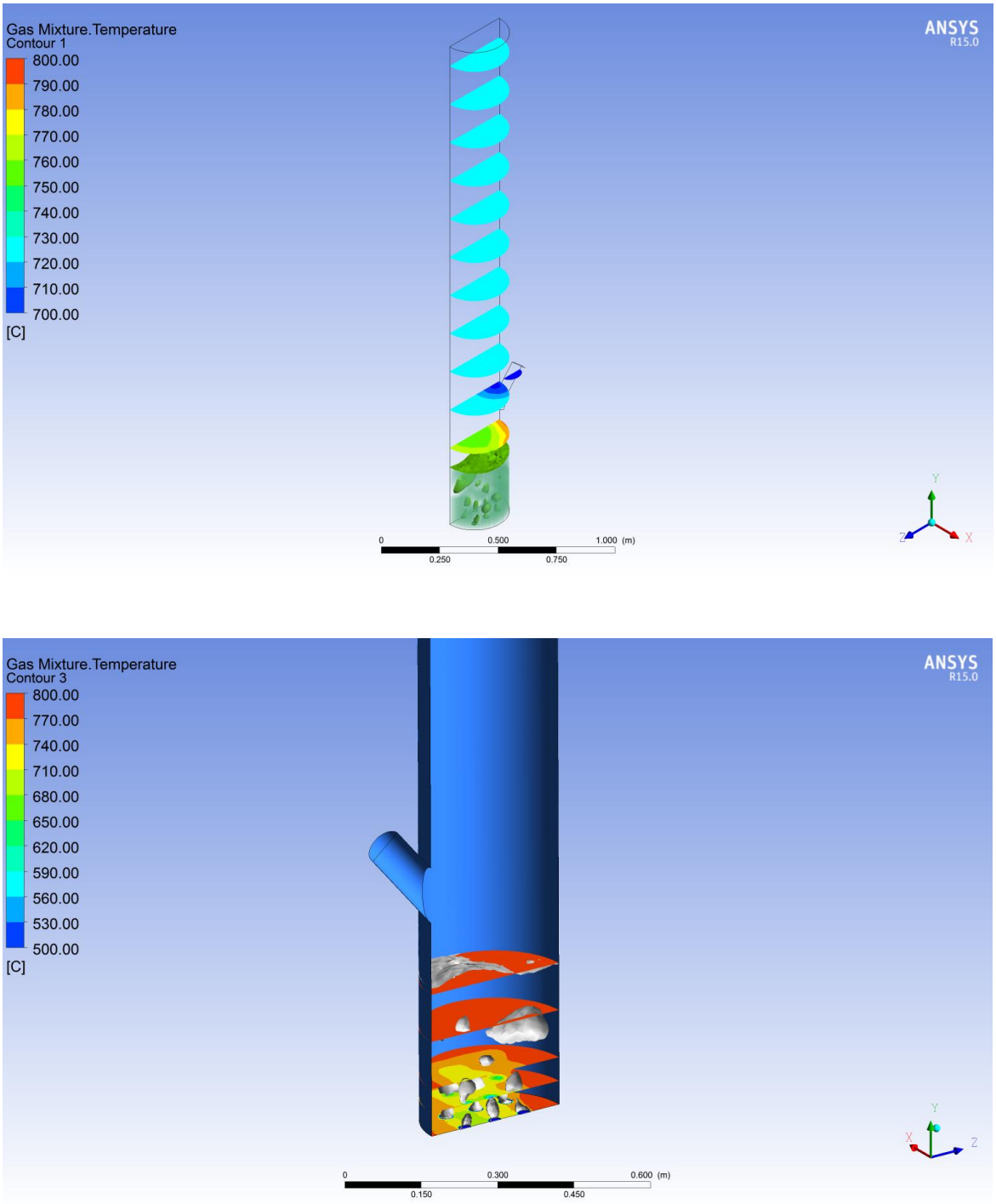

Figure C-8 Contour of gas mixture temperature at time = 0.35 s presented in 3-D.

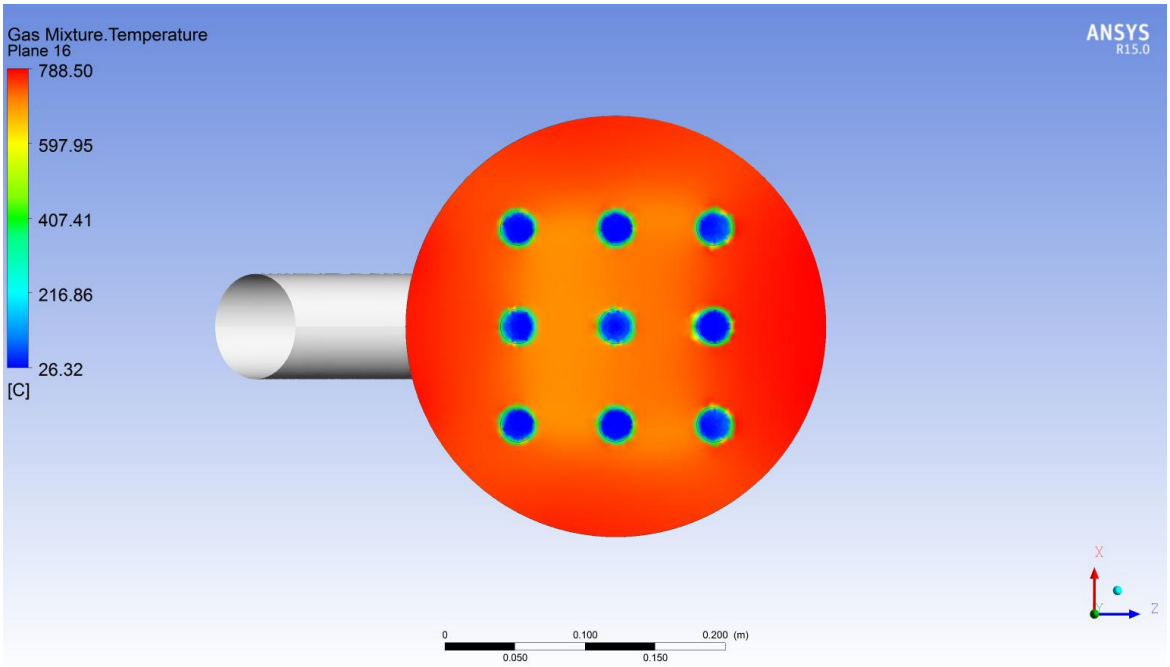

Figure C-9 Contour of gas mixture temperature at time = 0.35 s on plane at level 0 meters of height.

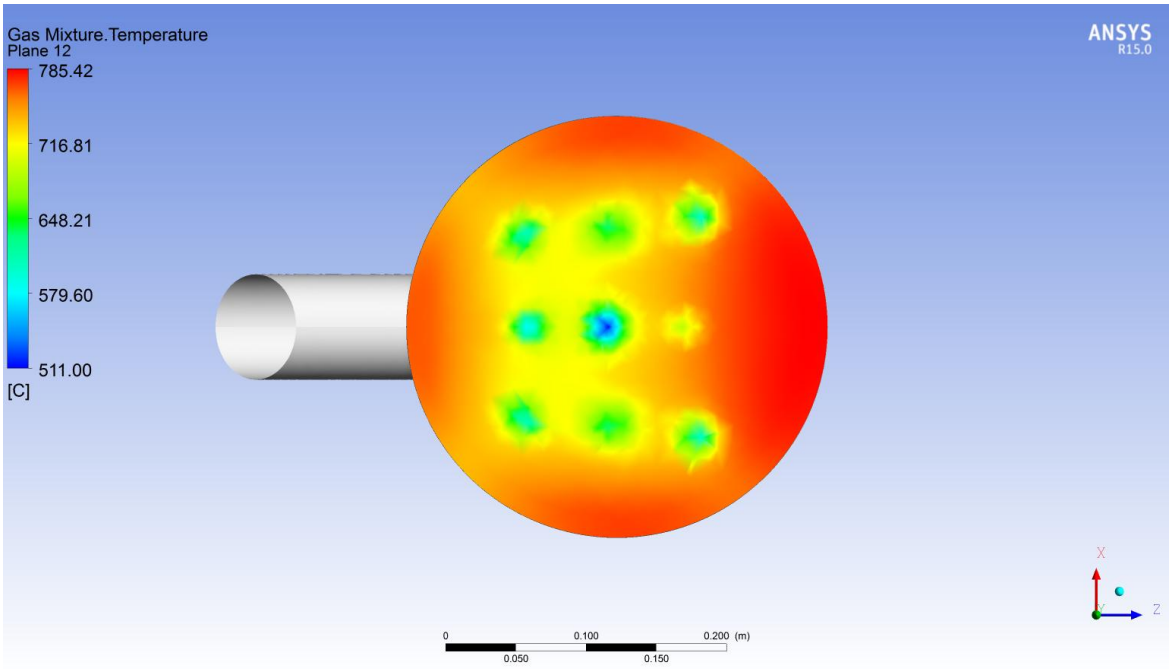

Figure C-10 Contour of gas mixture temperature at time = 0.35 s on plane at level 0.05 meters of height.

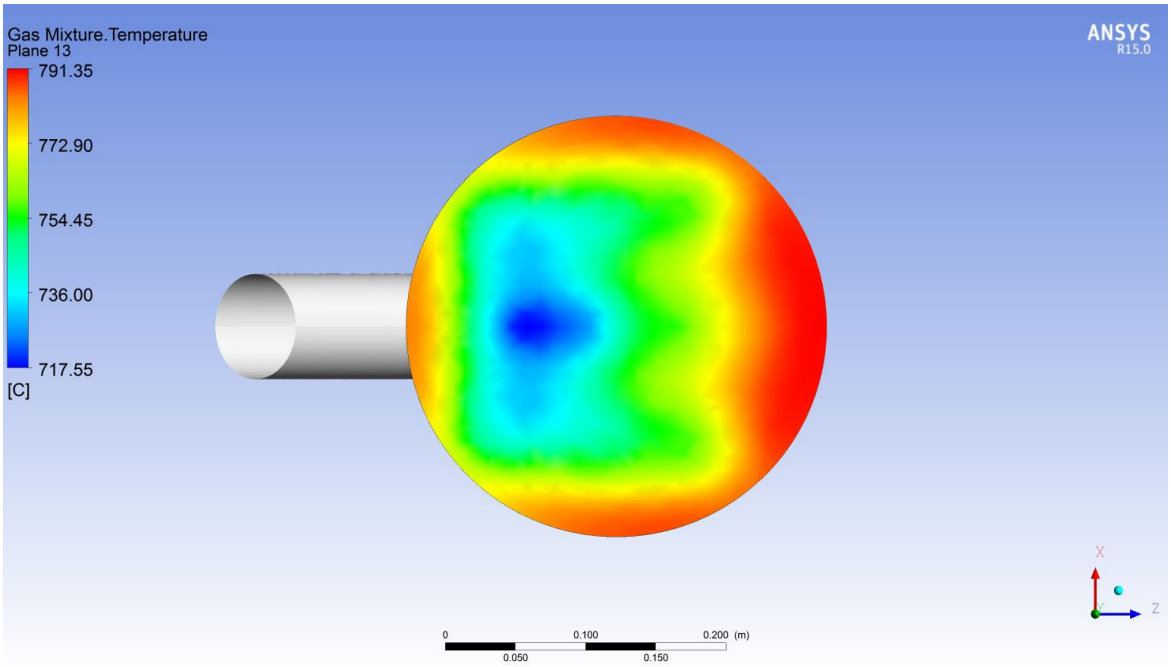

Figure C-11 Contour of gas mixture temperature at time = 0.35 s on plane at level 0.1 meters of height.

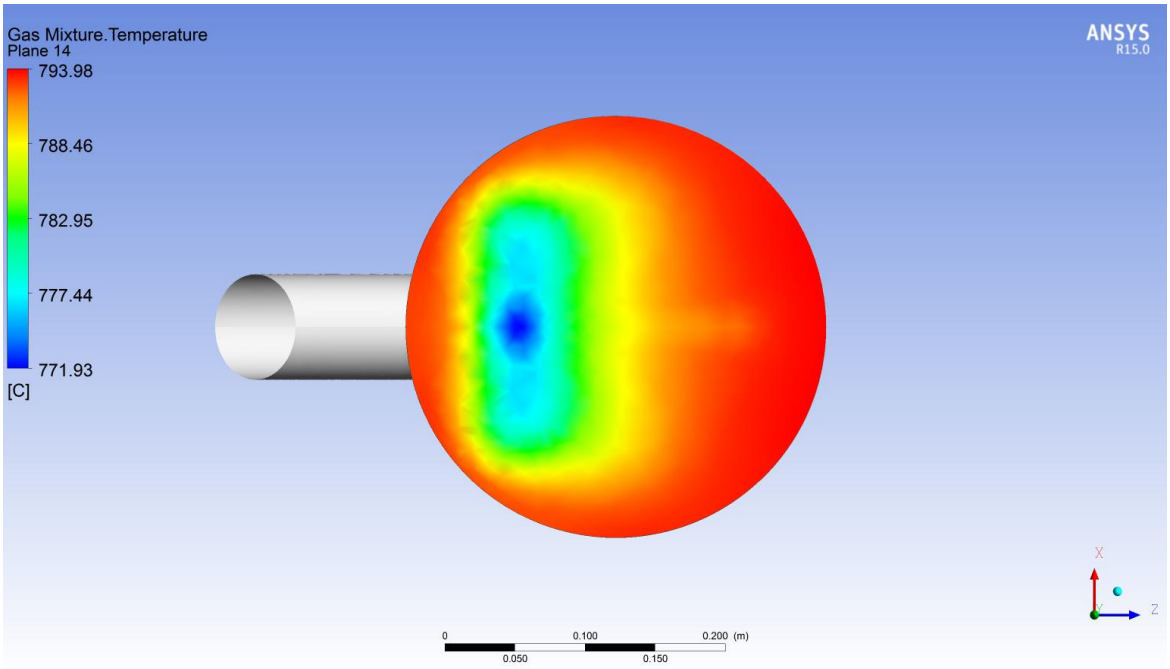

Figure C-12 Contour of gas mixture temperature at time = 0.35 s on plane at level 0.2 meters of height.

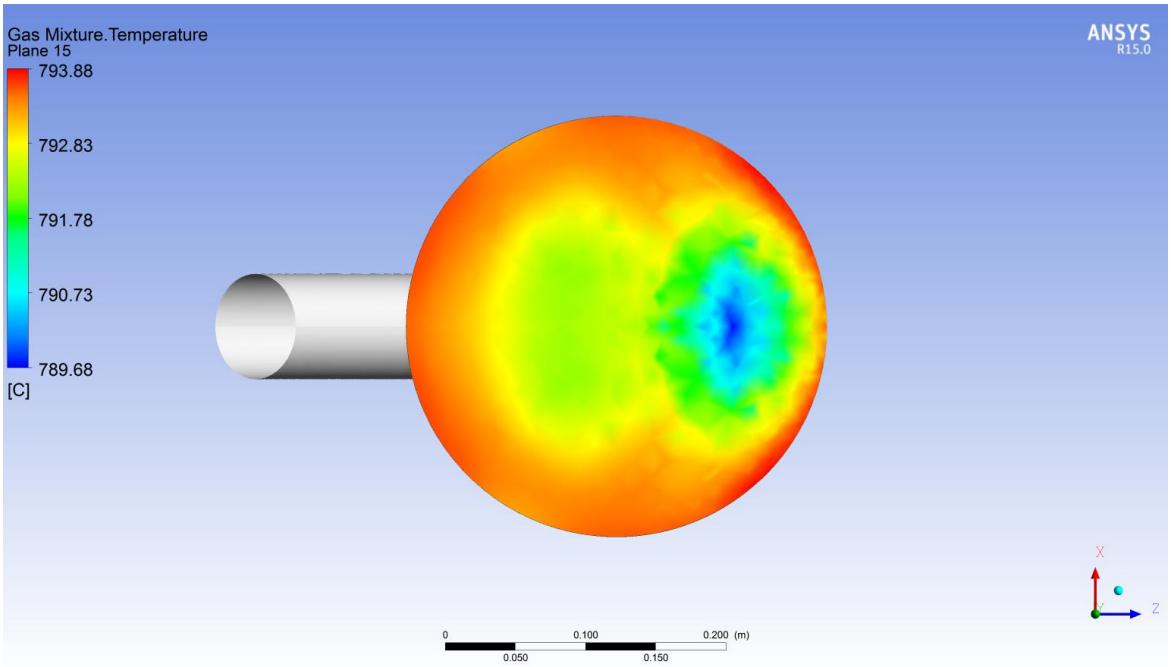

Figure C-13 Contour of gas mixture temperature at time = 0.35 s on plane at level 0.3 meters of height.

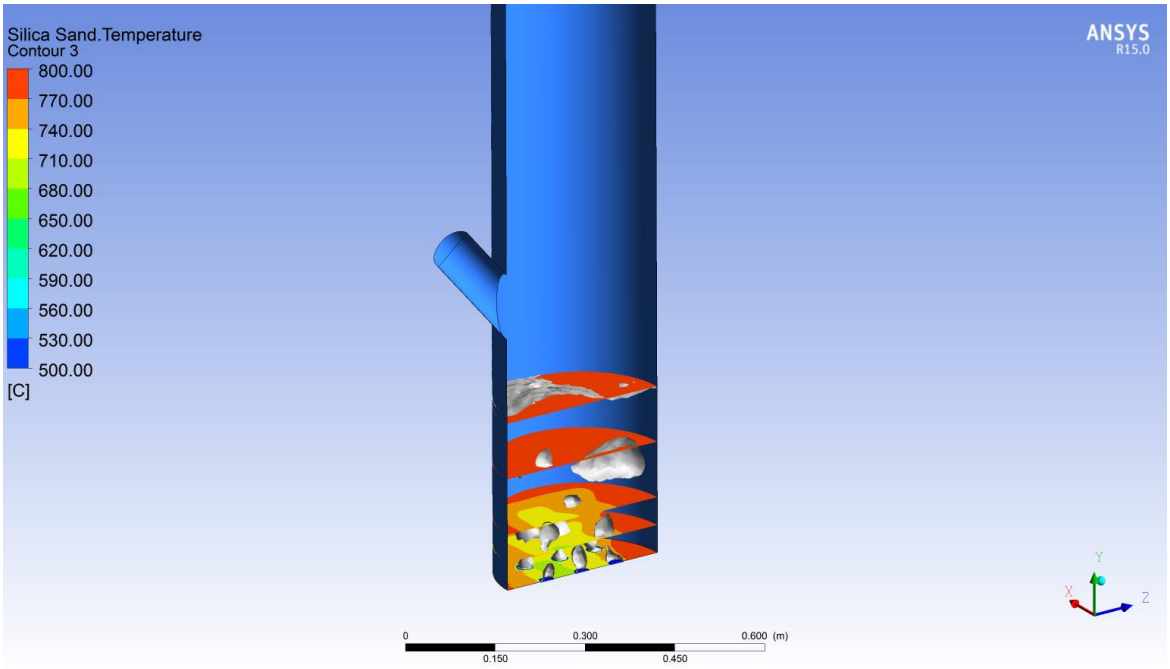

Figure C-14 Contours of silica sand temperature at time = 0.35 s presented 3-D.

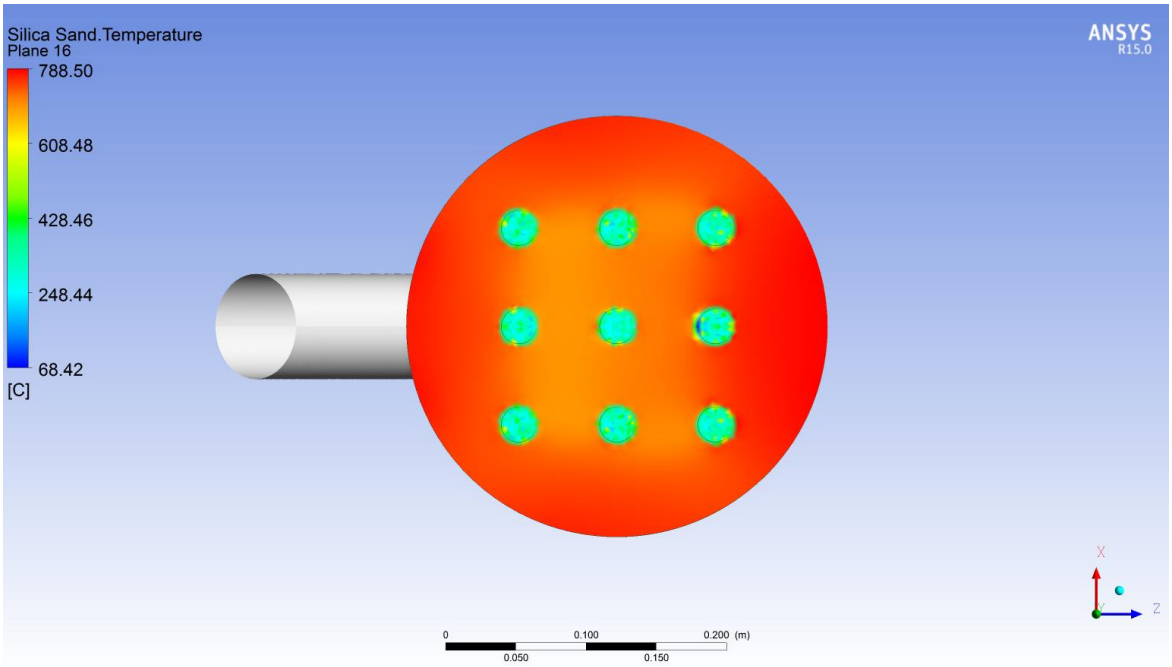

Figure C-15 Contour of silica sand temperature at time = 0.35 s on plane at level 0 meters of height.

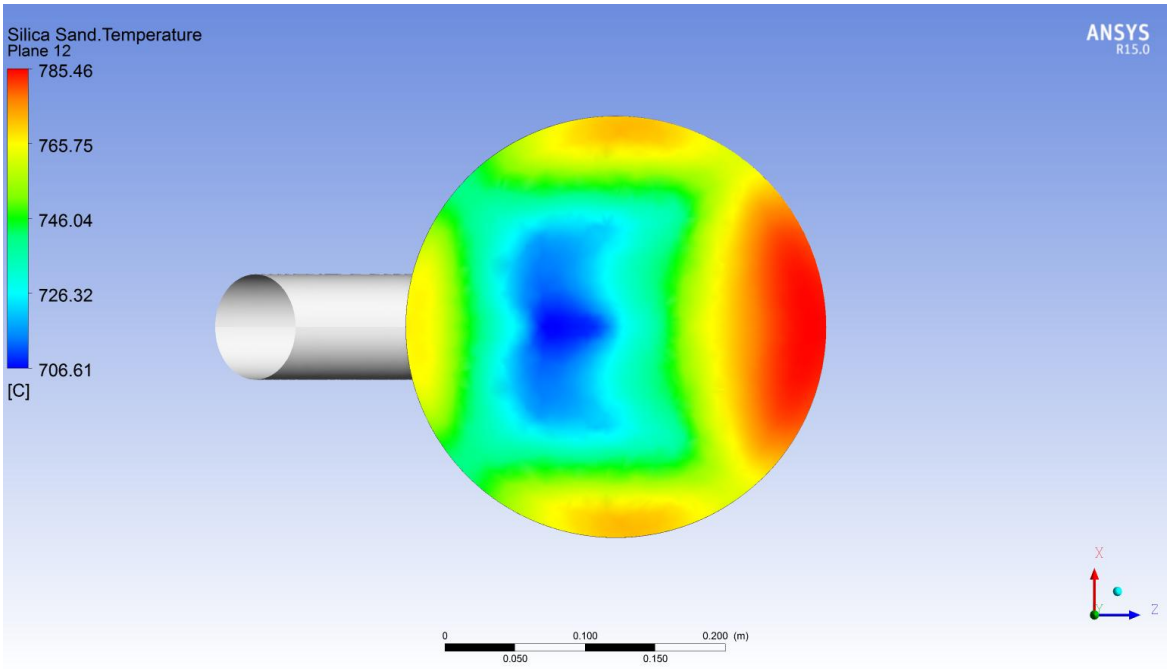

Figure C-16 Contour of silica sand temperature at time = 0.35 s on plane at level 0.05 meters of height.

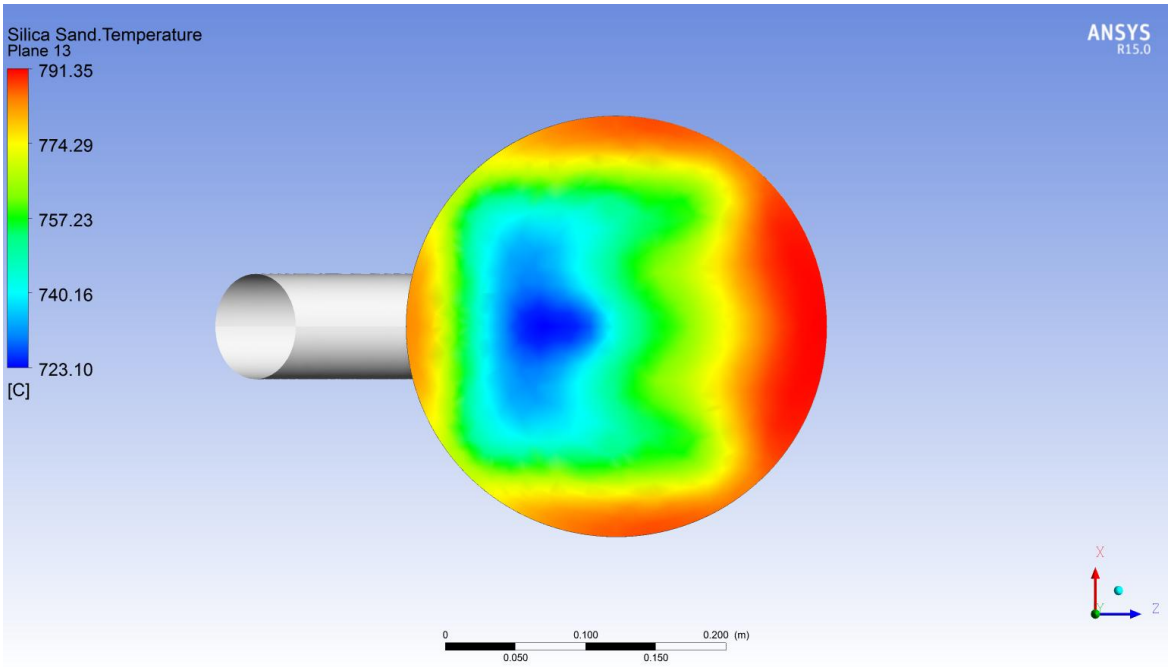

Figure C-17 Contour of silica sand temperature at time = 0.35 s on plane at level 0.1 meters of height.

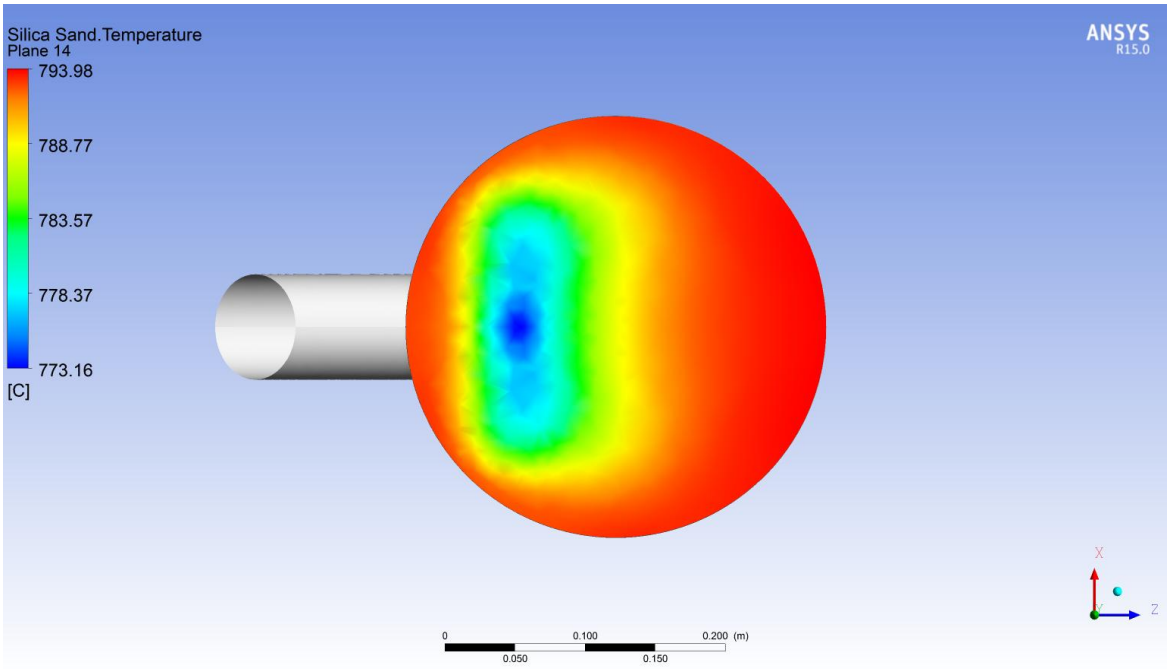

Figure C-18 Contour of silica sand temperature at time = 0.35 s on plane at level 0.2 meters of height.

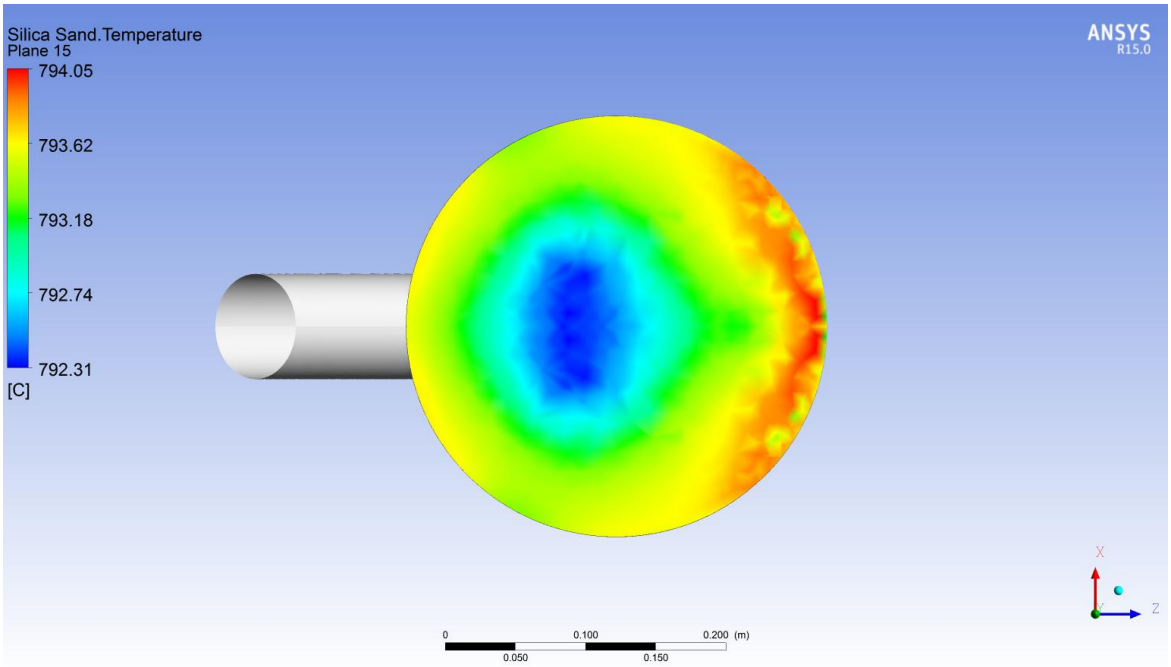

Figure C-19 Contour of silica sand temperature at time = 0.35 s on plane at level 0.3 meters of height.

This hot flow condition was simulated until it had only reached 0.35 seconds, which at this time the biomass was just still around the inlet surface. Therefore, the results of gases production were just at the beginning stage. Anyway, the simulation also showed a good tendency when compare to the model setting up as seen in Figures C-20 to C-30. The contour of mass fraction of biomass in terms of carbon-solid, wood-volatiles, and water-liquid were presented in Figures C-20 to C-22, respectively. At this time (0.35 s), there were found that the maximum amount of carbon-solid, wood-volatiles, and water-liquid were about 0.08, 0.66, and 0.27, respectively, which these results are reasonable with the biomass properties that had been set into the program at the beginning to have 10% of combustible fraction, 88.9% of volatile component fraction, and 27% of moisture content.

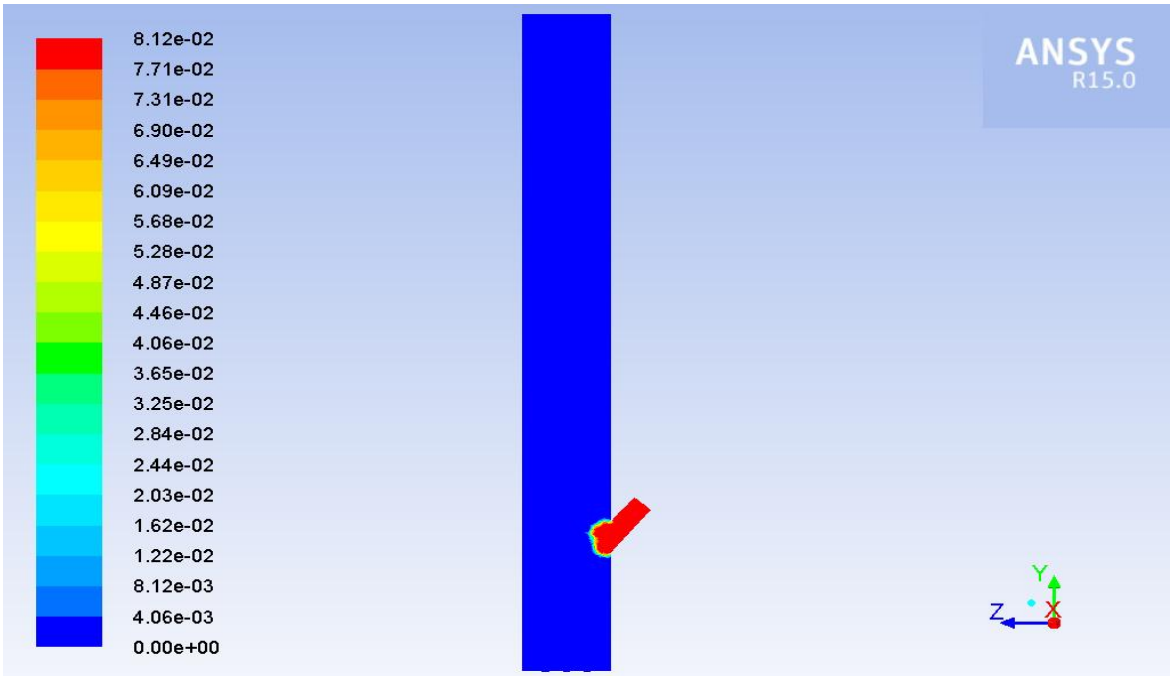

Figure C-20 Contour of mass fraction of carbon$_{<s>}$ (biomass) at time = 0.35 s on a symmetrical 3-D section.

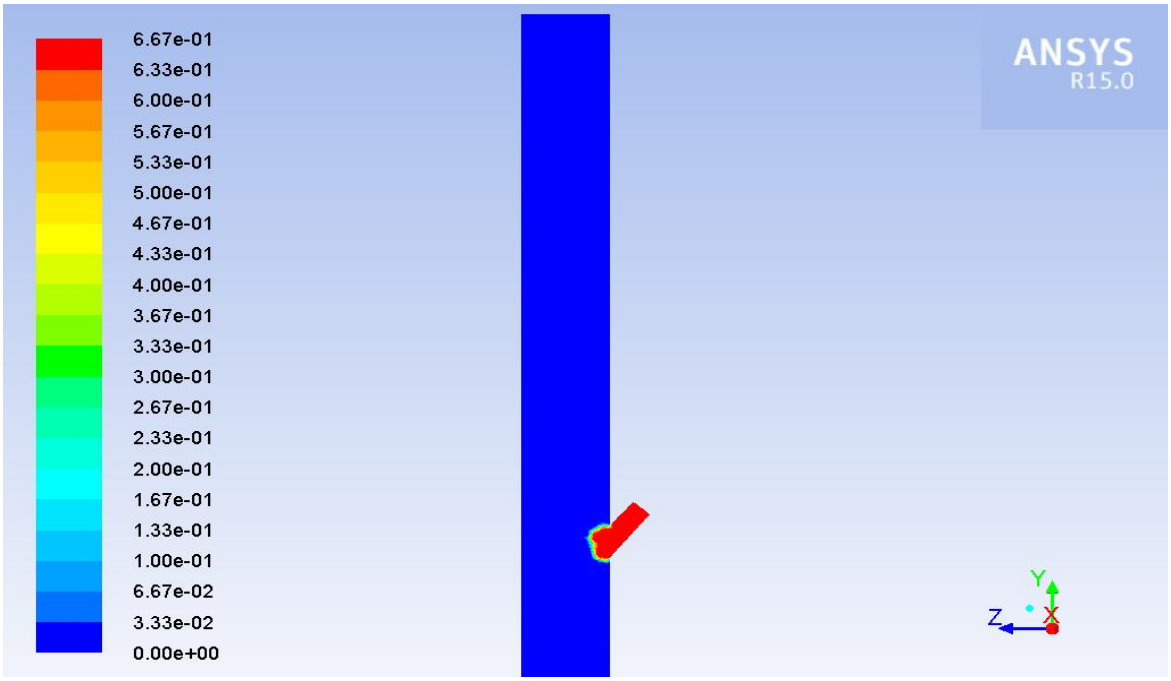

Figure C-21 Contour of mass fraction of wood_volatile (biomass) at time = 0.35 s on a symmetrical 3-D section.

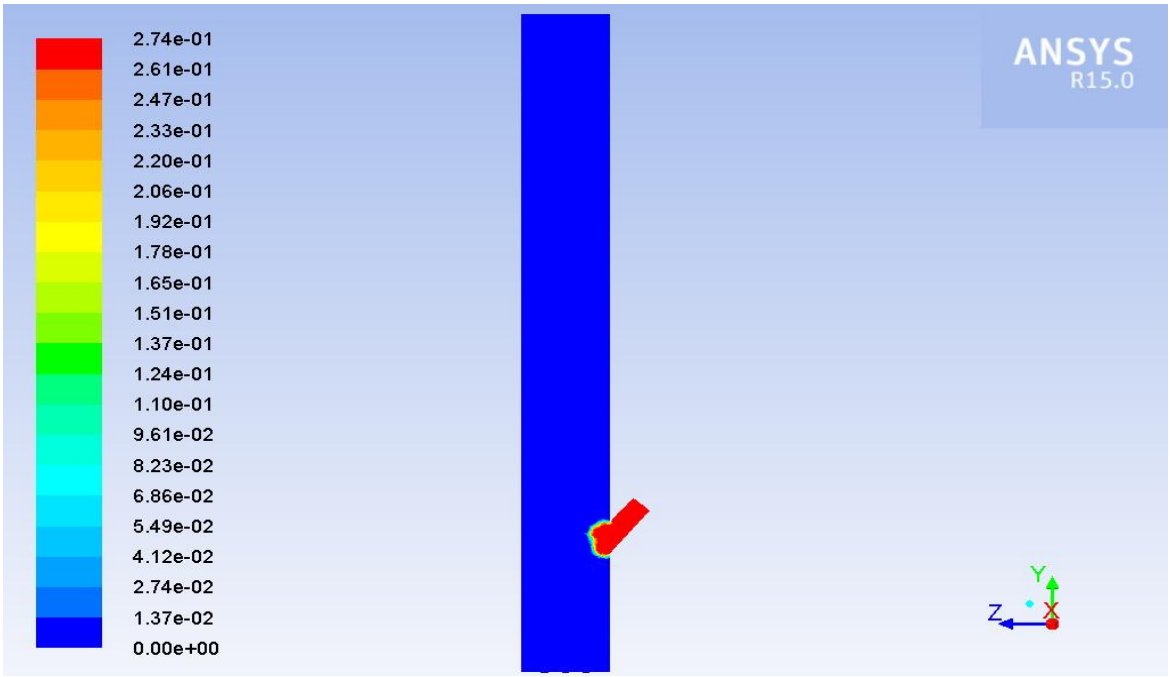

Figure C-22 Contour of mass fraction of $H_2O_{<l>}$ (biomass) at time = 0.35 s on a symmetrical 3-D section.

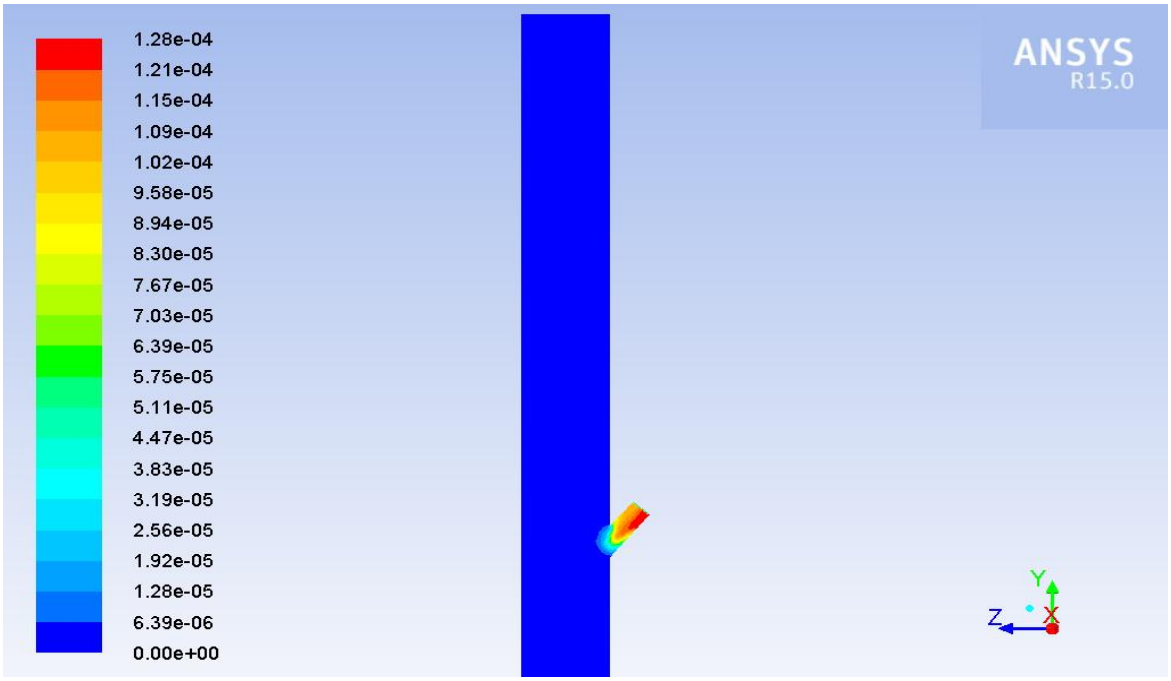

Figure C-23 Contour of mass fraction of CH_4 (gas-mixture) at time = 0.35 s on a symmetrical 3-D section.

The reactions that had been set as presented earlier in this Appendix C (R1 to R10) started to show results, as seen in Figures C-23 to C-30. The maximum contour of mass

fraction of CH_4 was just about 1.28 x 10^{-4} around the surface part of feeding pipe zone, then lower and lower until no fraction of CH_4 was found in reactor zone as seen in Figure C-23. This was probably due to the early stage when the hydrogen gasification/methanation reaction (R6) had just started to happen with carbon-solid and hydrogen from the introduced biomass.

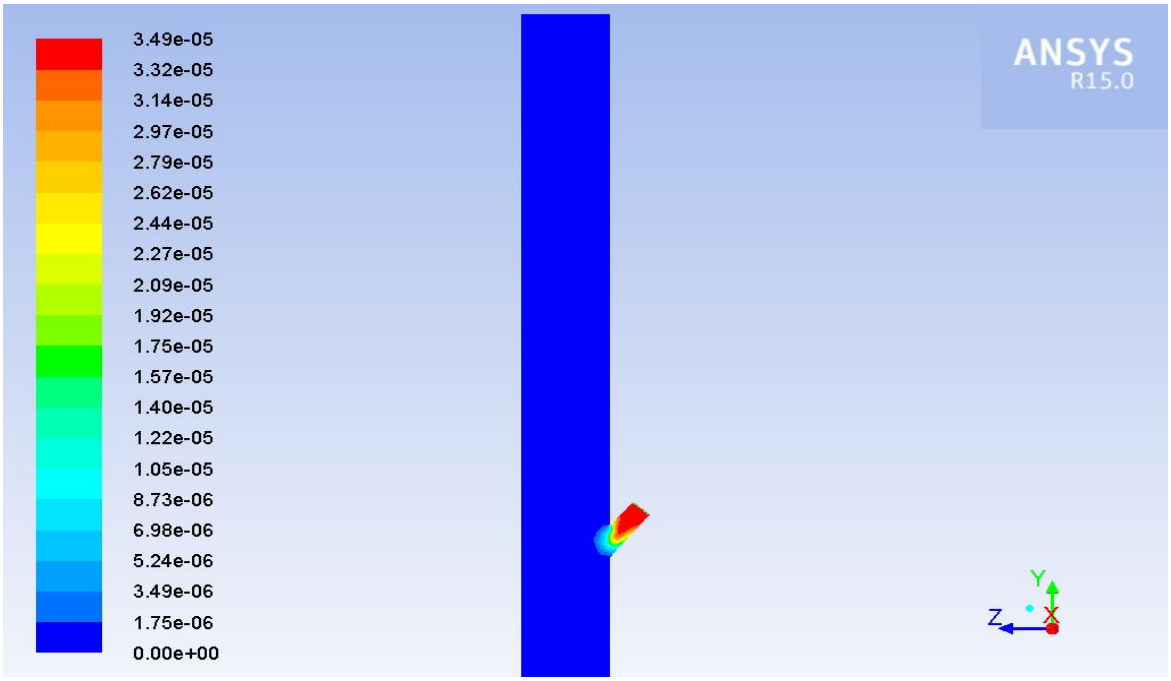

Figure C-24 Contour of mass fraction of CO (gas-mixture) at time = 0.35 s on a symmetrical 3-D section.

The CO production was found inside feeding the pipe zone with the maximum contour of mass fraction of CO of 3.49 x 10^{-5}, then moved lower and lower down until no fraction of CO could be found in reactor zone, as seen in Figure C-24. This is probably resulted from the carbon-solid from introduced biomass reacted with O_2 from air, CO_2 from oxidation reactions, and water-liquid from introduced biomass inside feeding pipe zone as called the partial combustion (R2), the Boudouard Reaction (R4), and the water gas reaction (R5), respectively.

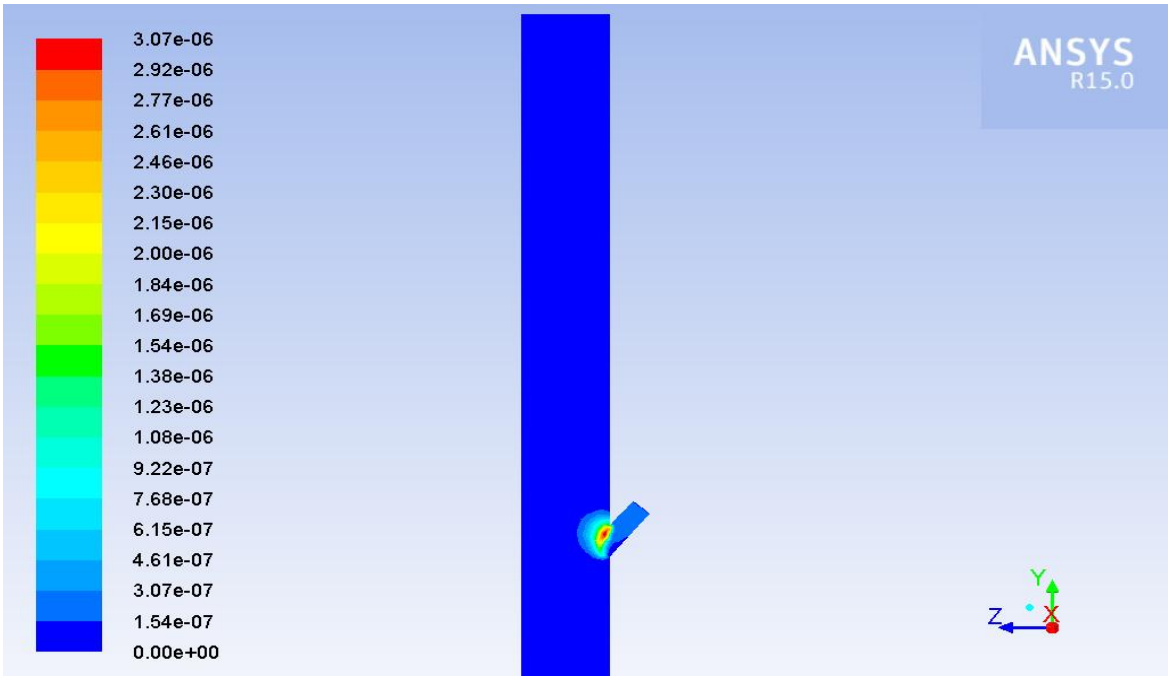

Figure C-25 Contour of mass fraction of CO_2 (gas-mixture) at time = 0.35 s on a symmetrical 3-D section.

The maximum contour of the mass fraction of CO_2 was just only about 3.07 x 10^{-6} around the junction part of the feeding pipe and the reactor zone, but no fraction of CO_2 was found outside of that zone, as seen in Figure C-25. This was probably due to the carbon-solid from the introduced biomass reacting with O_2 from air as called the complete combustion (R3), the CO which was occurred inside feeding pipe zone reacted with O_2 from air as named the carbon monoxide oxidation (R7), the CH_4 which was occurred inside feeding pipe zone reacted with O_2 from air as named the methane oxidation (R9), and the water-liquid from introduced biomass reacted with CO which was occurred inside feeding pipe zone as called the water gas shift reaction (R10) just starts to dominate the CO_2 production.

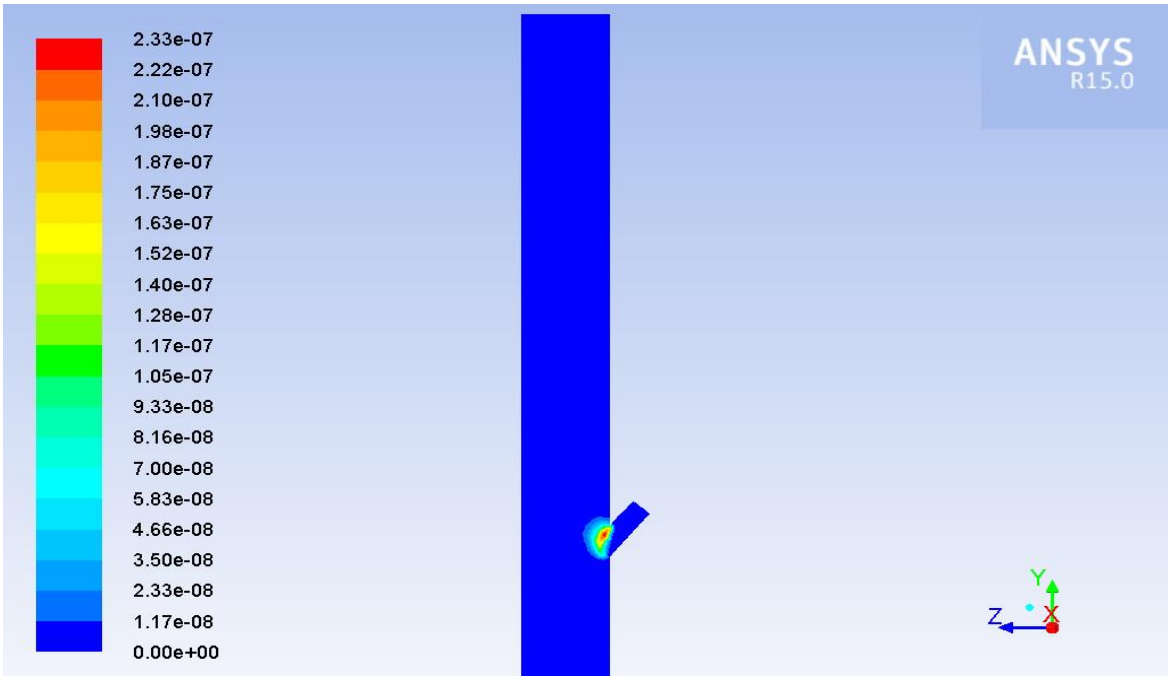

Figure C-26 Contour of mass fraction of H_2 (gas-mixture) at time = 0.35 s on a symmetrical 3-D section.

The H_2 production was around the junction part of feeding pipe and reactor zone with the maximum contour of mass fraction of H_2 of 2.33 x 10^{-7}, as seen in Figure C-26. This was probably due to at that part the water-liquid from introduced biomass reacted with carbon-solid from introduced biomass as called the water gas reaction (R5) and the water-liquid from introduced biomass reacted with CO which was occurred inside feeding pipe zone as called the water gas shift reaction (R10) just starts to dominate the H_2 production.

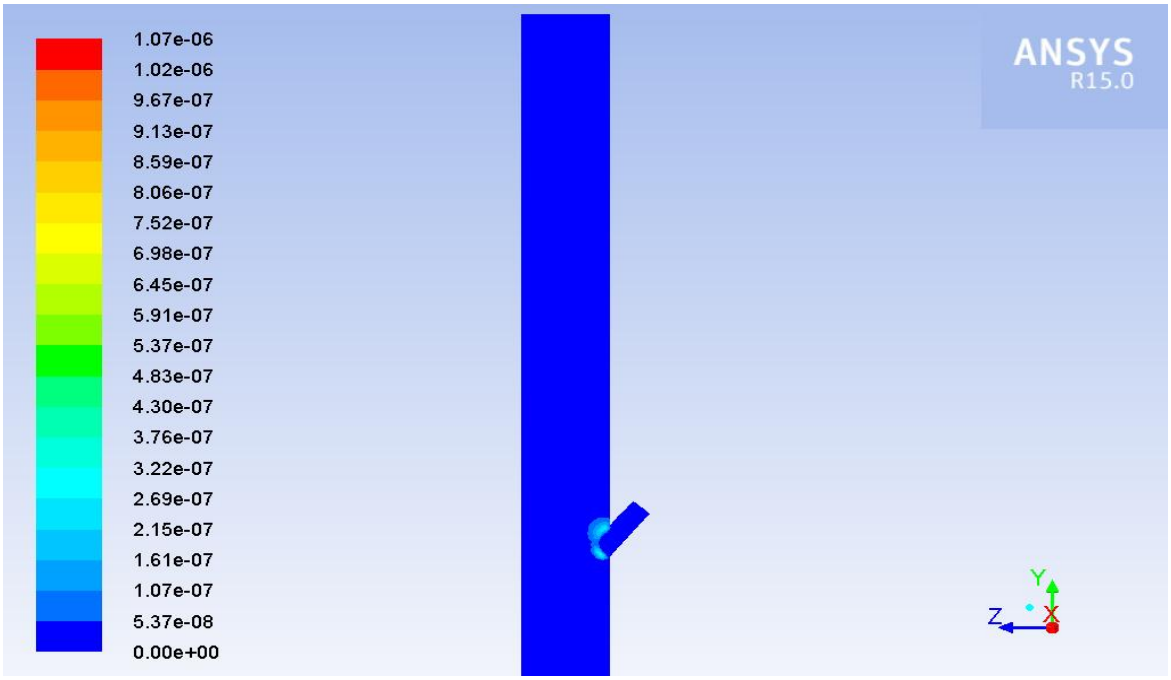

Figure C-27 Contour of mass fraction of H_2O (gas-mixture) at time = 0.35 s on a symmetrical 3-D section.

At time of 0.35 seconds, the H_2O production was found just a little bit around the junction part of the feeding pipe and reactor zone with the maximum contour of mass fraction of H_2O of 3 x 10^{-7}, as seen in Figure C-27. This was probably due to at that part the H_2, which was occurred from the water gas reaction and water gas shift reaction, reacted with O_2 from air as called the hydrogen oxidation (R8) just starts to dominate the H_2O production.

The maximum contour of the mass fractions of N_2 and O_2 were about 0.7 and 0.2, as seen in Figures C-28 and C-29, respectively. These results are really reasonable with the amounts of N_2 and O_2 in the air, i.e. N_2 78% and O_2 21%.

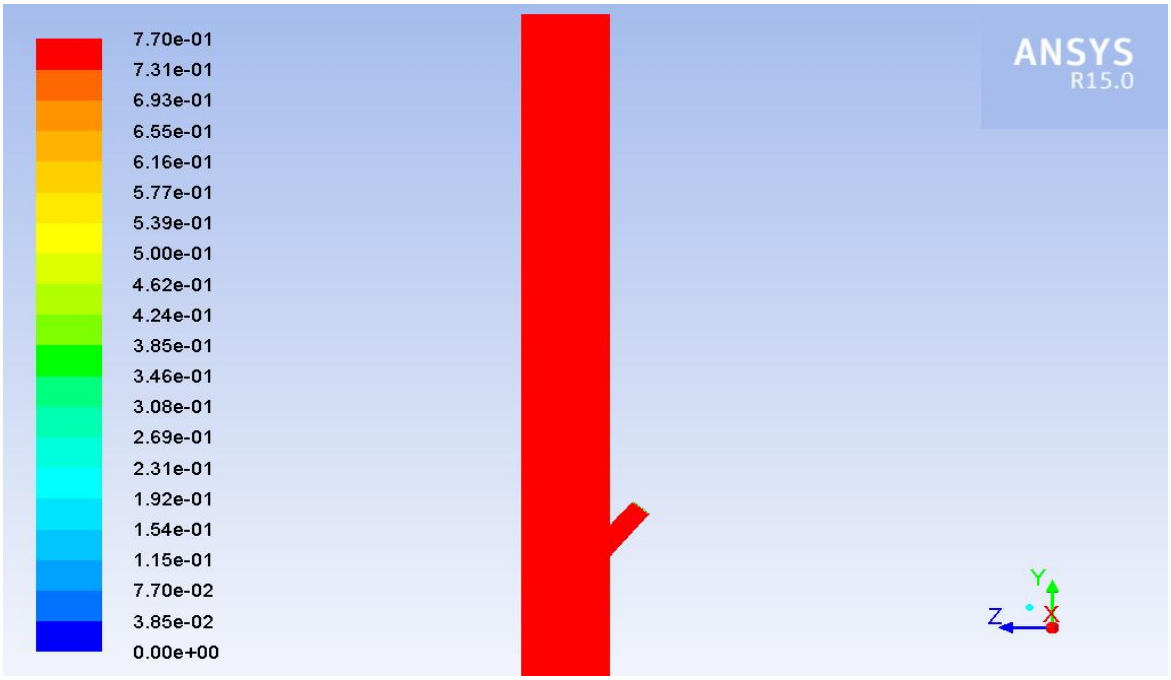

Figure C-28 Contour of mass fraction of N_2 (gas-mixture) at time = 0.35 s on a symmetrical 3-D section.

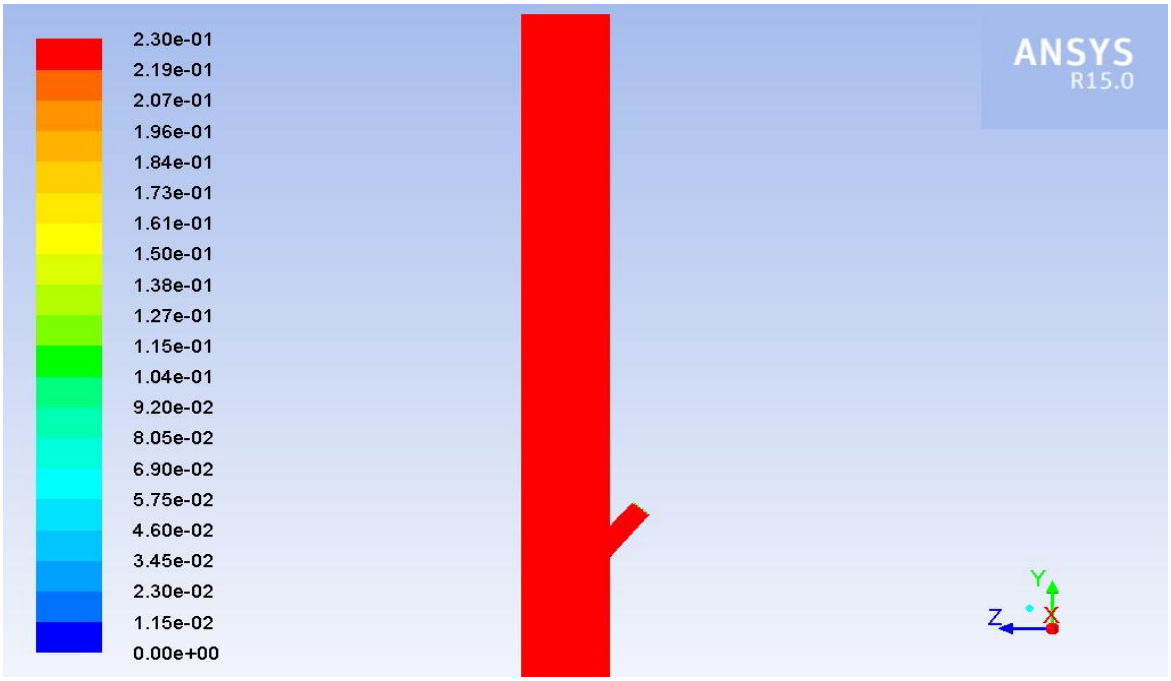

Figure C-29 Contour of mass fraction of O_2 (gas-mixture) at time = 0.35 s on a symmetrical 3-D section.

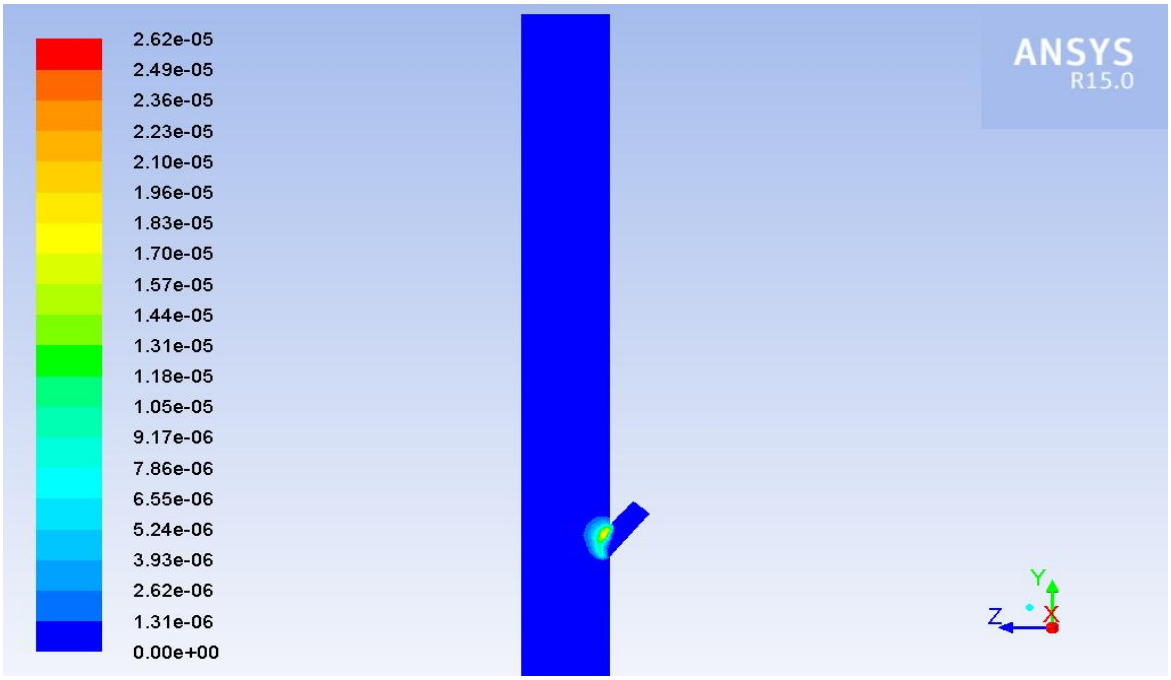

Figure C-30 Contour of mass fraction of tar (gas-mixture) at time = 0.35 s on a symmetrical 3-D section.

At the time of 0.35 seconds, the tar production was found with a small amount around the junction part of the feeding pipe and reactor zone with the maximum contour of the mass fraction of tar being 3 x 10^{-7}, as seen in Figure C-30. This was probably due to the tar production has been dominated by the pyrolysis reaction around that part.

These simulation results under hot flow conditions may imply that the input parameters that had been set into the model were correct as the simulation results showed a good tendency, but time was still needed for running the simulation until the gas-mixture at the outlet part happened and was able to validate with the experimental results.